

AFRL-PR-WP-TR-2005-2164

**SiC THIN FILMS ON INSULATING
SUBSTRATES FOR ROBUST
MICROELECTROMECHANICAL
SYSTEM (MEMS) APPLICATIONS**



**Lin Cheng, Ph.D.
Andrew J. Steckl, Ph.D.**

**University of Cincinnati
Department of Electrical and Computer Engineering
Cincinnati, OH 45221-0627**

NOVEMBER 2003

Final Report for 14 September 1998 – 13 August 2003

Approved for public release; distribution is unlimited

STINFO FINAL REPORT

**PROPELLSION DIRECTORATE
AIR FORCE RESEARCH LABORATORY
AIR FORCE MATERIEL COMMAND
WRIGHT-PATTERSON AIR FORCE BASE, OH 45433-7251**

NOTICE

Using Government drawings, specifications, or other data included in this document for any purpose other than Government procurement does not in any way obligate the U.S. Government. The fact that the Government formulated or supplied the drawings, specifications, or other data does not license the holder or any other person or corporation; or convey any rights or permission to manufacture, use, or sell any patented invention that may relate to them.

This report was cleared for public release by the Air Force Research Laboratory Wright Site Public Affairs Office (AFRL/WS) and is releasable to the National Technical Information Service (NTIS). It will be available to the general public, including foreign nationals.

PAO Case Number: AFRL-WS-05-1965
Date Cleared: 23 August 2005

THIS TECHNICAL REPORT IS APPROVED FOR PUBLICATION.

/s/

JAMES D. SCOFIELD, Ph.D.
Program Manager
Electrical Technology and Plasma Physics Branch
Power Division

/s/

JOSEPH A. WEIMER
Chief
Electrical Technology and Plasma Physics Branch
Power Division

/s/

BRAD L. BEATTY, Major, USAF
Deputy for Science
Power Division

This report is published in the interest of scientific and technical information exchange and its publication does not constitute the Government's approval or disapproval of its ideas or findings.

REPORT DOCUMENTATION PAGE

*Form Approved
OMB No. 0704-0188*

Public reporting burden for this collection of information is estimated to average 1 hour per response, including the time for reviewing instructions, searching existing data sources, gathering and maintaining the data needed, and completing and reviewing this collection of information. Send comments regarding this burden estimate or any other aspect of this collection of information, including suggestions for reducing this burden to Department of Defense, Washington Headquarters Services, Directorate for Information Operations and Reports (0704-0188), 1215 Jefferson Davis Highway, Suite 1204, Arlington, VA 22202-4302. Respondents should be aware that notwithstanding any other provision of law, no person shall be subject to any penalty for failing to comply with a collection of information if it does not display a currently valid OMB control number. **PLEASE DO NOT RETURN YOUR FORM TO THE ABOVE ADDRESS.**

1. REPORT DATE (DD-MM-YYYY) November 2003		2. REPORT TYPE Final		3. DATES COVERED (From - To) 14 Sep 1998 – 13 Aug 2003	
4. TITLE AND SUBTITLE SiC Thin Films On Insulating Substrates For Robust Microelectromechanical System (MEMS) Applications		5a. CONTRACT NUMBER F33615-98-1-2865			
		5b. GRANT NUMBER			
		5c. PROGRAM ELEMENT NUMBER 62203F			
6. AUTHOR(S) Lin Cheng, Ph.D. Andrew J. Steckl, Ph.D.		5d. PROJECT NUMBER 3145			
		5e. TASK NUMBER 23			
		5f. WORK UNIT NUMBER LH			
7. PERFORMING ORGANIZATION NAME(S) AND ADDRESS(ES) University of Cincinnati Department of Electrical and Computer Engineering Cincinnati, OH 45221-0627		8. PERFORMING ORGANIZATION REPORT NUMBER			
		9. SPONSORING / MONITORING AGENCY NAME(S) AND ADDRESS(ES) PROPELLION DIRECTORATE AIR FORCE RESEARCH LABORATORY AIR FORCE MATERIEL COMMAND WRIGHT-PATTERSON AFB, OH 45433-7251			
		10. SPONSOR/MONITOR'S ACRONYM(S) AFRL/PRPE			
12. DISTRIBUTION / AVAILABILITY STATEMENT Approved for public release; distribution unlimited.		11. SPONSOR/MONITOR'S REPORT NUMBER(S) AFRL-PR-WP-TR-2005-2164			
		13. SUPPLEMENTARY NOTES This technical effort is a dissertation submitted to the Division of Research and Advanced Studies of the University of Cincinnati in partial fulfillment of the requirements for the degree of Doctorate of Philosophy (Ph.D.) in the Department of Electrical and Computer Engineering and Computer Science of the College of Engineering. This document has color content.			
		14. ABSTRACT <p>An increasing demand for robust MEMS devices, such as micro-sensors, that can operate at temperatures well above 300 °C and often in severe environments has stimulated the search for alternatives to Si. [1] The research in direct formation of SiC thin-films on insulating substrates (SiCOI) has found a very promising technology for producing SiC device structures and providing an excellent alternative material solution for high temperature applications. MEMS applications require that large area of uniform SiC films is formed on insulating substrates or sacrificial layers [2], [3] such as Si₃N₄, SiO₂, polycrystalline Si (poly-Si), glass, quartz and sapphire substrates. The growth of highly uniform SiC films with a highly stable and impermeable thin-film structure as well as a smooth interface of SiC-substrate is the essential step in producing a MEMS device with the required long-term stability. The major portion of this study was devoted to optimize the SiC growth conditions for different device applications.</p>			
15. SUBJECT TERMS: MEMS, silicon carbide, SiCOI, insulating substrate, temperature sensor					
16. SECURITY CLASSIFICATION OF:			17. LIMITATION OF ABSTRACT SAR	18. NUMBER OF PAGES 167	19a. NAME OF RESPONSIBLE PERSON James M. Scofield, Ph.D.
a. REPORT Unclassified	b. ABSTRACT Unclassified	c. THIS PAGE Unclassified			19b. TELEPHONE NUMBER (include area code) 937-255-5949

ABSTRACT

An increasing demand for robust MEMS devices, such as micro-sensors, that can operate at temperatures well above 300°C and often in severe environments has stimulated the search for alternatives to Si.^[1] The research in direct formation of SiC thin-films on insulating substrates (SiCOI) has found a very promising technology for producing SiC device structures and providing an excellent alternative material solution for high temperature applications. MEMS applications require that large area of uniform SiC films is formed on insulating substrates or sacrificial layers^{[2], [3]} such as Si₃N₄, SiO₂, polycrystalline Si (poly-Si), glass, quartz and sapphire substrates. The growth of highly uniform SiC films with a highly stable and impermeable thin-film structure as well as a smooth interface of SiC-substrate is the essential step in producing a MEMS device with the required long-term stability. The major portion of this study was devoted to optimize the SiC growth conditions for different device applications.

First, for electrically controlled MEMS devices, *in-situ* N₂-doped 3C-SiC thin-films have been grown by low-pressure chemical vapor deposition (LPCVD) on low-stress, amorphous Si₃N₄/p-Si(111) substrate using the single organosilane precursor trimethylsilane [(CH₃)₃SiH]. The effects of N₂ flow rate and growth temperature on the electrical properties of SiC films were investigated by Hall Effect measurements. The electron carrier concentration is between 10¹⁷~10¹⁸/cm³. The lowest resistivities at 400 K and 300 K are 1.12x10⁻² and 1.18x10⁻¹ Ω•cm, respectively. The corresponding sheet resistances are 75.02 and 790.36 Ω/□. The SiC film structure was studied by X-ray

diffraction (XRD). The 3C-SiC films oriented in the <111> direction with a 2θ peak at 35.5° and line widths between $0.18^\circ\sim0.25^\circ$ were obtained. The SiC-Si₃N₄ interface is very smooth and free of voids. To pattern the SiC films into the desired structural shapes, selective etching is required.^[4] The inductively coupled plasma (ICP) etching of 3C-SiC films was then examined in both NF₃/Ar and Cl₂/Ar mixtures. Two different mask materials (ITO and Shipley 1818 photo-resist) were compared. The effects of RF power, DC bias, ICP power and gas flow ratio on etch rates have been discussed.

Second, a novel fiber-optic temperature sensor, which is rugged, compact, stable, and can be easily fabricated, has been developed by using the SiC thin-film grown on sapphire substrate. The film thickness was optimized to $2\sim3\text{ }\mu\text{m}$, while the optimal 3MS flow rate ranged from 35~40 sccm to produce an optically flat SiC film. The sensors were operated at temperature from 22°C to 540°C . The shifts in resonance minima versus temperature from the reflection spectra fit a linear function, giving a relative temperature sensitivity of $1.9\times10^{-5}/^\circ\text{C}$. The capability of providing a $\pm3\text{ }^\circ\text{C}$ accuracy was discovered at 532°C in a wide-open ambient, through a 14-days operating life.

References:

-
- [¹] Mehran Mehregany, Christian A. Zorman, Thin solid Films pp. 355-356, 518-524, 1999.
 - [²] J. Chen, J. Scofield, A. J. Steckl, *J. Electrochem. Soc.*, 147, p. 3845, 2000.
 - [³] M. Mehregany, C. A. Zorman, N. Rajan, and C. H. Wu, *Materials Sci. Forum*, 338-342, 541, 2000.
 - [⁴] J. J. Wang, E. S. Lambers, S. J. Pearton, M. Ostling, C. -M. Zetterling, J. M. Grow and F. Ren, Solid-State Electronics Vol. 42 No. 5, pp. 743-747, 1998.

ACKNOWLEDGMENTS

I would like to dedicate this dissertation to my beloved parents, Zhiqiu Cheng and Fengzhi Zhao, for their forever support, patient, and understanding to help me go through these years of PhD study and research. This is also for my sweet daughter, who is always my driving force to accelerate. I would like to take this opportunity to express my sincere and deep thanks to my advisor, Dr. A. J. Steckl, for his technical guidance on this project and for consistently providing moral and financial support throughout my graduate education. Without his help, I would never be able to achieve my goals. I also wish to especially thank my sponsor and committee, Dr. J. D. Scofield, for his strongly technical support and always kind encouragement. I appreciate my dissertation committee, Dr. Nevin, Dr. Boyd, and Dr. Kosel for taking the time to take part in my committee and for their critical comments and useful suggestions which have greatly benefited me in my research. I am grateful to my friends and colleagues at UC NanoLab and Cincinnati Chinese Church for their invaluable help and support throughout my stay in Cincinnati. I would also like to express my gratitude to Ms. Julie Muncheon for her invaluable help on countless number of occasions. My heart-felt thanks also go to my dear friends including Feng Jiao, Kun Dong, Dong-Seon Lee, Jihong Chen, Irving Chyr, Zhou Yu, Robert Hudgins, Jason Heikenfeld, Robert Jones, Ming Pan, David Chao, Chanaka Munasinghe, Chris Baker, Boon Lee, Robert Chi, Michael Garter, and John Wang. The excitement of my research project combined with the help and support of all these people has made it a truly rewarding experience for me to work on my Ph.D. dissertation at the University of Cincinnati.

TABLE OF CONTENTS

Contents	Page No.
Abstract	i
Acknowledgments	v
Table of contents	vi
List of figures.....	xi
List of tables	xviii
CHAPTER 1. INTRODUCTION.....	1
1.1 Silicon carbide (SiC)	1
1.2 SiC on insulating substrates — SiCOI structures.....	4
1.3 Chemical vapor deposition (CVD)	7
1.4 Inductively coupled plasma (ICP) etching	11
1.5 SiC for MEMS and sensors operating in harsh environments	13
1.6 References	17
CHAPTER 2. OBJECTIVES	20
CHAPTER 3. LITERATURE REVIEW.....	25
3.1 Growth of SiC thin-film on insulators	26
3.1.1 Chemical vapor deposition (CVD)	27
3.1.2 SiC thin-film grown on insulators by CVD	29
3.2 Planarization of SiC thin-film.....	31
3.3 Plasma etching of SiC.....	31

3.3.1 Basic mechanism of plasma etching.....	32
3.3.2 Plasma etching parameters	35
3.3.3 Plasma reactors	38
3.3.4 Plasma etching of SiC	42
3.4 SiC for MEMS applications.....	44
3.5 Thin-film Fabry-Perot interferometer for fiber-optic temperature sensor....	48
3.5.1 Fabry-Perot interferometer for temperature sensor	48
3.5.2 Wavelength-encoded temperature measurement	49
3.6 References.....	51

CHAPTER 4. GROWTH AND DOPING OF SiC THIN-FILM ON LOW-

STRESS, AMORPHOUS Si₃N₄/Si SUBSTRATE.....	61
4.1 Low-stress, amorphous Si ₃ N ₄ grown on Si Substrate by LPCVD	61
4.2 Growth of SiC thin-film by CVD.....	62
4.2.1 Introduction of RM rapid thermal CVD system	62
4.2.2 Sample preparation	68
4.2.3 Ex-Situ cleaning	70
4.2.4 In-Situ cleaning	71
4.2.5 Growth with trimethylsilane	71
4.2.6 In-Situ nitrogen doping.....	73
4.3 Characterization of as-grown SiC thin-film.....	73
4.3.1 Characterization techniques	74
4.3.2 Structural properties of SiC films measured by XRD.....	81
4.3.3 Electrical properties of SiC films grown	

with constant N ₂ flow rate (1 sccm).....	84
4.3.4 Electrical properties of SiC films versus different N ₂ flow rates....	86
4.3.5 Surface morphology of SiC films examined by SEM and AFM....	87
4.3.6 Initial efforts on MEMS fabrication	90
4.4 Conclusion	91
4.5 References	92

CHAPTER 5. PATTERNING OF SiC THIN-FILM ON Si₃N₄/Si FOR

ROBUST MEMS APPLICATIONS.....	94
5.1 Sample preparation	94
5.2 Polishing of SiC thin-film	94
5.3 Photolithography and ITO liftoff	96
5.4 ICP etching of SiC thin-film	97
5.4.1 Sample loading.....	97
5.4.2 Plasma chemistries	98
5.4.3 Process parameters set-up.....	98
5.5 Results and discussion.....	100
5.5.1 Improvement of etching yield on polished SiC thin-films	100
5.5.2 Effects of ICP source power, RF chuck power and NF ₃ % on etch rate	101
5.5.3 Possibility to directly use photoresist as mask material	105
5.5.4 Initial efforts on SiC etching in ICP Cl ₂ /Ar discharges	107
5.6 Conclusion	108
5.7 References	110

CHAPTER 6. SiC THIN-FILM AS FABRY-PEROT INTERFEROMETER FOR FIBER-OPTIC TEMPERATURE SENSORS OPERATING IN HARSH ENVIRONMENT.....	111
6.1 Introduction	111
6.1.1 Motivation — Fiber-optic temperature sensors for flight control technologies.....	111
6.1.2 Poly-SiC for fiber-optic applications.....	113
6.2 Preliminary design of Fabry-Perot temperature sensor.....	114
6.2.1 Experimental approach.....	114
6.2.2 Principle of operation of a Fabry-Perot fiber-optic temperature sensor and its temperature sensitivity.....	115
6.3 Substrate selection.....	119
6.4 Growth of SiC thin-film on insulating sapphire substrate.....	120
6.4.1 Effect of film thickness on the structural properties.....	122
6.4.2 Effect of precursor flow rate on the structural properties.....	126
6.5 SiC temperature sensor characterization.....	131
6.5.1 Experimental setup.....	131
6.5.2 Effect of SiC thin-film thickness.....	133
6.5.3 Effect of SiC thin-film structure.....	137
6.5.4 Short-term stability test.....	141
6.6 Summary and Conclusion	142
6.7 References	144

CHAPTER 7. CONCLUSIONS & SUGGESTIONS FOR FUTURE WORK.....147

LIST OF FIGURES

<u>Fig. No.</u>	<u>Titles</u>	<u>Page</u>
CHAPTER 1		
1-1	Atomic structure of SiC: a) tetrahedrally bonded Si-C+ cluster b) Hexagonal bilayer with Si and C in alternating tetrahedrally coordinated sites.....	2
1-2	Crystal structure of different SiC polytypes displayed parallel to the (1120) plane: a) Zincblende structure (cubic 3C-SiC), b) hexagonal 4H-SiC and c) hexagonal 6H-SiC.....	2
1-3	Stacking order of different SiC polytypes: (a) 3C-SiC, (b) 4H-SiC and (c) 6H-SiC.....	2
1-4	Schematic of SiCOI structures: (a) SiC on insulating layer, (b) SiC on insulating substrate.....	4
1-5	A schematic of ICP process chamber.....	12
CHAPTER 2		
2-1	Processing flow chart designed for the fabrication of SiC films on insulators for robust MEMS applications.....	23
CHAPTER 3		
3-1	SiC growth techniques: (a)Lely, (b)Modified Lely (old), (c)Modified Lely (new).....	25
3-2	A schematic of different etching mechanisms. s, n, i, and e represent species at sample surface: neutral species, ions, and electrons; diff, abs, des, acc and sput stand for diffusion, absorption, desorption, acceleration and sputtering, respectively.....	33

3-3	Effect of pressure on the ion bombardment energy.....	35
3-4	Ion milling configuration.....	38
3-5	A schematic of RIE reaction chamber.....	39
3-6	A schematic of ECR reaction chamber.....	41
3-7	A schematic of Fabry-Perot interferometer.....	49

CHAPTER 4

4-1	Schematic diagram of the rapid thermal RTCVD system.....	65
4-2	A schematic arrangement of reaction chamber of the RTCVD system.....	66
4-3	Arrangement of the sample and Si wafer pieces on the quartz tray.....	69
4-4	Linear chain structure of a 3MS $[(CH_3)_3SiH]$ molecule.....	72
4-5	Recipe for SiC growth using 3MS.....	72
4-6	A schematic of X-ray diffractometer.....	75
4-7	Electron beam diagram when observing SEM image.....	77
4-8	SEM sample stubs.....	78
4-9	The Nanoscope Dimension TM with integrated acoustic/vibration isolation system manufactured by Digital Instruments in CA.....	79
4-10	Basic setup of Hall effect measurement.....	80
4-11	Normalized XRD spectra for SiC films grown on Si_3N_4/Si at different temperatures. Flow rates: 30 sccm 3MS, 1 sccm N_2	82
4-12	Normalized XRD intensity of the SiC (111) peak as a function of growth temperature. Flow rates constant at 30 sccm 3MS and 1 sccm N_2	82

4-13	XRD spectra of Si ₃ N ₄ layer un-annealed and annealed at the temperatures used for SiC growth.....	83
4-14	Normalized XRD intensity and FWHM of SiC (111) peak as a function of 3MS flow rate. Growth temperature is 1200°C and N ₂ flow rate is 1 sccm.....	84
4-15	Resistivity and sheet resistance of SiC films at 300K as a function of growth temperature. Flow rates: 30 sccm 3MS and 1 sccm N ₂	85
4-16	Resistivity and sheet resistance of SiC films at 300 K as a function of 3MS flow rate. Growth temperature: 1200°C, N ₂ flow rate: 1 sccm.....	85
4-17	Resistivity and sheet resistance of SiC films at 300K as a function of N ₂ flow rate: (a) growth temperature: 1200°C, 3MS flow rate: 40 sccm; (b) growth temperature: 1250°C, 3MS flow rate: 25 sccm.....	86
4-18	SEM micrographs of SiC thin films grown on Si ₃ N ₄ /Si structures with 30 sccm 3MS and 1 sccm N ₂ at the following temperatures: (a) 1100°C; (b) 1150°C; (c) 1200°C; (d) 1250°C.....	87
4-19	Growth rate and surface roughness of SiC films versus growth temperature. Flow rates: 30 sccm 3MS, 1 sccm N ₂	88
4-20	AFM micrographs of starting Si ₃ N ₄ /Si surface and SiC film surface grown at 1100°C and 1200°C. Flow rates: 30 sccm 3MS, 1 sccm N ₂	89
4-21	SEM micrographs of SiC MEMS structures: (a) film stress diagnostic indicator gauge; (b) residual stress cantilever beams.....	90

CHAPTER 5

- 5-1 SEM micrographs of SiC thin-film grown on Si₃N₄/Si at 1200 °C

(a) before polishing, (b) after 15 minutes polishing, and (c) after 90 minutes polishing by 0.1 μm diamond lapping films.....	95
5-2 Basic steps used to pattern and expose photoresist, and liftoff process.....	96
5-3 (a) Top view of 2" sample chuck; (b) small piece sample adhesive to a 2" Si wafer.....	97
5-4 ICP etching of unpolished and polished SiC thin-films grown on $\text{Si}_3\text{N}_4/\text{Si}$ with 40 sccm 3MS at 1200 $^{\circ}\text{C}$. ICP power/RF bias power: 300/40 W.....	100
5-5 ICP etching of unpolished and polished SiC thin-films grown on $\text{Si}_3\text{N}_4/\text{Si}$ with 40 sccm 3MS at 1200 $^{\circ}\text{C}$. ICP power/RF bias power: 200/40 W.....	100
5-6 Effect of ICP source power on etch rates of SiC thin-films with total gas flow rate of 15 sccm, while SiC thin-films were grown on $\text{Si}_3\text{N}_4/\text{Si}$ with 40 sccm 3MS at 1200 $^{\circ}\text{C}$	101
5-7 (a) Schematic of ICP etched $\text{SiC}/\text{Si}_3\text{N}_4/\text{Si}$ structure with ITO mask layer, and SEM micrographs of the etched SiC patterns in $10\text{NF}_3/5\text{Ar}$, 2 mTorr, 25 $^{\circ}\text{C}$ substrate temperature, 40W RF chuck power and (b) 100W, (c) 200W, (d) 300W ICP power discharges.....	102
5-8 Etch rates of SiC as a function of RF chuck power in $10\text{NF}_3/5\text{Ar}$, 2 mTorr, 25 $^{\circ}\text{C}$ substrate temperature, and 400 W ICP source power discharges.....	103
5-9 Effect of NF_3 % in NF_3/Ar on SiC removal rates.....	104
5-10 SEM micrographs (tilt 60 $^{\circ}$) of PR 1818 patterns on (a) polished SiC and (b) unpolished SiC films before ICP etching.....	106
5-11 SEM micrographs of SiC etched patterns after stripping off PR 1818.....	106
5-12 SEM micrographs of (a) PR patterns on SiC film before ICP etch and	

(b) etched SiC patterns in 20Cl ₂ /5Ar, 100/500 W RF/ICP powers	
discharges after stripping off PR1818.....	108
5-13 SEM micrographs of SiC surface micromachined MEMS	
structures: film stress diagnostic indicator gauges.....	109

CHAPTER 6

6-1 A schematic of the experimental approach.....	114
6-2 A schematic of the thin-film Fabry-Perot interferometer	
used for the temperature measurement.....	116
6-3 SiC thin- films grown on 1x1 cm ² sapphire substrate with (a) 40 sccm	
3MS for 8 min. and (b) 35 sccm 3MS for 12 min. at 1100 °C, which	
are semi-transparent to a flash light.....	121
6-4 XRD spectra of starting sapphire substrate and SiC films grown at 1100 °C.....	122
6-5 Dependence of XRD intensity and thickness-normalized XRD	
intensity of 3C-SiC (111) peaks on film thickness.....	122
6-6 AFM micrographs of 3D surface topology of the starting sapphire	
substrate and of SiC films with different thickness.....	124
6-7 RMS surface roughness of starting sapphire substrate and	
SiC films versus film thickness.....	125
6-8 SEM micrographs of SiC films with different thickness (a) 1.5 μm; (b) 2 μm.....	125
6-9 Effects of 3MS flow rate on growth rate and FWHM of 3C-SiC(111)	
XRD peak of SiC thin films grown on sapphire substrate at 1100 °C.....	126
6-10 Effect of 3MS flow rate on the XRD peak intensity of 3C-SiC (111) orientation.....	127

6-11	The SEM micrographs of SiC thin films grown on sapphire [0001] substrate with (a) 25 sccm, (b) 30 sccm, (c) 35 sccm, (d) 40 sccm, and (e) 45 sccm 3MS at 1100 °C.....	128
6-12	The AFM micrographs of (a) starting surface of sapphire substrate and surfaces of SiC films grown at 1100 °C with (b) 30 sccm, (c) 35 sccm, (d) 40 sccm and (e) 45 sccm 3MS for 16 min., 12 min., 8 min. and 9 min., respectively.....	129
6-13	Effects of 3MS flow rate on RMS surface roughness of SiC thin films, which is normalized to the film thickness.....	130
6-14	Sketch of the experimental set-up for temperature measurement.....	132
6-15	Spectra of temperature sensors using SiC thin films with different thickness over the wavelength range from 490 nm to 1050 nm.....	133
6-16	Spectra of SiC temperature sensor obtained at 22.2 °C and 546.5 °C. The shifts in resonance minima versus temperature were recorded. The $\lambda_m(T_0)$ near 692.8 nm at 22.2 °C is arbitrarily defined.....	135
6-17	Measured shifts in resonance minima, $\Delta\lambda_m$, versus measured temperature, T_M , for the SiC temperature sensor fitted to a linear function.....	135
6-18	Normalized resonant shifts, $\overline{\Delta\lambda_m}(T) = \frac{\lambda_m(T) - \lambda_m(T_0)}{\lambda_m(T_0)} \cdot 100\%$, versus measured temperature, T_M , for the SiC temperature sensor fitted to a quadratic function.....	136
6-19	The deviation of normalized resonant shifts, $\delta[\overline{\Delta\lambda_m}(T)]$, from the quadratic fit in Fig. 6-18, expressed in terms of the deviation of sensed temperature, ΔT_M , from measured temperature T_M	137
6-20	Sensor spectra: output spectra of SiC temperature sensors using SiC thin films	

grown on sapphire substrate with different 3MS flow rate. 490 nm < λ < 1050 nm.....	138
6-21 Normalized resonance shifts, $\overline{\Delta\lambda_m}(T) = 100\%[\lambda_m(T) - \lambda_m(T_0)]/\lambda_m(T_0)$, versus measured temperature for the SiC temperature sensors fitted to the quadratic functions. 3MS flow rate: 30 to 45 sccm.....	140
6-22 Effect of 3MS flow rate on the deviation of sensed temperature (i.e. temperature accuracy), ΔT_M , of the poly-SiC temperature sensors, expressed in term of measured temperature, T_M	140
6-23 Short-term stability measurement on one SiC sensor exposed to 532 °C in air for two weeks shows the random variations of temperature about the baseline temperature and a standard deviation of 0.97 °C.....	142

LIST OF TABLES

<u>Table No.</u>	<u>Titles</u>	<u>Page</u>
CHAPTER 1		
1-1	Properties of typical SiC polytypes and Si, GaAs, GaN.....	3
1-2	Typical physical properties of LPCVD Si ₃ N ₄ , Corning 1737F glass substrate, quartz, sapphire [0001] substrate, and 3C-SiC.....	5
1-3	Comparison of CVD and other thin film growth techniques.....	8
CHAPTER 3		
3-1	Plasma dry etch rates of SiC.....	44
CHAPTER 4		
4-1	Properties of SiO ₂ and Si ₃ N ₄ at 300 K.....	63

SiC Thin-Films on Insulating substrates for Robust MEMS Applications

A dissertation submitted to the
Division of Research and Advanced Studies
of the University of Cincinnati

in partial fulfillment of the requirements for the degree of

DOCTORATE OF PHILOSOPHY (Ph.D.)

in the Department of Electrical & Computer Engineering and Computer
Science of the College of Engineering

by

Lin Cheng
B.S., Wuhan University of Technology, China, 1988

Committee Chair: Prof. Andrew J. Steckl

April 23, 2003

CHAPTER 1. INTRODUCTION

As the conventional material for semiconductor devices, Si, is reaching the limits of its physical properties, replacement materials, such as silicon carbide (SiC), are being investigated for a new generation of robust semiconductor devices in harsh environment. First synthesized in the 20th century, SiC has been the subject of research for semiconductor applications for over 40 years ^[1]. The wide bandgap (2.2-3.4 eV), high thermal conductivity (3.2-4.9 W/cm K) ^[2], and robust mechanical properties make SiC attractive for many applications including high temperature, high power, or high frequency devices that are not possible using Si or GaAs. The high Young's modulus (700 GPa) and Knoop hardness (2480 kg/mm²) ^[2], chemical inertness, and radiation resistance of SiC also make it an excellent candidate for the fabrication of micro-electro-mechanical systems (MEMS) devices that need to operate at high temperature and high frequency as well as in harsh environments.

1.1 Silicon Carbide (SiC)

SiC is the only known binary compound of silicon (Si) and carbon (C). Both Si and C belong to group IV elements. They are bounded in SP³ hybridization bonds. The unit atomic and crystal structures of SiC are shown in Fig. 1-1 and Fig. 1-2 ^[3]. SiC takes many crystal forms with the same chemical composition because of different stacking orders (see Fig. 1-3) ^[4]. This phenomenon is called "polytypism". Each crystal structure is called "polytype".

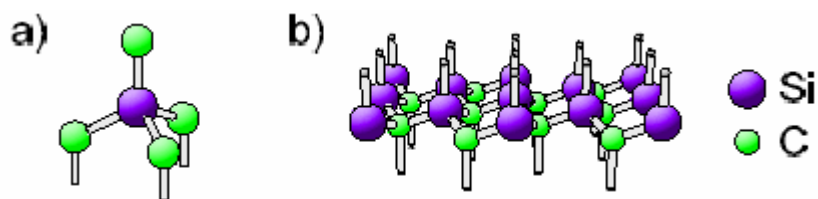


Figure 1-1. Atomic structure of SiC: a) tetrahedrally bonded Si-C+ cluster b) Hexagonal bilayer with Si and C in alternating tetrahedrally coordinated sites.

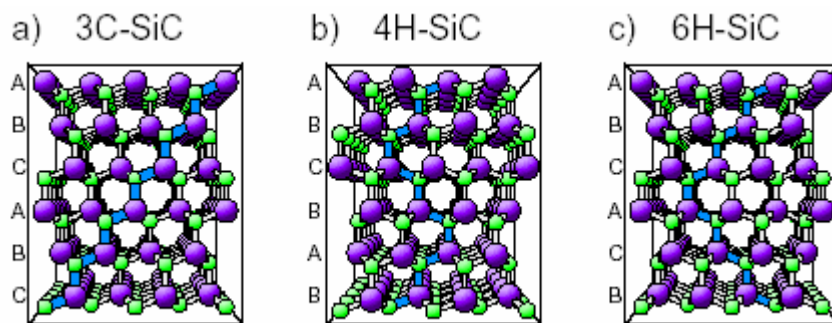


Figure 1-2. Crystal structure of different SiC polytypes displayed parallel to the (1120) plane: a) Zinkblende structure (cubic 3C-SiC), b) hexagonal 4H-SiC and c) hexagonal 6H-SiC.

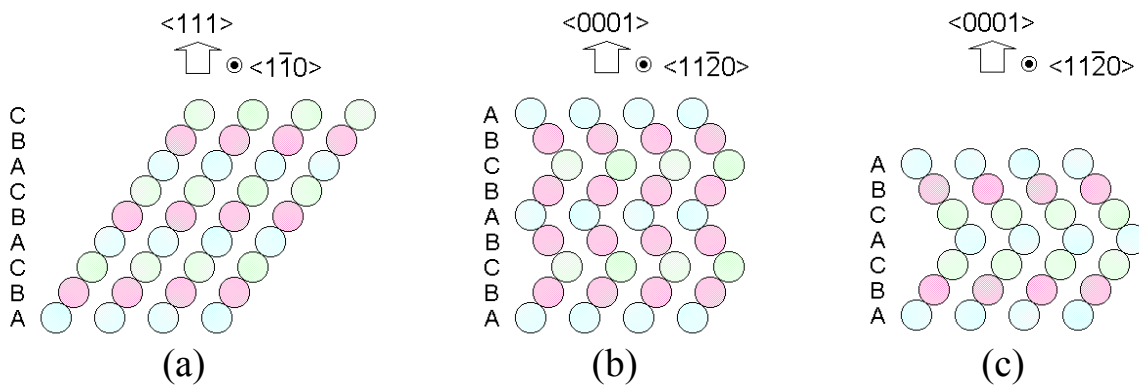


Figure 1-3 Stacking order of different SiC polytypes: (a) 3C-SiC, (b) 4H-SiC and (c) 6H-SiC.

Among more than 200 polytypes, the cubic (3C-) and hexagonal (4H- and 6H-) SiC are the most stable and common polytypes for device fabrication. Compared to 4H- and 6H-SiC epitaxial films, the 3C-SiC has the highest reported electron mobility. Table 1-1 gives a comparison of the properties of typical SiC polytypes, Si, GaAs and GaN [5].

Table 1-1. Properties of typical SiC polytypes and Si, GaAs, GaN

Property	3C-SiC (6H-SiC)	GaAs	Si	Diamond
Melting Point (°C)	Sublimes at 1825	1238	1415	Phase Change
Max. Operating Temp. (°C)	873 (1240)	460	300	1100
Thermal Conductivity (W/cm °C)	4.9	0.5	1.5	20
Thermal Expansion Coeff. (*10 ⁻⁶ °C ⁻¹)	3.8 (4.2)	6.9	2.6	
Young's Modulus (GPa)	448	75	190	1035
Physical Stability	Excellent	Fair	Good	Fair
Energy Gap (eV)	2.2 (2.9)	1.42	1.12	5.5
Electron Mobility (cm ² /V s)	1000 (500)	8500	1350	2200
Hole Mobility (cm ² /V s)	40 (50)	400	600	1600
Sat. Electron Drift Velocity (*10 ⁷ cm/s)	2.5 (2)	2	1	2.7
Breakdown Voltage (*10 ⁷ cm/s)	3 (4-6)	0.4	0.3	10
Dielectric Constant	9.7	13.2	11.9	5.5
Lattice constant (Å)	4.36	5.65	5.43	3.6

The biggest problem with the commercialization of SiC is the high cost and limited availability of bulk substrate. 6H and 4H bulk substrates for SiC are now

available, but their quality is still far from optimized. In December 2000, Hoya Corporation in Japan announced its first success in fabricating large monocrystal 3C-SiC substrates (up to 6" and at least 200 μm thick after removal of the Si base layer). But so far this 3C-SiC substrate is still not quite marketable. As a result, a lot of work is focusing on the synthesis of SiC in film-form on various substrates. From low-cost point of view, among 3C, 4H and 6H polytypes, heteroepitaxial growth of 3C-SiC films needs lowest growth temperature, in other words, lowest energy consumption, via chemical vapor deposition.

1.2 SiC on Insulating Substrates — SiCOI Structures

MEMS applications require that large-area uniform SiC films is formed on insulating or sacrificial layers^{[6], [7]}. Also the need for SiC on insulator structures is great, which has motivated researchers to borrow from SOI fabrication techniques in order to produce SiC-on-insulator substrates^[8]. The term “SiCOI” stands for Silicon Carbide on Insulating layers, which can be amorphous Si_3N_4 , SiO_2 or other oxide layers, or insulating substrates, which can be single-crystalline sapphire, high-temperature glass, or quartz. It usually represents a multi-layered structure. Fig. 1-4 shows a schematic of two kinds of SiCOI structures.

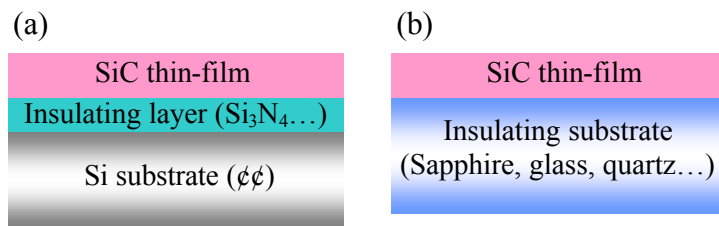


Figure 1-4. Schematic of SiCOI structures: (a) SiC on insulating layer, (b) SiC on insulating substrate.

The most important properties of insulating substrates are their thermal expansion coefficient and thermal softening point. They must be suitable for the conformal growth of SiC with small mismatch in thermal mechanical properties. Their high Young's modulus and high DC resistivity are also required to ensure the capability of device operating in harsh environment. Table 1-2 shows the comparison of some properties of

Table 1-2. Typical physical properties of LPCVD Si_3N_4 , [9], [10], [11] Corning 1737F glass substrate, [12] quartz, [11], [13] sapphire [0001] substrate, [14], [15] and 3C-SiC. [5], [16]

Material property	Si_3N_4 (LPCVD)	Corning 1737F glass	Quartz	Sapphire [0001]	3C-SiC
Density (g/cm ³)	3.17	2.54	2.2	3.98	3.166
Energy band-gap (eV)	~ 5.0	~ 9.0	9.0	9.0	2.3
Maximum operating temperature (°C)	1000	666 softening at 975	1120	~ 1800	873
Thermal expansion coefficient ($\times 10^{-6}/^\circ\text{C}$)	2.8	3.76 (0-300 °C) 4.2 (25-671 °C)	0.55	6.66 (C) 5 (⊥ C)	3.8
Thermal conductivity (W/cm·°C)	~ 0.02	~ 2.4	0.014	~ 0.42	4.9
Dielectric constant	~ 7	5.7	3.75	9.4 (⊥ C) 11.6 (C)	9.7
Index of refraction	2.15 – 2.30	1.515	1.46	1.76	2.6
Young's modulus (GPa)	270	~ 8	72	400	448
DC resistivity (? -cm)	10^{14} at 25 °C 2×10^{13} at 500°C	$\sim 5.6 \times 10^6$ RT to 300 °C	7×10^7 at 350°C	10^{16} at 25 °C 10^{11} at 500°C	0.01~100

low-pressure (LP) CVD Si₃N₄, Corning 1737F glass substrate, quartz, single-crystalline sapphire, and 3C-SiC. Compared to Corning 1737F glass substrate, LPCVD Si₃N₄ and sapphire [0001] substrates have much higher maximum operating temperature. Compared to quartz substrate, they have smaller mismatch in thermal expansion coefficient. They also possess higher Young's modulus and higher DC resistivity than Corning 1737 glass and quartz substrates. Therefore, LPCVD Si₃N₄ and sapphire [0001] substrates are more suitable for the fabrication of SiCOI structures.

SiC is considered to be a promising material for sensors, such as pressure, temperature, UV, and infrared sensors. When SiC is used as a sensor material, it provides the advantages of a large operating-temperature range and small thermal fluctuation due to its high thermal conductivity. SiC is also mechanically and chemically stable, so it can be used in the manufacture of sensors for use in extreme environments, such as high-temperature or corrosive environment.

Poly- or single-crystalline 3C-SiC films are being used for the fabrication of surface-micromachined MEMS. In contrast to Si, the dominant material nowadays, 3C-SiC has excellent mechanical hardness and electrical stability at temperature above 600°C [17], making it suitable for high temperature MEMS devices. Because the diameter of commercially available SiC substrates is at maximum 3? [18] and their cost is extremely high, heteroepitaxial SiC on foreign substrate with large area is very interesting and promising for subsequent device fabrication. With regards to single-crystalline 3C-SiC, the problem that still remains is how to obtain buffer layers of good enough quality to

achieve heteroepitaxial growth with low defect density [19], [20]. Polycrystalline SiC can be deposited on a variety of substrates, including nitride and native or thermal oxide layers, such as Si_3N_4 and SiO_2 that can be selectively etched away during device fabrication to obtain free standing membranes [17] or cantilever beams.

Since many suitable insulating substrates have amorphous or polycrystal structures, the direct growth of single-crystalline SiC thin film on such substrates is very complex and uneconomic. On the other hand, the ease of deposition and the ability to deposit amorphous or polycrystalline SiC thin film on many different substrates make it very attractive for many MEMS applications, particularly in connection with surface micro-machining fabrication techniques [8]. As reported, SiC has been deposited by plasma-enhanced (PE) CVD, sputtering, and electron beam evaporation at substrate temperatures ranging from 200°C to 1000°C [21], [22], [23]. These films are either amorphous, as in the case of low temperature PECVD, or polycrystalline with a low degree of texture and a temperature dependence to the distribution of grain orientations. Atmospheric-pressure (AP) CVD and LPCVD processes have also been used to deposit poly-SiC on electrically insulating substrates [6], [8]. APCVD and LPCVD techniques do not place limits on substrate size, and thus are well suited for producing ploy-SiC films for batch processing.

13. Chemical Vapor Deposition (CVD)

Chemical Vapor Deposition (CVD) is a materials synthesis process wherein one

or more gaseous precursors flowing over a heated solid surface can decompose or react to deposit as a solid film on a solid substrate. In other word, CVD is a thin-film formation technique that is easy to scale up and is widely used by industry. For example, if silane (SiH_4) is one such gas phase precursor, the silane molecules can hit the solid surface. Some of the silane molecules might be reflected back while others may be adsorbed on the surface. The adsorbed molecules, if supplied the right amount of energy, may decompose into Si and H_2 with the latter returning to the gas phase. The Si that is left behind can build up as a solid thin-film. Table 1-3 shows the comparison of CVD and other thin-film growth techniques.

Table 1-3. Comparison of CVD and other thin-film growth techniques

Advantages of CVD over other techniques:	Disadvantages:
<ol style="list-style-type: none"> 1. Thin and thick films of materials can be obtained well below their melting or decomposition temperature. 2. It is possible to obtain materials with extremely low impurity contents. 3. The growth rate can be varied over a wide range. 4. There are numerous reactant gases to choose from. 5. It is possible to deposit on a number of different substrates. 6. It is possible to obtain an extremely clean starting surface by in-situ etching the substrate prior to deposition. 	<ol style="list-style-type: none"> 1. It is necessary to optimize a large number of parameters that can affect the quality of the deposited material. 2. The gases used can be flammable, corrosive, and toxic. Precautions need to be taken to ensure safe handling. 3. The substrate temperatures are higher than PVD (such as MBE technique) or some other techniques.

The chemical reaction of the gases can take place either as a heterogeneous reaction, which is close to the heated substrate surface; or as a homogeneous reaction, which means that the reaction is in the gas phase. The former is desirable since it leads to the production of good quality films. The latter can lead to clusters of the deposited material dropping on sample surface, which results in bad quality films with poor film adhesion.

The process of chemical vapor deposition consists of several steps:

1. Transport of the gaseous species to the substrate surface through the boundary layer,
(Reactants diffuse to surface)
2. Adsorption/Chemisorption of some of the molecules on the substrate surface,
3. Heterogeneous reaction on the substrate surface (or Surface reaction to form final product or intermediate species),
4. Surface diffusion to form islands or clusters,
5. Desorption of the reaction by-products from substrate surface (or Diffusion of by-products away from surface),
6. Transport of the by-products through the boundary layer back to the gas phase and subsequent removal.

The slowest of these becomes the rate-limiting step. At low temperatures, the decomposition of the gaseous precursors or the rate of reaction on the substrate surface is usually lower than the reactant species to the surface. In this case, the deposition or the rate of reaction becomes the rate-limiting step and the reaction is *kinetically controlled*.

At high temperatures, the reactant species decompose and react as soon as they reach the substrate surface as a result of which the transport of species becomes the rate-limiting step. The deposition is now called to be mass-transport limited or *diffusion-controlled*.

The gas molecules decompose close to the heated surface and are transported to the substrate. They are adsorbed by weak van der Waals forces and then diffuse on the surface until they reach the sites where they can strongly bond to the substrate lattice by chemisorption. It has been shown that islands are obtained when a material with higher surface energy is grown on a substrate, which leads to subsequent three-dimensional growth. On the other hand, if the film being grown has a lower surface energy than the substrate, layer by layer (two-dimensional) growth can be achieved.

CVD has been widely used for heteroepitaxial and homoepotaxial growth of SiC thin-films on foreign and SiC substrates. There are two types of pressure dependent CVD processes, APCVD and LPCVD. Both of them have all been used for various applications. In general, APCVD is controlled by the rate of mass transport to the wafer, while LPCVD is controlled by the reaction rate at the sample surface. APCVD usually gives fast deposition rate but poor step coverage and contamination.^[24] The deposition rate of APCVD is also insensitive to small variations in temperature.^[25] Compared to APCVD, LPCVD has lower deposition rate but provides higher film uniformity and lower contamination level, which is good for depositing thinner films. The tradeoff to use LPCVD is that the high temperatures are required to get significant deposition rate.^[26] The deposition rate of LPCVD is also more sensitive to temperature variations than

APCVD. Therefore, for the growth of thin-films (a couple of μm) with high uniformity and low contamination level, an LPCVD system is more suitable than an APCVD system.

1.4 Inductively Coupled Plasma (ICP) Etching

There are a wide variety of device structures that have been fabricated in SiC, such as p-n junction and Schottky barrier diodes, bipolar junction transistors (BJTs), thyristors, metal-semiconductor field effect transistors (MESFETs), micro-sensors, and various optoelectronic and MEMS devices [27]. In all of these structures, the etching processes play the key role in achieving pattern transfer capability. Due to its chemical inertness, there is virtually no chemical etch that can attack SiC at room temperature. Chemical etching can proceed only at high temperatures: in molten salts (Na_2O_2 , NaOH , KOH , etc. at 500 °C), and in a flow of chlorine, chlorine-contained gases, and hydrogen (at > 1000 °C) [27]. At such high temperatures, the use of conventional photoresist, oxide, and metal masks is impossible. The main requirements of the etching process for device fabrication are as follows: (i) low temperatures, (ii) high quality of the surface treatment, (iii) high selectivity of etching with respect to the mask materials, and (iv) high resolution and anisotropy. To date, plasma etching is the most promising method for etching SiC.

Compared to ion milling, reactive ion etching (RIE), electron-cyclotron resonance (ECR) etching, inductively coupled plasma (ICP) etching offers an attractive alternative dry etching technique. As a common recognition, ICP sources are very promising for

large area, high ion density etching process. Fig. 1-5 shows a schematic of ICP process chamber. ICP plasmas are formed in a dielectric vessel encircled by inductive coil into which RF-power is applied. A strong magnetic field is induced in the center of the chamber, which generates high-density plasma due to the circular region of the electric field that exists concentric to the coil. Under the etching condition at low pressure (= 20 mTorr), the plasma diffuses from the generation region and drifts to the substrate at relatively low ion energy (<25 eV for Plasma Therm 790 Series). Thus ICP etching is expected to produce low damage while achieving high etching rate. In the mean time, anisotropic profiles are obtained by superimposing an RF-bias on the sample to independently control the ion energy.

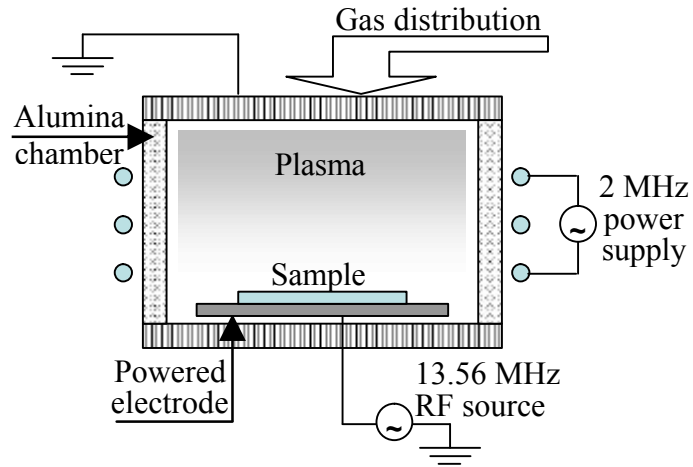


Figure 1-5. A schematic of ICP process chamber.

The principle of the ICP source operation is that the electrical field produced by the coils in the horizontal plane induces an oscillating magnetic field in the vertical plane, trapping electrons and producing high ionization and excitation efficiencies without leaking the electrons to the chamber wall. Therefore, as in an ICP source, the ion density is high while the induced self-bias on the cathode is low.

As shown in Fig. 1-5, a typical ICP system (Plasma Therm 790 series) has an RF power source operating at 2 MHz. The 2 MHz power is inductively coupled into the plasma volume to create a high ion density ($=10^{11} \text{ cm}^{-3}$) discharge. A second RF power supply (13.56 MHz) is used to control the ion energy. This is a prototypical single-wafer, high-density system, in which there is separate control of ion density (via the ICP power) and ion energy (via biasing of the sample position). The details about effects of process parameters on etch results will be addressed in Chapter 3.

1.5 SiC for MEMS and Sensors Operating in Harsh Environments

Many measurement and control applications that require micro-sensor and micro-actuator technologies are in the presence of harsh environments. Harsh environments include locations of high temperatures, intense vibrations, corrosive flows. Application fields characterized by harsh environments include aerospace, micro-propulsion, automotive, turbo-machinery, oil well/logging equipment, industrial process control, nuclear power, and communication. For example, optimized engine performance in aerospace and automotive systems requires a stable, high-temperature material, such as SiC, for solid-state sensors and electronics. The ability to deposit large area SiC thin-films on many different insulating substrates make the SiCOI structures fairly attractive for low-cost, robust, high-temperature applications in harsh environments.

A main focus area for SiC MEMS has been SiC sensor systems for combustion systems or gas turbine engines. To meet the efficiency, emissions, cost, and safety goals

set by military and commercial customers, the next generation of gas turbine designs require instrumentation in or near the hot-gas flow path, which must operate above 350 °C [8]. Sensors are needed for turbine development testing and in-flight service in order to measure combustor liner temperature, rotor and stator metal temperatures, internal cooling temperatures, steady-state and transient cooling flow and temperature, pressure and rate of change of pressure, hot gas path leakage, and coolant leakage. Conversion of electronic control and sensor systems from Si to SiC-based devices will not only increase efficiency and safety through enabling instrumentation by also reduce the overall weight of an aircraft by eliminating the packaging wiring and connectors necessary to line sensor systems with control electronics. This reduction would directly translate to increased range and lower fuel costs.

Most of the high-temperature sensors needed for gas turbine engines will find application areas in rocket technology to monitor combustion temperature, pressure, and by-products. Gas sensors sensitive to hydrogen are required for launch pad and in-flight safety systems, and gas sensors for hydrocarbon and CO₂ are needed for monitoring the condition of the cabin atmosphere in manned spacecraft. These sensor systems can be fabricated based on SiC technology.

SiC-based MEMS devices will benefit manned and unmanned spacecraft as well. Currently, unmanned spacecraft require thermal radiators to dissipate heat generated by on-board Si-based electronics. Implementation of SiC-based electronic systems, which can operate at temperatures above 350 °C, will eliminate the need for thermal radiators,

thus reducing the overall weight of the spacecraft. Additionally, SiC electronics and sensors are much less susceptible to radiation damage than their Si counterparts, thereby reducing the need for radiation shielding and, as a result, the spacecraft weight. Reduced spacecraft weight, and increased operating temperature and radiation resistance of on-board electronics and sensor systems, will dramatically increase the functionality of unmanned spacecraft, allowing them to more aggressively probe harsh planetary environments. Communication satellites will have extended operating lifetimes and the ability to carry more critical on-board electronic systems [8].

A family of high temperature SiC electronics and sensors that could function in hot areas of the aircraft would alleviate the above-mentioned technical obstacles to enable substantial aircraft performance gains. The NASA Glenn Chemical Species Gas Sensor team has been developing SiC-based high temperature gas sensors for aerospace applications. Based on their research, they concluded that [28] (1) un-cooled operation of 300 - 600 °C SiC electronics and sensors mounted would save weight and increase reliability by replacing hydraulic controls with "smart" electromechanical controls; (2) SiC-based distributed control electronics would eliminate 90% of the wiring and connectors needed in conventional sheltered-electronic aircraft control systems; (3) Even in non-hot areas of an aircraft, SiC electronics would enable the elimination of electronics cooling systems, such as the liquid cooling system employed in the air fighters, which add weight and reduce operational reliability of high-performance aircraft; (4) SiC electronics and sensors offer similar improvements to commercial jetliners, where increased fuel efficiency, weight savings, and reduced pollution carry particularly large

economic and environmental payoffs over an aircraft's multi-decade operational lifetime. Therefore, the use of advanced SiC control electronics would allow the aircraft to shed hundreds of pounds of weight, operate with increased capabilities and fuel efficiency, and operate more reliably with less maintenance and downtimes. It has been speculated that the economic savings value will be in the millions of dollars per aircraft.

1.6 References:

- [¹] For an excellent source of information, see SiC Materials and Devices, Y. S. Park, ed., *Semiconductors and Semimetals*, Vol. 52, Series Editors: R. K. Willardson and E. R. Weber, Academic Press, 1998.
- [²] Pasqualina M. Sarro, Sensors and Actuators, 82, pp. 210-218, 2000.
- [³] U. Starke, J. Bernhardt, J. Schardt, and K. Heinz, Surf. Rev. Lett., July 1999.
- [⁴] See also <http://matsunami.kuee.kyoto-u.ac.jp/~syu-naka/English/Polytype.html>
- [⁵] See also <http://matsunami.kuee.kyoto-u.ac.jp/~syu-naka/English/WhatIsSiC.html>
- [⁶] J. Chen, J. Scofield, A. J. Steckl, J. Electrochem. Soc., Vol. 147, p. 3845, 2000.
- [⁷] M. Mehregany, C. A. Zorman, N. Rajan, and C. H. Wu, Materials Sci. Forum, pp. 338-342, 541, 2000.
- [⁸] M. Mehregany, C. A. Zorman, N. Rajan, and C. H. Wu, Proc. IEEE, Vol. 86, No. 8, pp. 1594-1610, 1998.
- [⁹] “LPCVD Silicon Nitride (stoichiometric) Properties” by cpgrippo, can be found online by using google search engine.
- [¹⁰] “LPCVD Silicon Nitride (silicon-rich) Properties”, can be found online, http://web.mit.edu/6.777/www/materials/LPCVD_silicon_nitride_si/source1.html
- [¹¹] S. M. Sze, “Properties of SiO₂ and Si₃N₄ at 300 K” in *Physics of Semiconductor Devices*, 2nd ed., p. 852, A WILEY-INTERSCIENCE PUBLICATION, 1981.
- [¹²] Product information: CORNING: 1737F, <http://www.abrisa.com>, 200 South Hallock Drive, Santa Paula, CA 93003 Tel: (805) 525-4902, Fax: (805) 525-8604.
- [¹³] Fused Quartz Properties & Usage Guide, <http://www.quartz.com/gedata.html>, GE Willoughby Quartz Plant - Willoughby, OH.

-
- [¹⁴] Sapphire Table of General Properties, <http://www.mkt-intl.com>, *MarkeTech International*, Address: 4750 Magnolia St. Port Townsend WA 98368, Phone: 360-379-6707, Fax: 360-379-6907, Email: mkt@olympus.net
- [¹⁵] “AlGaN/GaN Transistor Application Notes - Substrate Selection”, *RF Nitro Communications Inc.*, 10420-F Harris Oaks Blvd., Charlotte, NC 28269, USA, Phone: (704) 596-9060, Fax: (704) 596-0950, Web: www.rfnitro.com.
- [¹⁶] “Development of Large 3C-SiC Mono-crystal Substrate for Semiconductor Devices”, *Hoya Advanced Semiconductor Technologies Co., Ltd.*, Address: 1-17-16 Tanashioda, Sagamihara-shi, Kanagawa 229-1125 Japan, Tel: 82-42-777-5405, Contact for technical aspects: Dr. Hiroyuki Nagasawa. <http://www.Hoya.co.jp/eng/randd/index.html>.
- [¹⁷] E. Hurtós, J. Rodríguez-Viejo, M. T. Clavaguera-Mora and K. Zekentes, “Nucleation behavior during the first stages of SiC growth on different substrates,” *J. Phys. IV France* 9, pp. Pr8-1069 to Pr8-1074, 1999.
- [¹⁸] “Silicon Carbide Substrates Product Specifications”, *Cree Inc.*, 4600 Silicon Drive, Durham, NC 27703, USA, Phone: (919)313-5300, Fax: (919)313-5451, Web: www.cree.com.
- [¹⁹] Nishino S., Powell J. A., Will H. A., *Appl. Phys. Lett.*, Vol. 42, pp. 460-462, 1983.
- [²⁰] Nagasawa H., Yamaguchi Y., *J. Crystal Growth*, Vol. 115, pp. 612-616, 1991.
- [²¹] G. Derst, S. Kalbitzer, G. Krotz, and G. Muller, “Preparation of crystalline SiC thin films by plasma-enhanced chemical vapor deposition and by ion beam modification of silicon,” *Mater. Sci. Eng.*, Vol. B11, pp. 79-82, 1992.
- [²²] J. Kobayashi, S. Yonekubo, K.Kamimura, and Y. Onuma, “Preparation of polycrystalline SiC thin films by RF magnetron sputtering using multi-target,” in *Silicon*

Carbide and related Materials, Vol. 142, S. Nakashima, H. Matsunami, S. Yoshida, and H. Harima, Eds. Bristol, UK: IOP Publishing, pp. 229-232, 1995.

[²³] Y. Onuma, S. Milyashita, Y. Nishibe, K. Kamimura, and K. Tezuka, "Thin film transistors using polycrystalline SiC," Amorphous and Crystalline Silicon Carbide II, M. M. Rahman, C. Y. Yang, and G. L. Harris, Eds. Berlin, Germany: Springer, Vol. 43, pp. 212-216, 1989.

[²⁴] Y-J Yang, "Thin Film Process", *Class notes of IC and MEMS Fabrication Process*, Dept. of Mechanical Engineering, National Taiwan University, See also <http://www-yjy.me.ntu.edu.tw/IC/6p.pdf>, 2002.

[²⁵] D. Richards, "Chemical Vapor Deposition", *Class notes of Semiconductor Material Processing (Lecture 14)*, Dept. of Chemical Engineering, Rensselaer Polytechnic Institute, See also <http://banyan.cie.rpi.edu/~class/SMP/cvd.pdf>, Fall, 2002

[²⁶] S. Gleixner, "CVD Reactors and Chemistries", *Class notes of Advanced Thin Film Processes (CemE/MatE 166)*, Dept. of Chemical and Materials Engineering, College of Engineering, San Jose State University, Fall, 2001.

[²⁷] For an excellent source of information, see Properties of Silicon Carbide, Gary L. Harris, ed., *Emis Datareviews Series*, No. 13, Published by: INSPEC, the Institution of Electrical Engineers, London, United Kingdom, 1995.

[²⁸] P. Neudeck, "Benefits of Silicon Carbide Electronics to Aircraft", NASA Glenn Research Center, Lewis Field, Cleveland, Ohio, Dec., 2001.
See also <http://www.grc.nasa.gov/WWW/SiC/aircraftbenefit.html>.

CHAPTER 2. OBJECTIVES

The thrust of this project is in four directions:

1. To optimize the growth conditions of SiC thin-films on several insulating layers or substrates for different MEMS applications.

SiC grown on different insulators, such as Si_3N_4 , Corning 1737 glass, quartz, and sapphire, suffers a large lattice mismatch and thermal mismatch, which result in stress in the SiC films. Although post-annealing may help to release the stress, the optimized growth conditions are required to minimize the effects of these differences on the film quality. Depending on the substrate properties and different device purposes, the optimized SiC growth conditions will be developed using an LPCVD system. In order to avoid the peeled and/or cracked film during the growth, the thickness of SiC thin-film has to be taken into account at the device design stage. According to the different MEMS applications, 0.5 to 3 μm thick SiC films are needed for device fabrication in this research.

2. To study the *in-situ* N_2 doping effect on the electrical properties of SiC films grown on amorphous, insulating Si_3N_4 layer.

As a wide band gap semiconductor, the electrical properties of SiC, which can be controlled by introducing various dopants with expected doping concentration, are the

most important issues to be considered during the device design. Among many dopants and different doping processes, *in-situ* N₂ doping of SiC films by chemical vapor deposition is the most convenient and effective way to achieve the goal. To date, most attention has been paid on the study of electrical properties of single crystal SiC. For many MEMS applications, single-crystal 4H-, 6H-, and 3C-SiC thin-films are not suitable to be directly deposited on a wide variety of insulating substrates or sacrificial layers. In this study, we need first to demonstrate the controllability of sheet resistance and resistivity of poly-SiC thin-films grown on insulating substrates. If successful, this approach will explore a new practical process to yield SiCOI substrates that can be of the same size as commercially available SOI substrates for the applications in electrically controlled MEMS devices. The results from our study should pave the way in determining the viability of this concept.

3. To study the ICP etching of the SiC thin-films grown on insulators in NF₃ and Cl₂ with Argon gaseous mixtures.

To fabricate SiC-based MEMS devices, selective etching is required to pattern the SiC films into the desired structural shapes. The absence of practical wet chemical etches for SiC has focused attention on the development of dry etching for device fabrication. Among plasma dry etching processes, ICP etching of single-crystal SiC in fluorine based chemicals is the most effective way to achieve high etch rate and low surface damage. The same technique can be used on ICP etching of poly-SiC grown on insulators. In this research, we will use the ICP Therm-790 system with

NF_3/Ar or Cl_2/Ar gaseous mixtures to develop the new patterning process for the fabrication of SiCOI-based MEMS devices. Since the structural density and bond strength of poly-SiC is supposed not to be the same as those of any polytype of single-crystal SiC, an initial effort to discover the opportunity for Cl_2 as an alternatively plasma chemistry for ICP etching of SiC will be conducted. The new processes for poly-SiC etches should differ to those for fabricating single-crystal SiC-based devices, in terms of power consumption and etch yields under certain conditions.

4. To explore the possibility of creating a fiber-optic temperature sensor by using poly-SiC thin-film Fabry-Perot interferometer grown on insulating transparent substrate.

The application of fiber-optic technologies to the measurement of physical parameters can alleviate many of the problems that are encountered when using electrical sensors.^{[1], [2]} The greatest advantage is obtained when electrically passive optical sensors are connected solely by fibers to their opto-electronic interfaces, which can be located in benign environments remote from the hostile measurement sites.^[3] Combining both advantages of fiber-optic technologies and robustness of SiC, it is very promising to create a SiC-based fiber-optic temperature sensor that can function well at harsh environment. The wide energy bandgap of SiC makes it visually transparent so that a light source in the range of visible wavelength can be used as the luminance source for the sensor operation. As a comparison, Si-based one has to operate with a light source in infrared wavelength range, which is more

expansive and needs an extra IR protection during the operation, due to its much narrow energy bandgap. The initial experimental results will also show the larger operating temperature range of SiC-based temperature sensor than that of Si-based one.

The overall experiment designed for this project is summarized in Fig. 2-1.

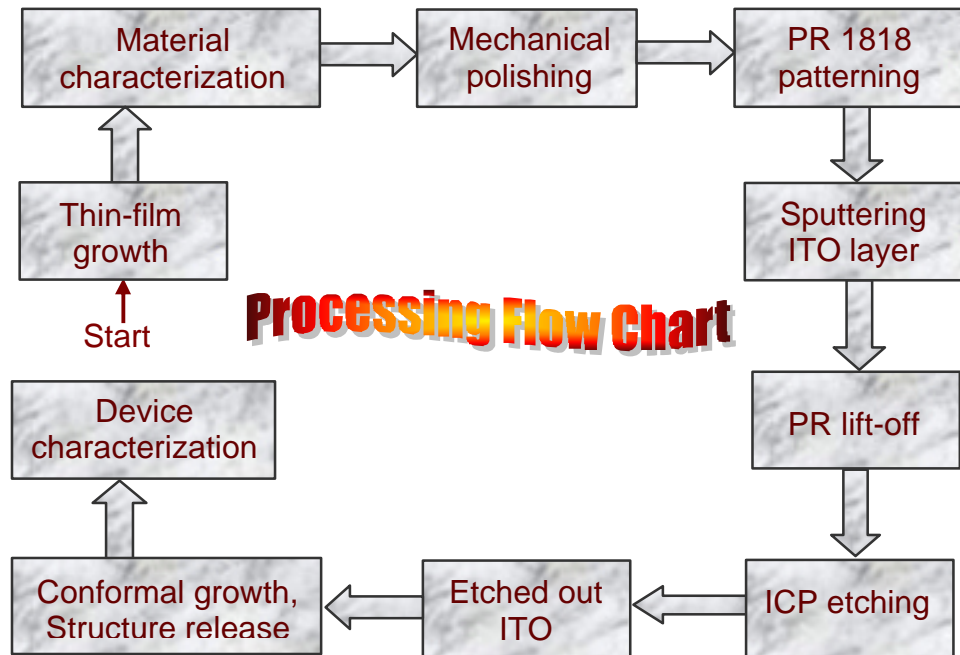


Figure 2-1. Processing flow chart designed for the fabrication of SiC films on insulators for robust MEMS applications.

References:

-
- [¹] T. G. Giallorenzi, J. A. Bucaro, A. Dandridge, G. H. Sigel, Jr., J. H. Cole, S. C. Rashleigh, and R. G. Priest, "Optical Fiber Sensor Technology," IEEE J. Quantum Electron. QE-18, 626, 1982.
 - [²] G. D. Pitt, P. Ectance, R. C. Neat, D. N. Batchelder, R. E. Jones, J. A. Barnett and R. H. Pratt, "Optical-Fiber Sensors," IEEE Proc. 132, Pt. J, 214, 1985.
 - [³] Glenn Beheim, "Fiber-Optic Temperature Sensor Using a Thin Film Fabry-Perot Interferometer," Ph.D. dissertation, Case Western Reserve University, Cleveland, Ohio, May, 1996

CHAPTER 3. LITERATURE REVIEW

SiC is probably the first semiconductor ever to be discovered. The substance was first reported in 1824 by a Swede, Jacob Berzelius. It does not appear to occur naturally on earth but has been identified in meteorites. So far, more than 200 polytypes of SiC have been discovered. The main polytypes of interest are 3C, 2H, 4H, 6H, and 15R.

With the development of the electric smelting furnace, it became possible to grow crystals and around 1885, Acheson grew a crystal and recognized it as a silicide of carbon, which these days is known by convention as carbide of silicon – silicon carbide (SiC). The first light emitting diode operation was discovered in SiC way back in 1907. The major development in SiC took place nearly 70 years later when, in 1955, Lely proposed a new method, based on the sublimation of SiC, for growing high quality bulk crystals. In the 1970s, Y. Tairov and colleagues at the Saint-Petersburg University modified the Lely process by using a seed crystal for SiC growth. This “Modified Lely process”, as shown in Fig. 3-1, is now the main technique for SiC bulk crystal growth worldwide.

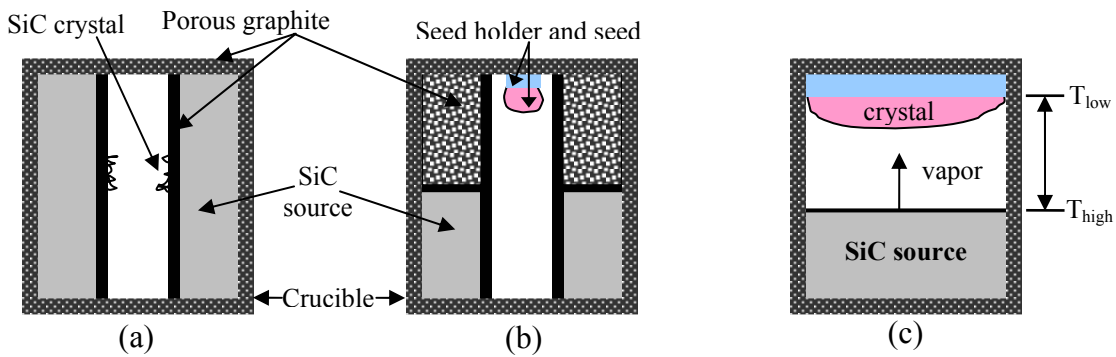


Figure 3-1. SiC growth techniques: (a)Lely, (b)Modified Lely (old), (c)Modified Lely (new)

3.1 Growth of SiC Thin Film on Insulators

Growth of bulk single crystal SiC is difficult because the processing temperature is required to be greater than 1800 °C. As a result, growth-from-melt techniques (such as those used for Si or GaAs) are not applicable. Meanwhile, although it is possible to obtain both p and n-type, semi-insulating substrates are presently not commercially available. Moreover, the size of SiC wafers is limited to less than three inches and their quality still needs a lot of improvement for device fabrication. A major problem is the presence of defects called micropipes. Furthermore, their highly prohibitive cost is another problem. For example, a single three inch 6H-SiC wafer can cost more than \$3,000 and a single two inch 6H-SiC wafer is at least \$700. These promote the investigation on epitaxial growth of SiC thin-films on foreign substrates.

Thin-films of various polytypes of SiC have been grown on different substrates, such as α -SiC, sapphire, Si, and quartz. The technique of choice is invariably chemical vapor deposition (CVD), although other techniques such as sputtering, laser ablation, and MBE, have also been used. CVD is also the best way for conformal growth on three-dimensional (3D) structures. Comparing with other polytypes of interest, growth of 3C-SiC thin-film requires the lowest growth temperature by LPCVD or APCVD. 3C-SiC grown on Si is now available commercially. But, this material suffers from a large number of defects which arise primarily due to the large lattice mismatch ($\sim 20\%$) and their large thermal expansion coefficient mismatch ($\sim 50\%$) between SiC and Si.

3.1.1 Chemical vapor deposition (CVD)

Chemical vapor deposition (CVD) is a very important thin-film deposition technique in the microelectronics industry and other industries that make use of thin-film coatings.^[1] The CVD process includes precursor transport, chemical reactions, and surface interactions. There are two limiting cases for CVD: the high-pressure and low-pressure CVD processes. For the high-pressure CVD process, the mean free path of the precursor is much smaller than the characteristic length of the surface features. In other words, the Knudsen number, which is defined as the ratio of the mean free path of the precursor to the characteristic length of the surface features, is small. Therefore the high-pressure CVD process is a hydrodynamic process. For low-pressure CVD, since the mean free path of the precursor is much larger than the characteristic length of the surface features, the process can be described by ballistic transport.^[2]

Several researchers have studied surface morphology or morphological stability issues for the small Knudsen number case (pressure \sim 10–760 Torr).^{[3], [4], [5], [6], [7], [8]} In these studies, gas transport was taken into account by using a continuum diffusion equation,* and it was assumed that the gas-film interface reaches quasi-thermal equilibrium. In other words, the effects of surface diffusion, gas diffusion, capillarity,

* Here, the model assumes a two-dimensional surface described by a height function $h(\mathbf{r},t)$, where $\mathbf{r}=(x,y)$. We denote the overall flux of n th-order particles at in-plane position \mathbf{r} at time t by $F_n(\mathbf{r},t)$. The surface evolution is then described by the following continuum equation:

$$\frac{\partial h}{\partial t} = \nu \nabla^2 h - \kappa \nabla^4 h \mp \sqrt{1 + (\nabla h)^2} + [s_0 F_0(\mathbf{r},t) + s_1 F_1(\mathbf{r},t) + \dots] + \eta,$$
 where $\nabla^2 h$ is the condensation/evaporation term, $-\kappa \nabla^4 h$ is the surface diffusion term, and η is the noise term. For more details, please see Ref. 1.

surface reactions, and the curvature of the film are all taken into account in the framework of continuum theory. Particularly, Bales et al. have shown theoretically that, in the diffusion-limited growth regime, the surface is not stable and has a fingerlike (column tip) morphology in the fast surface kinetics regime.^[5] In the reaction-limited growth regime, the surface should, theoretically, exhibit Kardar-Parisi-Zhang (KPZ) type growth,^{[8], [9]} a simplest possible interface model for both surface tension and lateral growth, but so far there has been no experimental evidence to support this claim. This could be due to complications caused by flow transport.

In the large-Knudsen-number case, i.e., the LPCVD process, researchers have used the idea of ballistic transport of an ideal gas to study trench or via filling problems for many years.^{[8],[10],[11],[12],[13],[14],[15],[16]} They have shown that, since the Knudsen number is large, collisions of precursors within the trench or via can be neglected. This kind of line-of-sight model can explain very well the features observed in trench evolution, although the details of the model may vary. However, surface morphological evolution governed by this kind of dynamics has only recently been studied.^[17]

Thin-film deposition at temperatures, which are as low as possible, is one of the key technologies for next generation of ultra-large scale integrated circuit (ULSI) fabrication.^[18] It can improve the device performance by reducing the damage and stress during the deposition. The definition and processing of microelectronic devices have been well established. The main challenge is to grow semiconductor thin-films, such as SiC, on foreign substrates or layers with reasonable high growth rate, good surface

morphology and low stress.

3.1.2 SiC thin-film grown on insulators by CVD

Historically, research in SiC growth has mainly focused on heteroepitaxy of single crystalline 3C-SiC on Si substrate and homoepitaxy of hexagonal polytypes for electronic device applications [19]. However, SiC has shown great promise as a micromechanical material for harsh environments because of its excellent electrical, chemical and mechanical properties [20]. The MEMS applications demand that large area uniform SiC thin-films on structured sacrificial layers such as SiO₂, Si₃N₄, and poly-Si for batch processing, which is essential in making SiC MEMS cost competitive. SiO₂, Si₃N₄, poly-Si, or a stack of these films can be easily deposited or purchased commercially. The ability to directly deposit SiC on optically transparent substrates also makes SiC very attractive for fiber-optic MEMS applications.

The fabrication of such SiC-on-insulator (SiCOI) structures was first realized on sapphire substrates: direct deposition on sapphire [21], [22], SiC deposition on Si on sapphire (SOS) [23], and on AlN on sapphire [24], and SiC growth on Si followed by removal of the substrate and attachment of the SiC film to a sapphire substrate [25]. The sapphire substrate approach was subsequently followed by the use of Si substrates to form SiCOI on Si: carbonization of Si SOI followed by SiC growth [26], wafer bonding [27], [28], and the Smart-Cut process [29], [30].

The fabrication of large area SiC SOI structures is most practical and cost-effective through the use of Si substrates. However, the techniques developed so far, SiC wafer bonding and direct carbonization techniques, still present some difficult processing issues. SiC wafer bonding is prone to the formation of air bubbles at the bonding interface which can cause SiC layer to peel off during the etch-back of the Si substrate. The high temperature (1300 °C) used in direct carbonization of Si SOI by propane usually damages the thin Si layer due to H etching and thermal evaporation. This can expose the SiO₂ to the propane ambient. At this high temperature, SiO₂ dissociates and the bottom Si substrate is exposed to reaction with propane, which generates voids in the Si substrate.

Direct growth of SiC on SiO₂, Si₃N₄, and poly-Si by CVD is an attractive process for obtaining large area SiC on sacrificial and insulating layers. Previously, the growth of randomly oriented polycrystalline SiC on SiO₂ and Si₃N₄ by atmospheric pressure CVD from the SiH₄/C₃H₈/H₂ gas system has been reported.^[31] By using tetramethylsilane and low pressure CVD, Rodriguez-Vieho *et al.* reported that <111> oriented polycrystalline SiC film can be grown on SiO₂^[32] and Kim *et al.* reported that single crystalline SiC can be grown on Si₃N₄.^[33] In this study, SiC films have been directly grown on low-stress and amorphous Si₃N₄/Si, poly-Si/SiC/Si₃N₄/Si, Corning 1737F glass, quartz and single-crystal sapphire [0001] substrates for robust MEMS and high-temperature fiber-optic applications. The details will be addressed in the following chapters.

3.2 Planarization of SiC Thin-Film

The planarization of surfaces plays a key role in the micro-fabrication of SiC devices. So far, post-processing of CVD SiC is still presenting many challenges for wafer surface finishing because of its very high hardness, which is second only to diamond^[34], and remarkable chemical inertness. During the device fabrication, such as wafer bonding, mask layer deposition or spin-on coating, surface roughness of less than 20 nm with good surface flatness and morphology is required for a reliable bond between a device layer and substrate, two device layers, or a mask layer and a device layer.

Existing surface polishing techniques can be categorized as purely mechanical, chemo-mechanical, or etching. Mechanical polishing of SiC wafers primarily uses diamond-polishing compounds mixed with water. Chemical-Mechanical Polishing (CMP) combines mechanical polishing with chemical etching actions, and has been shown to be very effective and can achieve very high smoothness^[35]. However, due to the chemical inertness of SiC, CMP is not yet available to improve the surface smoothness of SiC to the level adequate for direct wafer bonding. Thus, the current planarization technique relies mainly on mechanical polishing (lapping), which is a tedious process and currently suffers from low yields due to the wafer bow caused by residual stresses in SiC.

3.3 Plasma Etching of SiC

The word “plasma” comes from the Greek, meaning “something molded” [36]. To the physicist, plasma is an ionized gas with equal numbers of free positive and negative charges. The free charge is produced by the passage of electric current through the discharge. For most plasma of interest for etching, the extent of ionization is very small. Typically there is only one charged particle per 100,000 to 1,000,000 neutral atoms and molecules. The positive charge is mostly in the form of singly ionized neutrals, (i.e., atoms, radicals or molecules) from which a single electron has been stripped (removed). The majority of negatively charged particles are usually free electrons, although in very electronegative gases such as chlorine, negative ions can be more abundant.

3.3.1 Basic mechanism of plasma etching

In a plasma, two kinds of active species are produced, neutrals and ions. Neutrals are very reactive, on the other hand ions are usually less reactive but their kinetic energy can be controlled by substrate bias. The schematic of the different etching mechanisms is shown in Fig. 3-2.

1. Sputtering

Positive ions are accelerated through sheath region and strike the substrate with high kinetic energy [37].

$$E_{Max} = \frac{(QE_0)^2}{8\pi^2 f^2 M} \quad (\text{eV}),$$

where Q is the ionic charge, E_0 represents the RF field (kV/cm), M is the mass of ion, and f is the RF frequency (MHz).

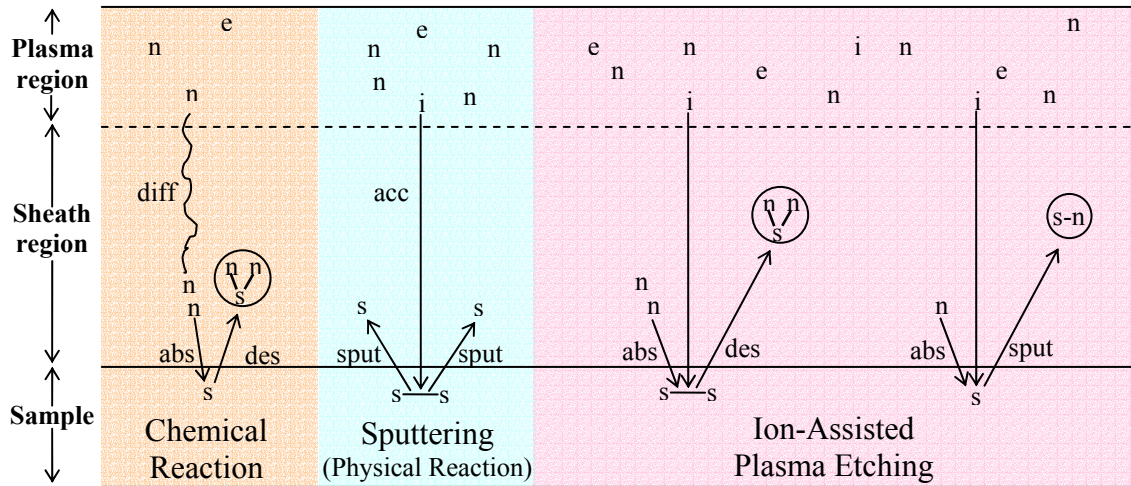


Figure 3-2. A schematic of different etching mechanisms. s, n, i, and e represent for atoms at sample surface, neutral species, ions, and electrons; diff, abs, des, acc and sput stand for diffusion, absorption, desorption, acceleration and sputtering, respectively.

By momentum conservation law, some of this energy is transferred to surface atoms that are then ejected, leading to material removal. This is mechanical interaction and the sputtering rate^[38] is

$$R = \frac{62.2 * s * j * W}{\rho},$$

where s is etching yield, j is ion flux (mA/cm^2), W is atomic weight (g/mol) and ρ is material density (g/cm^3).

Sputtering is unselective etching because the ion energy required to eject material is large compared to differences in surface bond energies and chemical reactivity. Due to the biasing voltage applied to the substrate, the flux of ions is vertical and this kind of etching is anisotropic.

2. Chemical reaction

This etching comes about when active species (neutral) from the gas phase are absorbed in the surface material and react with it to form a volatile product. High product volatile is essential. The evaporation rates of a material^[38] is

$$\mu_A = \alpha \left[\frac{M}{2\pi RT} \right]^{-\frac{1}{2}} P ,$$

where α is the material-dependent efficiency factor, usually between 0.1 and 1.0, M is the molecular weight and P is vapor pressure.

Without volatility, the reaction products would coat the surface and prevent gaseous species from reacting with it, therefore cut off the etching reaction. Chemical etching provides very high selectivity, but is non-directional providing an isotropic etch.

3. Ion-assisted plasma etching

The substrates are exposed to suitable neutral species in the presence of ion bombardment. The combination between sputtering and chemical reaction results in material removal rates exceeding the sum of separate chemical attack and sputtering. There are two mechanisms in ion-assisted etching.

(a) Ion-enhanced energetic etching

Neutral species cause little or no etching without ion bombardment. Ions damage the substrate material. They create high roughness that increases the exposed surface, and dangling atomic bonds at the surface that increase the number of absorption site.

Since ions are accelerated and strike the surface vertically, the etching induced is directional.

(b) Ion-enhanced inhibitor mechanism

Etching by neutrals takes place spontaneously. Ion bombardment does not cause any etching reaction. However, residues can coat the substrate surface and prevent the etching reaction from taking place. The ion flux at normal incidence keeps areas clear of inhibitor film on the horizontal surfaces, while vertical sidewalls are coated with an inhibitor film that prevents chemical attacks. The inhibitor-forming species may generate from feed gas, feed gas additives, sputtered reactor material or resist mask.

3.3.2 Plasma etching parameters

1. Effect of pressure

The mean free path of particle is inversely proportional to pressure. At higher pressure, the mean free path is shorter causing more frequent collisions of electrons. The electrons will lose their energy and create more reactive neutral species during the collision (generate higher plasma density).

Then the etch mechanism is more

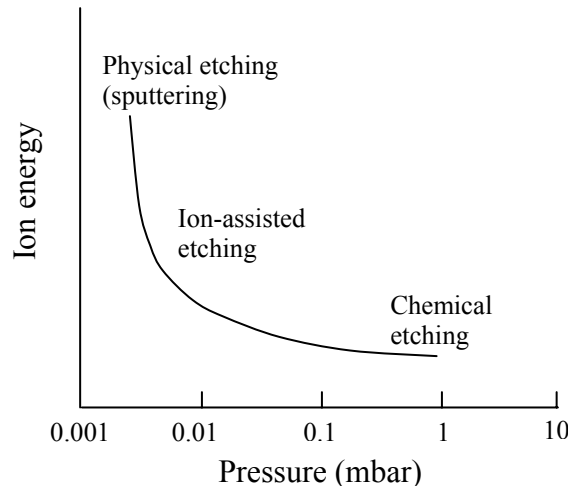


Figure 3-3. Effect of pressure on the ion bombardment energy. [38]

dominated by chemical reactions than physical (sputtering) removal, as shown in Fig. 3-3.

As the pressure is lowered, the characteristic potentials across the sheaths and the voltage applied to a discharge increase sharply. The rise in potential translates into a higher energetic ion flux to substrate surfaces. Sputtering does not take place until the ion energy exceeds the material-ion (molecule) threshold energy. When the physical reaction dominates the etching process, more surface damage will occur and the selectivity of mask material over etched sample will be also decreased.

For example, at low pressures (2~3 mTorr), the selectivity of AZ5209E photoresist (PR) over 6H-SiC in $10\text{NF}_3/5\text{O}_2$ discharge has the minimum (about zero)^[39] mainly due to an absence of ion collisions and recombination of ion and electron. The etch rate of PR is mostly dominated by physical reaction. On the other hand, as expected, the etch rate depends strongly on process pressure since the chemical component is enhanced at higher pressure. The neutral density is about 10^{13} cm^{-3} at 5 mTorr,^[40] and with a gas such as Cl_2 , a higher pressure should increase the etch rate. Selectivity to photoresist increases with increasing process pressure.

Purely chemical etching results in isotropic profile but low surface damage, while purely physical etching gives anisotropic profile but high surface damage. To take advantage of both mechanisms, ion-assisted etching under the pressure of several to several tens of mTorr can achieve anisotropic profile. Meanwhile, low surface

damage can be kept by controlling the process pressure and other parameters to control both physical and chemical reactions during etching process.

2. Effect of ion energy controlled by RF power supply

Increasing the ion energy in a plasma etch system typically results in anisotropic, high etching rate due to the physical sputter desorption of the etch products. However, bombardment of semiconductor surfaces with energetic ions generated during plasma etching can damage the near surface region and produce lattice damage if the ion energy is greater than the displacement energy of the host atoms. As these energetic ions strike the sample, damage as deep as 100 nm can occur and cause degradation of device performance. This damage can include simple Frenkel pairs consisting of a vacancy and the displaced atom, implanted etchant, broken bonds, formation of dangling bonds, or deposition. Attempts to minimize the damage by reducing the ion energy below the damage threshold for compound semiconductors (<40 eV) or by increasing the chemical component during the etching process can result in more isotropic profiles. These significantly limit minimum device dimensions and reduce the etch rates. It is therefore necessary to develop plasma-etch processes which couple high etch rates, anisotropy, and sidewall profile control with low damage for optimum device performance.

3. Effect of temperature

The chemical reaction is a function of temperature as $e^{-E_a/RT}$, where E_a is activation energy, R is gas constant and T is temperature in Kelvin. Thus, the

temperature has a dominant effect in selectivity, etch rates, and degradation of the resist mask. Temperature can affect structure of some oxide masks as well, such as indium-tin-oxide (ITO). ITO can be annealed and re-crystallized at relatively high temperature (>100 °C). If ITO film acts as a sacrificial layer, it is very difficult to chemically remove an annealed ITO mask layer after plasma etching.

4. Effect of loading

Since the arrival rate of reactive species at the sample surface controls the etch rate, a high generation rate of reactive species is required for a high etch rate. The generation rate R is defined as $R=kn_eN$, where k, n_e and N are the reaction rate constant for ionization, electron density and neutral density, respectively.^[41] The loading effect is the decreasing of etch rate when there are more etchable substrates placed in a reactor. The etch rate is usually proportional to etchant concentration that decreases with increasing the area of etchable surface in the plasma.

3.3.3 Plasma reactors

1. Ion milling

Ion milling is a purely physical process. The common gas used is Ar. The ion density and ion energy are separately controlled by the filament current and the accelerated voltage adjustment, as seen in Fig. 3-4.^[42] This process employs high energetic inert ion to erode the surface of material by bombardment, causing high surface damage and degrade the performance of the device.

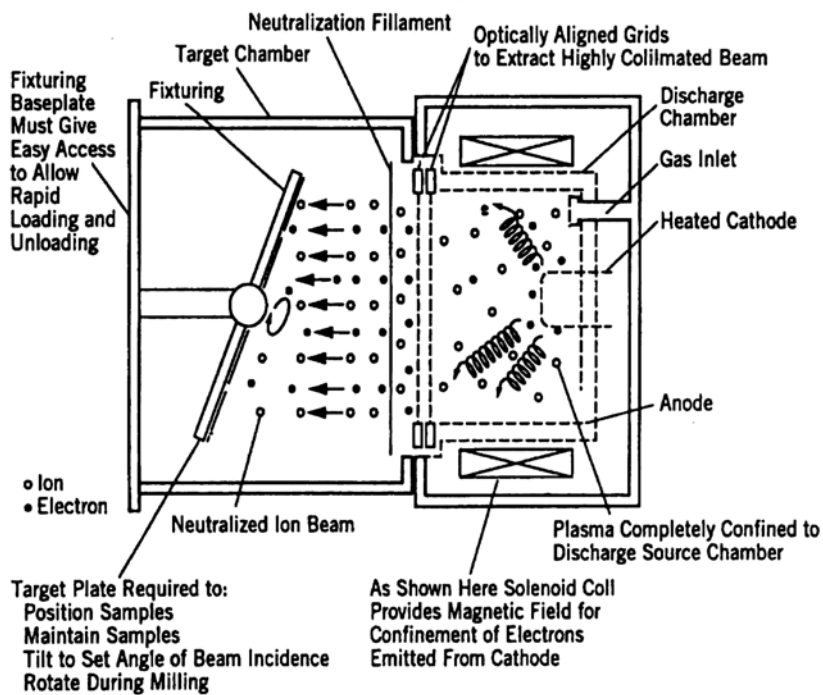


Figure 3-4. Ion milling configuration.

2. Reactive ion etching (RIE)

Reactive ion etching technique generates the plasma at a radio frequency of 13.56 MHz between two parallel electrodes in a reactive gas, as shown in Fig. 3-5. The electrons are accelerated and collide with gas molecules. The substrate is placed on the powered electrode. In this case, a large negative DC self-bias develops on the sample and attracts ions from plasma

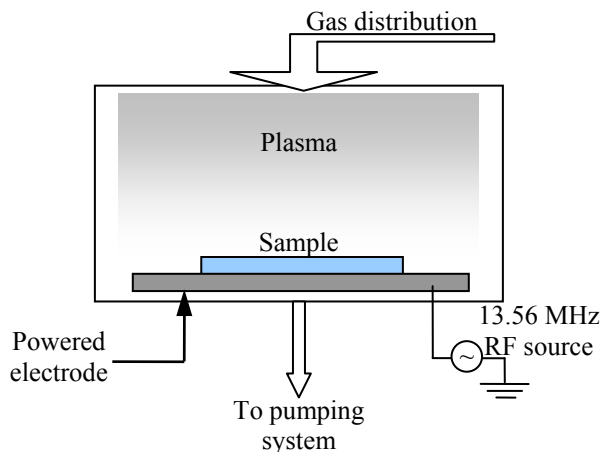


Figure 3-5. A schematic of RIE reaction chamber.

which cause damage on the surface. This results in a high anisotropic etch rate. However, highly energetic ions damage the sample surface and degrade both electrical and optical device performances.

3. Electron-cyclotron resonance (ECR)

Due to the surface damage from high energetic ions, high-density plasma is interesting. The ECR discharge is a low pressure and low temperature microwave plasma processing.^[41] Its ability to create high densities of charged and excited species at low pressures ($<10^{-4}$ Torr) make it an attractive processing discharge in etching and thin-film deposition applications. Low plasma potentials and ion energies can be obtained due to magnetic confinement of electrons in the source region. Therefore, the surface damage in ECR is less than RIE technique.

The frequency of orbital motion of electrons, confined under the action of an external magnetic field (875 Gauss), is equivalent to the drive frequency of 2.45 GHz leading to the occurrence of resonance, so-called electron cyclotron resonance, if this frequency of power is applied to the plasma. In this condition, outer-shell electrons from gas molecules in the discharge may also be liberated, leading to a very high degree of ionization in the plasma. ECR provides high ion density ($10^{10} \sim 10^{12} \text{ cm}^{-3}$), compared with RIE (10^9 cm^{-3}), without inducing high damage on the sample because the magnetic confinement of electrons results in low plasma potential.

ECR can also control the ion energy and ion flux independently. Fig. 3-6 shows a

schematic of ECR reaction chamber. Ion energy is controlled by RF or DC biasing at the substrate holder, while the ion and neutral flux are controlled by microwave and gas pressure. On the other hand, ECR etching also

has some disadvantages:

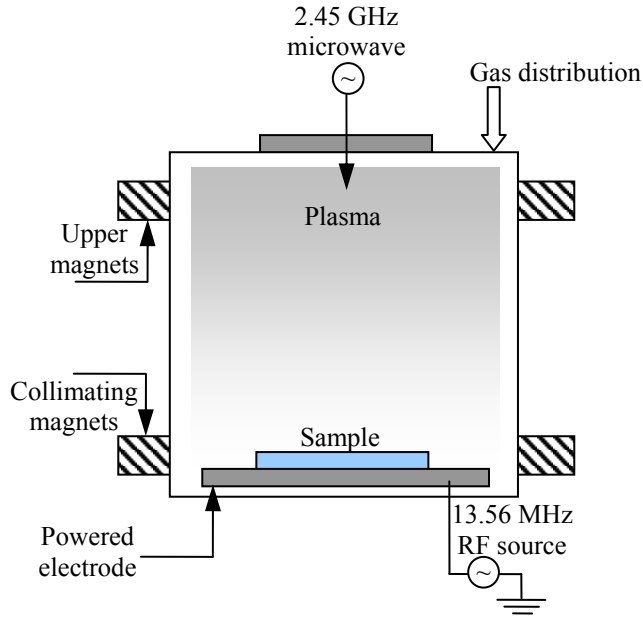


Figure 3-6. A schematic of ECR reaction chamber.

- Expensive and complicated for equipment setup
- Not suitable for shallow etch depth in electronic devices
- Create more roughness
- May alter stoichiometry at near sample surface

4. Inductively coupled plasma (ICP)

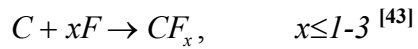
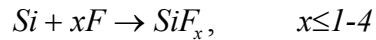
Inductively coupled-plasma etching offers an alternative high-density plasma technique where plasmas are formed in a dielectric vessel encircled by an inductive coil into which RF power is applied, as shown in Fig. 1-5. A strong magnetic field is induced in the center of the chamber, which generates high-density plasma due to the circular region of the electric field that exists concentric to the coil. The electrons in circular path will have only a small chance to be lost to the chamber wall resulting in

low DC self bias. At low pressures (≤ 20 mTorr), the plasma diffuses from the generation region and drifts to the substrate with relatively low ion energy (<25 eV). Thus ICP etching is expected to produce low damage while achieving high etch rates. Anisotropic profiles are obtained by superimposing a RF bias on the sample to independently control ion energy, while ion scattering and lateral etching can be minimized by using low-pressure conditions. ICP sources may be easier to scale up than ECR sources and are more economical in terms of cost and power requirements.

3.3.4 Plasma etching of SiC

In order to etch SiC in a plasma reactor, the chemistry used must be reactive with SiC. The species produced by the chemical reactions must be volatile compounds under the selected temperature and pressure condition to avoid the residue on the surface.

Several chemistries were examined, as shown in Table 3-1. The most effective gas for etching SiC is based with fluorine chemistry. The reaction mechanism of SiC in F-based chemistry is shown as follows:



J. J. Wang et al. ^[44] showed the data from optical emission spectra that ion bombardment plays a role in etch mechanism. When silicon atoms are etched away by

fluoride, a carbon layer is assumed to be on the exposed surface and removed by ion bombardment.

Various gas additives can have effects on the etch behavior. Oxygen has often been added to fluorine-based chemistries under RIE conditions to enhance the active fluorine concentration and increase the SiC etch rate [45], [46]. In ECR condition, there is only little change from O₂ addition to NF₃ or SF₆ in the atomic fluorine concentration [47]. In contrast, the addition of H₂ to the gas mixture reduces the etch rate [47], [48]. The introduction of hydrogen into the plasma prevents residue formation through a combination of mechanisms, including the formation of volatile alane (AlH₃) and the removal of the C-rich surface [49].

The difference in the etch rates of SiC is due more to differences in the dangling bond densities and the corresponding reactivity of the crystal faces than to the different crystal structure. For example, each atom on cubic (001) face has two dangling bonds, whereas only one dangling bond exists on a (111) face or similarly on the (0001) face of hexagonal SiC [50].

There is no measurable difference in etch rates between n⁺ and p⁺ SiC indicating the Fermi-level effects play no role in the etch mechanism under ICP conditions [44]. However, with the RIE technique, the etch rate increases when the n-type doping increases. [46]

Table 3-1. Plasma dry etch rates of SiC

Reactor	SiC	Gas	Conditions at highest ER	ER (Å/min)
RIE	6H	CHF ₃ /O ₂	20 sccm, 200W, 0% O ₂	32 [46]
		SF ₆ /O ₂		410
		CF ₄ /O ₂		278
		NF ₃ /O ₂		483
ECR	3C	SF ₆	150 W, 80 mTorr	700 [51]
	6H, 4H	NF ₃	225 mTorr, 95-110 sccm, 275W	1500 [45]
ICP	6H	CF ₄ /O ₂	500W, -100V, 17.5% O ₂ , 50 sccm	800 [52]
		CF ₄ /O ₂	650W, -100V, 17% O ₂ , 50 sccm	700 [53]
		20SF ₆ /10Ar	750W, 250 rf, 2 mTorr, 30 sccm	4500 [54]
		SF ₆ /O ₂	1200W, 1 mTorr, 4 sccm	2500 [55]
		10Cl ₂ /5Ar	1000W, 150 rf, 1.5 mTorr, 15 sccm	2500 [47]
	6H	10Cl ₂ /5H ₂	1000W, 150 rf, 1.5 mTorr, 15 sccm	1000
		4IBr/4Ar	1000W, 250 rf, 1.5 mTorr, 15 sccm	1100
		NF ₃	800W, 100 rf, 1 mTorr, 10 sccm	1600
		SF ₆	800W, 100 rf, 1 mTorr, 10 sccm	450
		Cl ₂ /Ar or He	100 Cl ₂ , 750W, 250 rf, 5 mTorr	100 [54]
	6H	Cl ₂ /Xe	13% Cl ₂ , 750W, 250 rf, 5 mTorr	260
		IBr/Ar	10% Cl ₂ , 750W, 250 rf, 5 mTorr	800
		ICl/Ar	66% Cl ₂ , 750W, 250 rf, 5 mTorr	250
		NF ₃ /O ₂ or Ar	100% NF ₃ , 750W, 250 rf, 5 mTorr	4000 [56]

3.4 SiC for MEMS Applications

Silicon carbide (SiC) is a promising material for the development of high-temperature solid-state electronics and transducers, [57] owing to its excellent electrical, mechanical, and chemical properties. Many measurement and control applications that require micro-sensor and micro-actuator technologies are in the presence of chemically

reactive and high temperatures environments. For example, the comprehensive instrumentation needed to maximize the efficiency of gas turbine, rocket, and internal combustion engines must be able to reliably monitor operating parameters in and around combustion environments. This need includes the measurement of steady state and transient phenomena (e.g., temperature, pressure, acceleration, and flow parameters), as well as monitoring of the by-products of the combustion process.^[58] The wide bandgap SiC is well suited for such sensing applications in harsh environments.

SiC's high temperature capabilities, for example, have enabled the realization of catalytic metal-SiC and metal-insulator-SiC (MIS) prototype gas sensor structures with great promise for emissions monitoring applications.^{[59], [60]} These structures with catalytically active gates are widely used to electronically detect the presences of various chemical species.^{[60], [61]} A number of groups have demonstrated the refractory metal gate SiC devices for high temperature chemical sensing applications,^{[57], [58], [62], [63], [64], [65], [66]} which include hydrogen and hydrocarbon sensors operating at temperatures from 600 K to 1300K. Specific sensor configurations have achieved millisecond time response and sensitivity at the 0.1% level. In addition, the preliminary results indicate that suitably designed devices may offer sensitivity to ammonia, carbon monoxide, nitrogen oxides and fluorocarbons.^[67]

Although Si is well suited for a wide range of sensor and actuator applications, it is generally limited in electronic device operating below 250 °C and in mechanical device functioning below 600 °C (due to a decline in its elastic modulus with increasing

temperature). If not impractical, the bulky packaging required to keep Si-based micro-electro-mechanical systems (MEMS) within operating limits (in practice, below 250 °C) in high-temperature environments is both space and cost intensive for many applications. Consequently, for high-temperature MEMS applications (e.g., above 350 °C^[68]), there is a need for semiconductors with good mechanical and thermal stability and a wide bandgap for stable electronic properties at elevated temperatures. Silicon carbide (SiC) has these properties, as well as additional attractive features. Compared to Si, SiC demonstrates higher chemical inertness and radiation resistance, which expands its potential to MEMS for space satellite systems. At the same time, single and polycrystalline SiC can be grown on large area substrates and are compatible with batch-fabrication processes used in Si micromachining and integrated circuit (IC) industries. To a large extent, SiC device fabrication technology leverages off the infrastructure of Si technology.

The need for instrumentation in harsh environments, in particular at temperatures above 350 °C, has spurred the research and development of SiC MEMS, resulting in rapid advances in the technology over the last several years. Due to the ease of deposition and the ability to deposit poly-SiC on many different substrates, some of the first SiC-based sensors were fabricated from poly-SiC. In 1990, the fabrication of a poly-SiC thin-film thermistor on an alumina substrate was reported.^[69] The sensor was fabricated from RF-sputter-deposited SiC, using sintered SiC as a target, Ar as a sputtering gas, and a deposition pressure of 20 mTorr. Various packages for the thermistor were developed, and the device was tested at temperatures from 0 to 500 °C. The authors observed a

resistance change of only 5% after a continuous test at 500 °C for 1000 h. A second group reported the fabrication of SiC-based resistive temperature sensors on Si substrates [70]. SiC films for this sensor were prepared by plasma-assisted CVD, using dichlorosilane and methane as Si and C source gases. The resistors were tested at temperatures between 0 and 300 °C and exhibited a temperature coefficient of resistance of 1800 ppm/°C. The sensor was placed into a nitrogen flow stream to evaluate its performance as a gas mass flow sensor. The output characteristics of the SiC sensor showed square root dependence, and the output sensitivity was 0.05 mV/sccm.

The more reports on SiC-based gas sensors, pressure sensors, lateral resonant devices, and atomizers that show the ability to operate in harsh environment can be found in the references. [71], [72], [73], [74], [75], [76], [77], [78], [79], [80], [81], [82], [83], [84] However, most of them were electrically active. For certain applications, in order to have stable and reliable electrical properties at high temperature, a good formation of electrical contact for SiC devices is highly desirable and requires a well-developed processing technology, which still needs further effort to improve. [85] To solve this problem, the combination of fiber-optic technology and SiC technology opens a way to show an alternative (electrically passive SiC devices) to electrical devices at high temperature. Based on the following brief introduction about thin-film Fabry-Perot interferometer for fiber-optic temperature sensors, we have investigated the SiC thin-film Fabry-Perot interferometers operating at high temperature (540 °C). The details will be discussed in Chapter 6.

3.5 Thin-film Fabry-Perot interferometer for fiber-optic temperature sensor

The benefits of fiber optics are fully realized when the remotely located sensor is linked solely by fibers. Fiber-linked optical temperature sensors can be categorized on the basis of their method of signal generation as follows:

- (a) Optically emissive, thermally powered; [86]
- (b) Optically emissive, optically powered; [87], [88]
- (c) Intensity modulating (non-emissive). [89], [90]

In this study we have looked at a thin-film Fabry-Perot temperature sensor that falls under the category of intensity modulating (non-emissive). Therefore, the following discussion will be on non-emissive Fabry-Perot type temperature sensors only. A fiber-linked Fabry-Perot interferometer can provide a wavelength-encoded temperature measurement from a very compact and rugged sensor. Typically, the Fabry-Perot temperature sensor is a thin platelet of a material that has a temperature-dependent refractive index. [89], [90]

3.5.1 Fabry-Perot interferometer for temperature sensor

A Fabry-Perot interferometer is one type of spectrum-modulating transducer that can be used to sense a number of different physical parameters. [91] The separation between the thin film boundaries, L, is of the order of magnitude of the wavelength so

that interference effects occur.^[92] During the operation, it must incorporate some mechanism, which causes the interferometer's optical path difference (OPD) to be a stable and sensitive function of only the parameter to be measured. For the phase-modulated sensors, if the sensor is illuminated by a broadband light source, the positions of the maxima and minima of the sensor's output spectrum can be used to determine the magnitude of the sensed parameter. The information content of this type of spectrally encoded signal is unlikely to be degraded by routine variations in the transmission properties of the fiber link. Besides providing a high degree of link-independence, Fabry-Perot type sensors can be compact and rugged, and they can provide both high sensitivity and stability.^[93]

3.5.2 Wavelength-encoded temperature measurement

A wavelength-encoded temperature measurement can be provided by a temperature-sensitive Fabry-Perot interferometer. As shown in Fig. 3-7, the essential feature of it is two parallel flat reflective surfaces, which are separated by a distance L , where n_0 , n_1 and n_2 represent refractive index of ambient, refractive index of thin-film interferometer and refractive index of substrate, respectively. If the interferometer is operated in reflection mode, only the first

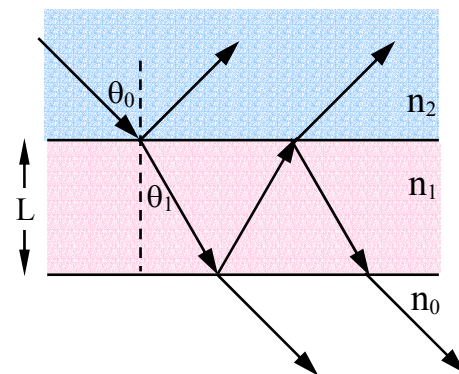


Figure 3-7. A schematic of Fabry-Perot interferometer.

reflector needs to be partially transmissive. The light is assumed to be collimated, with an internal angle of incidence θ_1 . The Fabry-Perot interferometer's OPD is then given by

$\Lambda_{OPD} = 2n_1 L \cos \theta_1$. To sense temperature, Λ_{OPD} must vary as a monotonic function of temperature. This can be affected by changes in n_1 or L .

At resonance, $\lambda = \lambda_m$, where the resonant wavelength of integer-order m is given by $m\lambda_m = \Lambda_{OPD}$, the interferometer's spectral reflectance $R_F(\lambda)$ is minimized (here it is assumed that the phase changes on internal reflection are zero). The sensed temperature can be determined by tracking the position of one of the minima in $R_F(\lambda)$, since λ_m is proportional to the temperature-dependent Λ_{OPD} . This wavelength-based measurement method, because it is signal-level insensitive, has a high degree of immunity to the effects of changes in the transmissivities of the optical fibers and connectors. A more detailed description about the operation of a wavelength encoded Fabry-Perot interferometer as well as an estimate of the sensor's temperature sensitivity will be addressed in Chapter 6.

3.6 References:

-
- [¹] J. T. Drotar, Y.-P. Zhao, T.-M. Lu, and G.-C. Wang, “Surface roughening in low-pressure chemical vapor deposition”, *Physical Review B*, Vol. **64**, p. 125411, Sept. 2001.
 - [²] Y.-P. Zhao, J. T. Drotar, G.-C. Wang, and T.-M. Lu, “Morphology Transition during Low-Pressure Chemical Vapor Deposition”, *Phys. Rev. Lett.*, Vol. **87**, No. 13, p. 136102, Sept. 2001.
 - [³] C. H. J. Van den Brekel and A. K. Jansen, *J. Cryst. Growth*, Vol. **43**, p. 364 & p. 371, 1978.
 - [⁴] B. J. Palmer and R. G. Gordon, *Thin Solid Films* **158**, p. 313 (1988); Vol. **177**, p. 141, 1989.
 - [⁵] G. S. Bales, A. C. Redfield, and A. Zangwill, “Growth Dynamics of Chemical vapor deposition”, *Phys. Rev. Lett.* Vol. **62**, No. 7, pp. 776-779, Feb. 1989.
 - [⁶] R. Ananth and W. N. Gill, *J. Cryst. Growth*, Vol. **118**, p. 60, 1992.
 - [⁷] H. J. Viljoen, J. J. Thiart, and V. Hlavacek, *AIChE J.*, Vol. **40**, p. 1032, 1994.
 - [⁸] M. Ikegawa and J. Kobayashi, *J. Electrochem. Soc.*, Vol. **136**, p. 2982, 1989.
 - [⁹] M. Kardar, G. Parisi, and Y-C. Zhang, “Dynamic Scaling of Growing Interfaces”, *Phys. Rev. Lett.*, Vol. **56**, No. 9, pp. 889-892, March 1986.
 - [¹⁰] M. J. Cooke and G. Harris, *J. Vac. Sci. Technol. A* **7**, p. 3217, 1989.
 - [¹¹] T. S. Cale and G. B. Raupp, *J. Vac. Sci. Technol. B*, Vol. **8**, p. 649 & p. 1242, 1990.
 - [¹²] J. J. Hsieh, *J. Vac. Sci. Technol., A* **11**, p. 78, 1993.
 - [¹³] V. K. Singh and S. G. Shaqfeh, *J. Vac. Sci. Technol. A* **11**, p. 557, 1993.
 - [¹⁴] D. G. Coronell and K. F. Jensen, *J. Electrochem. Soc.*, Vol. **141**, p. 2545, 1994.
 - [¹⁵] S. T. Rodgers and K. F. Jensen, *J. Appl. Phys.*, Vol. **83**, p. 524, 1998.

-
- [¹⁶] T. S. Cale and V. Mahadev, in *Modeling of Film Deposition for Microelectronic Applications*, edited by S. Rossnagel and A. Ulman, Academic, San Diego, 1996
- [¹⁷] Y.-P. Zhao, Jason T. Drotar, G.-C. Wang, and T.-M. Lu, Phys. Rev. Lett. (to be published)
- [¹⁸] K. Kurosawa, “VI-M Thin Film Preparation with Chemical Vapor Deposition Using Vacuum Ultraviolet Radiation”, *Annual Review, RESEARCH ACTIVITIES VI*, Department of Vacuum UV Photoscience, Institute for Molecular Science, Japan, pp.147-148, 2001. See also http://www.ims.ac.jp/publications/ann_rev_2001/ar200165.pdf.
- [¹⁹] C. H. Wu, C. A. Zorman, and M. Mehregany, in *Materials Science Forum*, Vols. 339-342, pp. 541-544, 2000.
- [²⁰] A. J. Fleischman, X. Wei, C. A. Zorman, and M. Mehregany, in *Proceedings of the 7th International Conference on Silicon Carbide, III-Nitrides and Related materials*, Stockholm, Sweden, Materials Science Forum, Vols. **264-268**, p. 885, 1998.
- [²¹] H. Nakamatsu, K. Hirata, and S. Kaeai, *Mater. Res. Soc. Symp.*, **101**, p. 397 (1988)
- [²²] L. Rimai, R. Ager, J. Hangas, E. M. Logothetis, N. Abu-Ageel, and M. Aslam, *J. Appl. Phys.*, Vol. **73**, p. 8242, 1993.
- [²³] J. C. Pazik, G. Kelner, and N. Bottka, *Appl. Phys. Lett.*, Vol. **58**, p. 1419, 1992.
- [²⁴] B. S. Sywe, Z. J. Yu, S. Burchard, J. H. Edgar, and J. Chaudhuri, *J. Electrochem. Soc.*, Vol. **141**, L66, 1994.
- [²⁵] X. tang, K. Wongchotigul, and M. G. Spencer, *Appl. Phys. Lett.*, Vol. **58**, p. 917, 1991.
- [²⁶] A. J. Steckl, C. Yuan, Q. Y. Tong, U. Gosele, and M. J. Loboda, *J. Electrochem. Soc.*, Vol. **141**, L66, 1994.

-
- [²⁷] Q. Y. Tong, U. Gosele, C. Yuan, A. J. Steckl, and M. Reiche, *J. Electrochem. Soc.*, Vol. **142**, p. 232, 1995.
- [²⁸] C. A. Zorman, K. N. Vinod, A. Yasseen, and M. Mehregany, in *Proceedings of the 7th International Conference in Silicon Carbide, III-Nitrides and Related Materials*, Stockholm, Sweden, Materials Science Forum, Vols. 264-268, p. 223, 1998.
- [²⁹] L. Di Cioccio, Y. Le Tiec, F. Letertre, C. Jaussaud, and M. Bruel, *Electron. Lett.*, Vol. **32**, p. 1144, 1996.
- [³⁰] L. Di Cioccio, F. Letertre, Y. Le Tiec, A. Papon, C. Jaussaud, and M. Bruel, *Mater. Sci. Eng.*, B**46**, p. 347, 1997.
- [³¹] C. H. Wu, C. A. Zorman, and M. Mehregany, *Thin Solid Films*, Vols. **355-356**, p. 179, 1999.
- [³²] J. Rodriguez-Vieho, J. Stoemenos, N. Clavaguera, and M. T. Clavaguera-Mora, *J. Cryst. Growth*, Vol. **155**, p. 214, 1995.
- [³³] K. C. Kim, C. Park, K. S. Nahm, E. K. Suh, in *Proceedings of the 8th International Conference on Silicon Carbide, Related Materials*, Materials Science Forum, Vols. 338-342, p. 317, 2000.
- [³⁴] Spearing, S. M., Materials issue in Microelectromechanical Systems (MEMS), *Acta Materialia*, Vol. **48**, pp 179-196, 2000.
- [³⁵] L. Zhou, V. Audurier, and P. Pirouz, “Chemomechanical Polishing of Silicon Carbide”, *J. Electrochem. Soc.* Vol. **144**, No. 6, June 1997.
- [³⁶] J. A. Bittencourt, *Fundamentals of Plasma Physics*, Pergamon Press, 1986.
- [³⁷] T. Sugano, *Applications of Plasma Processes to VLSI Technology*, John Wiley and Sons Publishers, 1985.

-
- [³⁸] D. M. Manos, and D. L. Flamm, *Plasma etching: An Introduction*, Academic Press, Boston, 1989.
- [³⁹] J. J. Wang, E. S. Lambers, S. J. Pearton, M. Ostling, C.-M. Zetterling, J. M. Grow, F. Ren, and R. J. Shu, “ICP Etching of SiC”, *Solid-State Electronics*, Vol. 42 No. 12, pp. 2283-2288, 1998.
- [⁴⁰] T. M. Christensen, “Plasma Physics”, *Class notes of Physics of Thin Film (PHYS549)*, Dept. of Physics and Energy Science, University of Colorado at Colorado Springs, 2002.
- [⁴¹] S. M. Rossnagel, J. J. Cuomo, and W. D. Westwood, “HANDBOOK OF PLASMA PROCESSING TECHNOLOGY”, *Materials Science and Process Technology Series*, Series eds.: R. F. Bunshah, and G. E. McGuire, Noyes Pub., NJ, 1989.
- [⁴²] S. K. Ghandhi, *VLSI Fabrication Principles*, John Wiley & Sons, Inc., New York, 1994.
- [⁴³] L. Jiang, R. Cheung, R. Brown, and A. Mount, “Inductively coupled plasma etching of SiC in SF₆ /O₂ and etch-induced surface chemical bonding modifications”, *J. of Appl. Phys.*, Vol. 93, No. 3, pp. 1376-1383, Feb. 2003.
- [⁴⁴] J. J. Wang, E. S. Lambers, S. J. Pearton, M. Ostling, C. -M. Zetterling, J. M. Grow, and F. Ren, *Mat. Res. Soc. Symp. Proc.*, **483**, p. 177, 1997.
- [⁴⁵] J. B. Casady, E. D. Luckowski, M. Bozsck, D. Sheridan, R. W. Johnson and J. R. Williams, *J. Electrochem. Soc.*, Vol. **143**, pp. 1750, 1996.
- [⁴⁶] P. H. Yih, and A. J. Steckl, *J. Electrochem. Soc.*, **142**, p. 312, 1996.
- [⁴⁷] G. F. McDaniel, J. W. Lee, E. S. Lambers, S. J. Pearton, P. H. Holloway, F. Ren, J. M. Grow, M. Bhaskaran, and R. G. Wilson, “Comparison of dry etch chemistries for SiC”, *J. Vac. Sci. Technol.*, **A14**, p. 885, 1997.

-
- [⁴⁸] P. H. Yih, and A. J. Steckl, *J. Electrochem. Soc.*, **140**, p. 1813, 1993.
- [⁴⁹] A. J. Steckl, and P. H. Yih, *Appl. Phys. Lett.*, **60**, p. 1966, 1992.
- [⁵⁰] J. R. Flemish, “Dry Etching of SiC”, In *Proc. Wide Bandgap Semic.*, ed. by S. J. Pearton, William Andrew Publ., Park Ridge, NJ, 1999
- [⁵¹] J. Wu, J. D. Parsons, and D. R. Evans, *J. Electrochem. Soc.*, **142**, p. 669, 1995.
- [⁵²] J. R. Flemish, K. Xie, and J. Zhao, *Appl. Phys. Lett.*, **64**, p. 2315, 1994.
- [⁵³] J. R. Flemish, and K. Xie, *J. Electrochem. Soc.*, **143**, p. 2620, 1996.
- [⁵⁴] J. Hong, R. J. Shul, L. Zhang, L. F. Lester, H. Cho, Y. B. Hahn, D. C. Hays, K. B. Jung, S. J. Pearton, C. -M. Zetterling, and M. Ostling, *J. Electron. Mater.* **28**, p. 196, 1999.
- [⁵⁵] F. Lanois, P. Lassagne, D. Planson, and M. L. Locatelli, *Appl. Phys. Lett.*, **69**, p. 236, 1996
- [⁵⁶] J. J. Wang, E. S. Lambers, S. J. Pearton, M. Ostling, C. -M. Zetterling, J. M. Grow, F. Ren, and R. J. Shul, *J. Vac. Sci. Technol.*, **A16**, p. 2204, 1998.
- [⁵⁷] V. I. Filippov, A. A. Vasilev, A. A. Terentev, W. Moritz and U. Roth, “Sensor Based on a Pt/LaF₃/SiO₂/SiC Structure for the Detection of Chlorofluorocarbons”, *Tech. Phys.* **44**, pp. 1334-1339, 1999.
- [⁵⁸] A. Lloyd Spetz, L. Unéus, H. Svenssonstorp, P. Tobias, L. G. Ekedahl, O. Larsson, A. Göras, S. Savage, C. Harris, P. Mårtensson, R. Wigren, P. Salomonsson, B. Häggendahl, P. Ljung, M. Mattsson, and I. Lundström, “SiC Based Field Effect Gas Sensors for Industrial Applications”, *Phys. Stat. Solidi A*, **185**, pp. 15-25, 2001.
- [⁵⁹] Hunter, G. W., Neudeck, P. G., Chen, L. Y., Knight, D., Liu, C. C. and Wu, Q. H., “SiC-Based Schottky Diode Gas Sensors”, *Silicon Carbide, III-Nitrides, and Related*

Materials, Materials Science Forum, 264-268, Pensl, G., Morkoc, H., Monemar, B. and Janzen, E., Eds., Trans Tech Publications, Switzerland, p. 1093, 1998.

[⁶⁰] A. Lloyd Spetz, A. Baranzahi, P. Tobias, and I. Lundstrom, “High Temperature Sensors Based on Metal-Insulator-Silicon Carbide Devices”, *Physica Status Solidi A*, **162**, pp. 493-511, 1997.

[⁶¹] I. Lundström, A. Berg, B. H. Schoot, H. H. Vlekkert, M. Armgarth and C. I. Nylander, “Field Effect Chemical Sensors”, in W. Gopel, J. Hesse, J. N. Zemel, Ed., *Sensors vol. 2*, VCH, Cambridge, New York, pp. 467-528, 1991.

[⁶²] G. W. Hunter, P. G. Neudeck, M. Gray, D. Androjna, L.-Y. Chien, R. W. Hoffman, Jr., C. C. Liu, and Q. H. Wu, “SiC-based Gas Sensor Development”, *Mater. Sci. Forum*, **338-342**, pp. 1439-1422, 2000.

[⁶³] C. K. Kim, J. H. Lee, S. M. Choi, I. H. Noh, H. R. Kim, N. I. Cho, C. Hong, and G. E. Jang, “Pd and Pt SiC Schottky Diodes for Detection of H₂ and CH₄ at High Temperature”, *Sensor. Actuat. B-Chem.* **77**, pp. 455-462, 2001.

[⁶⁴] S. Nakagomi, Y. Shindo, and Y. Kokubun, “Stability of electrical properties of high-temperature operated H₂ sensor based on Pt-I-SiC diode” *Phys. Stat. Solidi A*, **185**, pp. 33-38, 2001.

[⁶⁵] A. Samman, S. Gebremariam S, L. Rimali L, X. Zhang, J. Hangas, and G. W. Auner, “Silicon-carbide MOS Capacitors with Laser-ablated Pt Gate as Combustible Gas Sensors”, *Sensor. Actuat. B-Chem.* **63**, pp. 91-102, 2000.

[⁶⁶] F. Serina, K. Y. S. Ng, C. Huang, G. W. Auner, L. Rimali, and R. Naik, “Pd/AlN/SiC Thin-film Devices for Selective Hydrogen Sensing”, *Appl. Phys. Lett.*, **79**, pp. 3350-3352, 2001.

-
- [⁶⁷] R. N. Ghosh, P. Tobias, S. G. Ejakow, and B. Golding, “Interface States in High Temperature SiC Gas Sensing”, *Proc. of IEEE Sensors*, **2**, pp.1120-1125, 2002.
- [⁶⁸] M. Mehregany, C. A. Zorman, N. Rajan, and C. H. Wu, *Proc. of the IEEE*, Vol. **86**, No. 8, pp. 1594 – 1610, Aug. 1998.
- [⁶⁹] T. Nagai and M. Itoh, “SiC thin-film thermistors,” *IEEE Trans. Ind. Applicat.*, vol. 26, pp. 1139–1143, 1990.
- [⁷⁰] K. Kamimura, T. Miwa, T. Sugiyama, T. Ogawa, N. Nakao, and Y. Onuma, “Preparation of polycrystalline SiC thin films and its application to resistive sensors,” in *Silicon Carbide and Related Materials*, vol. 142, S. Nakashima, H. Matsunami, S. Yoshida, and H. Harima, Eds. Bristol, UK: IOP Publishing, pp. 825–828, 1996.
- [⁷¹] A. Arbab, A. Spetz, and I. Lundstrom, “Gas sensors for high temperature operation based on metal oxide silicon carbide (MOSiC) devices,” *Sensors Actuators B*, Vol. **15–16**, pp. 19–23, 1993.
- [⁷²] “Evaluation of gas mixtures with high-temperature gas sensors based on silicon carbide,” *Sensors Actuators B*, Vol. **18–19**, pp. 562–565, 1994.
- [⁷³] A. Baranzahi, A. L. Spetz, B. Andersson, and I. Lundstrom, “Gas sensitive field effect devices for high temperatures,” *Sensors Actuators B*, Vol. **26–27**, pp. 165–169, 1995.
- [⁷⁴] G. Hunter, P. Neudeck, D. Knight, C. C. Liu, and Q. H. Wu, “Silicon carbide-based detection of hydrogen and hydrocarbons,” in *Silicon Carbide and Related Materials*, Vol. **142**, S. Nakashima, H. Matsunami, S. Yoshida and H. Harima, Eds. Bristol, UK: IOP Publishing, pp. 817–820, 1996.
- [⁷⁵] V. B. Shields, M. A. Ryan, R. M. Williams, M. G. Spencer, D. M. Collins, and D. Zhang, “A variable potential porous silicon carbide hydrocarbon gas sensor,” in *Silicon*

Carbide and Related Materials, Vol. **142**, S. Nakashima, H. Matsunami, S. Yoshida, and H. Harima, Eds. Bristol, UK: IOP Publishing, pp. 1067–1070, 1996.

[⁷⁶] R. Okojie, A. Ned, and A. Kurtz, “Operation of 6H-SiC pressure sensor at 500 °C,” in *Tech. Dig. 1997 Int. Conf. Solid State Sensors and Actuators*, K. Wise and S. Senturia, Eds., Chicago IL, pp. 1407–1409, June 16–19, 1997.

[⁷⁷] R. Zeirmann, J. von Berg, W. Reichert, E. Obermeier, M. Eickhoff, and G. Krotz, “A high temperature pressure sensor with β-SiC piezoresistors on SOI substrates,” in *Tech. Dig. 1997 Int. Conf. Solid State Sensors and Actuators*, K. Wise and S. Senturia, Eds., Chicago IL, pp. 1411–1414, June 16–19, 1997.

[⁷⁸] G. Krotz, “New harsh environment sensor designs based on silicon carbide,” *MST News*, Vol. **21**, p. 17, Sept. 1997.

[⁷⁹] A. Garcia-Alonso, E. Castano, I. Obieta, and J. Garcia, “Thin film technology applied to the development of a multilayer pressure sensor device,” *Vacuum*, Vol. **45**, pp. 1103–1105, 1994.

[⁸⁰] V. Mosser, J. Suski, and J. Goss, “Piezoresistive pressure sensors based on polycrystalline silicon,” *Sensors Actuators A*, Vol. **28**, pp. 113–132, 1991.

[⁸¹] A. J. Fleischman, S. Roy, C. A. Zorman, and M. Mehregany, “Polycrystalline silicon carbide for surface micromachining,” in *Proc. 9th Ann. Int. Workshop Microelectromechanical Systems*, M. Allen and M. Reed, Eds., San Diego, CA, pp. 234–238, Feb. 11–15, 1996.

[⁸²] A. J. Fleischman, S. Roy, C. A. Zorman, and M. Mehregany, “Behavior of polycrystalline SiC and Si surface-micromachined lateral resonant structures at elevated

temperatures,” in *Extended Abstracts Int. Conf. Silicon Carbide, III—Nitrides, and Related Materials—1997*, Stockholm, Sweden, pp. 643–644, Aug. 31–Sept. 5, 1997.

[⁸³] A. Singh, M. Mehregany, S. Phillips, R. Harvey, M. Benjamin, “Micromachined silicon fuel atomizers for gas turbine engines,” in *Proc. 9th Ann. Int. Workshop Microelectromechanical Systems*, M. Allen and M. Reed, Eds., San Diego, CA, Feb. 11–15, pp. 473–478, 1996.

[⁸⁴] N. Rajan, C. A. Zorman, M. Mehregany, R. DeAnna, and R. Harvey, “3C-SiC coating of silicon micromachined atomizers,” in *Proc. 10th Ann. Int. Workshop Microelectromechanical Systems*, S. Kazuo and S. Shoji, Eds., Nagoya, Japan, pp. 165–168, Jan. 26–30, 1997.

[⁸⁵] L. Cheng, A. J. Steckl, and J. D. Scofield, “Polycrystalline SiC thin-film as a Fabry-Perot Interferometer for Fiber-Optic Temperature Sensor” submitted, Feb. 2003.

[⁸⁶] R.R. Dils, High Teperature Fiber Thermometry , *J. Appl. Phys.* **54**, p. 1198, 1983.

[⁸⁷] A. Ohte, K. Akiyama, and I. Ohno, “Optically-Powered Transducer with Optical Fiber Data Link”, *Fiber Optic and Laser Sensors II*, E.L. Moore and O.G. Ramer, eds., *Proc. SPIE* 478, pp. 33-38, 1985.

[⁸⁸] K.T.M. Gratten, A.W. Palmer, C.A. Wilson, “A Miniaturized Microcomputer-based Neodymium Decay-Time Temperature Sensor”, *J. Phys. E: Sci. Instrum.*, Vol. **20**, p. 1201, 1985.

[⁸⁹] G. Beheim, “Fiber-Optic Thermometer Using semiconductor-etalon sensor”, *Electron. Lett.*, Vol. **22**, pp. 238-239, 1985.

-
- [⁹⁰] J.C. Hartl, E. W. Saaski, and G. L. Mitchell, “Fiber Optic Temperature Sensor Using Spectral Modulation”, *Fiber Optic and Laser Sensors V*, R. P. DePaula and E. Udd, eds., *Proc. SPIE* 838, pp. 257-261, 1987.
- [⁹¹] Henry F. Taylor, “Fiber optic sensors based upon the Fabry-Perot interferometer,” in *Fiber Optic Sensors*, eds.: Francis T. S. Yu, and Shizhou Yin, Marcel Dekker, Inc., pp. 41-71, 2002.
- [⁹²] Milton Ohring, ed., “The Materials Science of Thin Films,” Academic Press, Inc., pp.526-5230, 1992.
- [⁹³] G. Beheim, K. Fritsch, and Donald J. Anthan, “Fiber-optic temperature sensor using a spectrum-modulating semiconductor etalon”, NASA Technical Memorandum 100153, 1987.

CHAPTER 4. GROWTH AND DOPING OF SiC THIN-FILM ON LOW-STRESS, AMORPHOUS Si₃N₄/Si SUBSTRATE

4.1 Low-stress, amorphous Si₃N₄ grown on Si substrate by LPCVD

The use of ‘low stress’ silicon nitride is prevalent in many micro-fabrication applications.^[1] This film is known to have desirable physical characteristics for structural components in MEMS devices, as well as being used as a hard mask for wet and dry etching. A Low Pressure Chemical Vapor Deposition (LPCVD) process is commonly used to deposit thin layers of silicon nitride. LPCVD depositions have proven to produce a high integrity, repeatable, controllable, and uniform film ideal for many micro-fabrication applications.

The MEMS applications require that large-area, uniform SiC films are formed on insulating or sacrificial layers,^{[2], [3]} such as SiO₂, Si₃N₄, and polycrystalline Si (poly-Si). As an insulating barrier layer for SiC MEMS applications, Si₃N₄ is more attractive than SiO₂ due to its higher dielectric constant that can reduce the leakage currents and the dopant (such as boron) penetration.^[4] Another drawback of SiO₂ for SiCOI structures is the decomposition of SiO₂ at temperature above 1100°C during SiC growth, which may cause the oxygen contamination that can affect the electrical properties of SiC films.^[5] In addition, because the thermal expansion coefficient of Si₃N₄ is much closer to that of SiC than one of SiO₂, the stress existed in SiC thin-film grown on Si₃N₄ will be lower than

that on SiO₂. Hence, Si₃N₄ is more suitable than SiO₂ as a functional layer for SiC-MEMS devices. Table 4-1 shows some basic properties of Si₃N₄ and SiO₂.

In this study, we use low stress, amorphous Si₃N₄ (0.5 μm) grown on <100> double-side polished 4" Si substrate by LPCVD from Cronos Integrated Microsystems, Inc. in NC. The Si substrate is 400 μm thick. The color of nitride film is bluish green; the refractive index of nitride film is between 2.15 to 2.30; the stress in the film is tensile and less than 140 MPa.

4.2 Growth of SiC thin-film by LPCVD

4.2.1 Introduction of RM rapid thermal CVD system

Conventional thermal processing (e.g. CVD, furnace oxidation, furnace annealing) involves the use of high temperatures with reaction times in minutes and hours. These high temperatures are necessary since the quality of deposition, growth rate and activation of implanted species are, in general, superior at higher temperatures. However, continuous exposures at high temperatures for extended periods of time have also been found to be detrimental on occasion since diffusion of dopants may be more than desired. Inter-diffusion of impurities from the substrate to the deposited film is also possible. In addition, maintaining the high temperatures may result in damage to both the substrate and the film. These drawbacks lead to the need to minimize the time for which

the materials ‘see’ high temperatures. The rapid thermal processing (RTP) technique has been designed with this objective in mind.

Table 4-1 Properties of SiO_2 and Si_3N_4 at 300 K ^[6]

Properties	SiO_2	Si_3N_4
Structure	Amorphous	Amorphous
Melting point (°C)	~1600	—
Density (g/cm ³)	2.2	3.1
Refractive index	1.46	2.05
Dielectric constant	3.9	7.5
Dielectric strength (V/cm)	10^7	10^7
Infrared absorption band (μm)	9.3	11.5-12.0
Energy gap (eV)	9	~5.0
Thermal-expansion coefficient (°C ⁻¹)	5×10^{-7}	4×10^{-6} ^[7]
Thermal conductivity (W/cm-K)	0.014	0.019 ^[8] - 0.037 ^[9]
DC resistivity ($\Omega\text{-cm}$) at 25 °C at 500 °C	10^{14} - 10^{16} —	$\sim 10^{14}$ $\sim 2 \times 10^{13}$
Etch rate in buffered HF ^a (Å/min)	1000	5-10

^a Buffered HF: 34.6% (wt.) NH_4F , 6.8% (wt.) HF, 58.6% H_2O .

In the RTP technique, the temperature of the wafer can be ramped up to high temperatures in a matter of seconds. Since the total thermal budget (heat supplied \times time) is reduced dramatically, the problems of inter-diffusion or damage to the material are also decreased. The wafer is normally placed on a quartz tray with the only contact between the two being via tiny pins on which the wafer rests. Lamps that supply infrared energy are placed on either side of the wafer. The power supplied to the lamps can be changed extremely rapidly and so the energy supplied by it and absorbed by the wafer is also changed extremely quickly. This enables ramping up the temperature of the wafer at rates up to 250 °C/sec. Since the wafer absorbs far more of this energy than the surrounding environment, the wafer is at much higher temperature. Upon switching off power to the lamps, the wafer can radiate its heat very quickly resulting in rapid ramp downs. The temperature uniformity across the wafer can be controlled accurately by controlling the power to the lamps close to different regions of the wafer. Usually, there are no thermal stresses across the wafer except at the wafer edge. The RTP technique is now widely used in ion implantation annealing, metal silicidation, thin dielectric formation, etc.

The rapid thermal CVD system used in this study is modified from AET Addax Inc.^[10]. The system comprises three main parts: the reaction chamber, the pumping group and the gas distribution system, as shown in Fig. 4-1. The reaction chamber (Fig. 4-2) is fabricated from high quality quartz. It has a rectangular cross-section that enables both vacuum operation and large area deposition (up to 4" diameter substrate) while efficiently utilizing the infrared output of lamps placed on both sides of the chamber. The Si substrate is placed on six quartz pins of a quartz tray that is attached to a water-cooled door. The

problem of carbon contamination due to the graphite susceptor commonly used in the conventional CVD growth is thus eliminated. Two rows of nine high-power (6000 W/each) tungsten halogen lamps are used to heat the wafer. The lamps are enclosed within a stainless steel chamber that has a reflective coating of gold to the inner wall and is water-cooled. The wafer temperature is monitored using an optical pyrometer or a thermocouple.

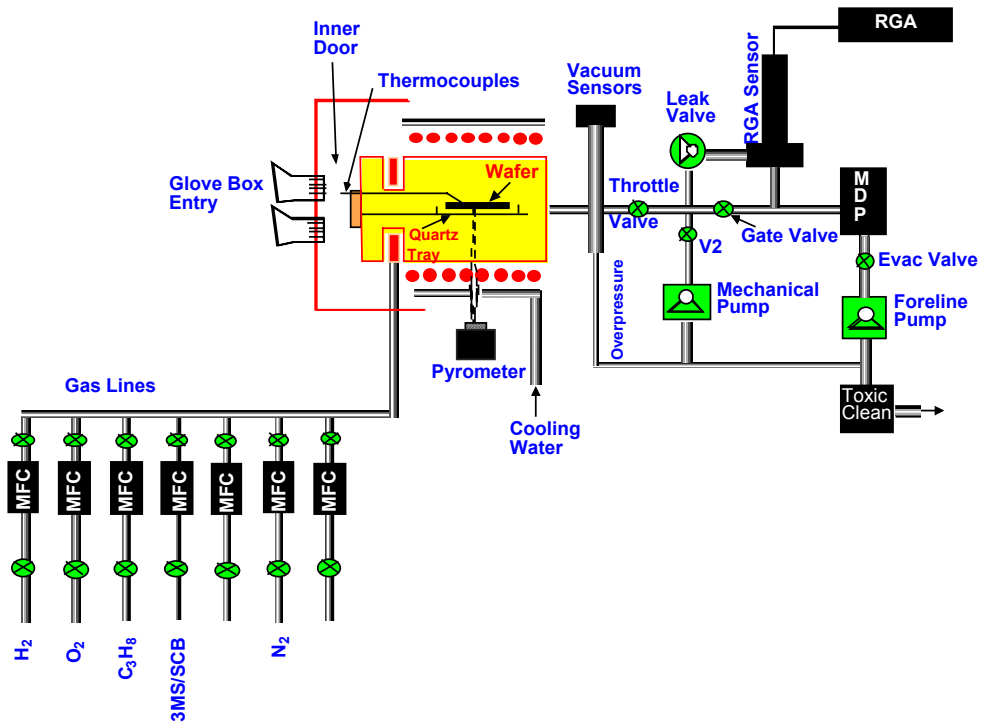


Figure 4-1. Schematic diagram of the rapid thermal RTCVD system

The system is capable of pumping down the chamber to a base pressure of 10^{-3} torr using a mechanical pump (Alcatek 2020 CP1). A thermocouple vacuum gauge and a cold-cathode vacuum gauge are used to indicate the chamber pressure. A toxic gas cleaning system is installed at the outlet of the mechanical pump to filter out any toxic residual precursors and by-products. Seven process gas lines are equipped with electronic

mass flow controllers. The gases are introduced into the chamber through nozzles on the front door flange.

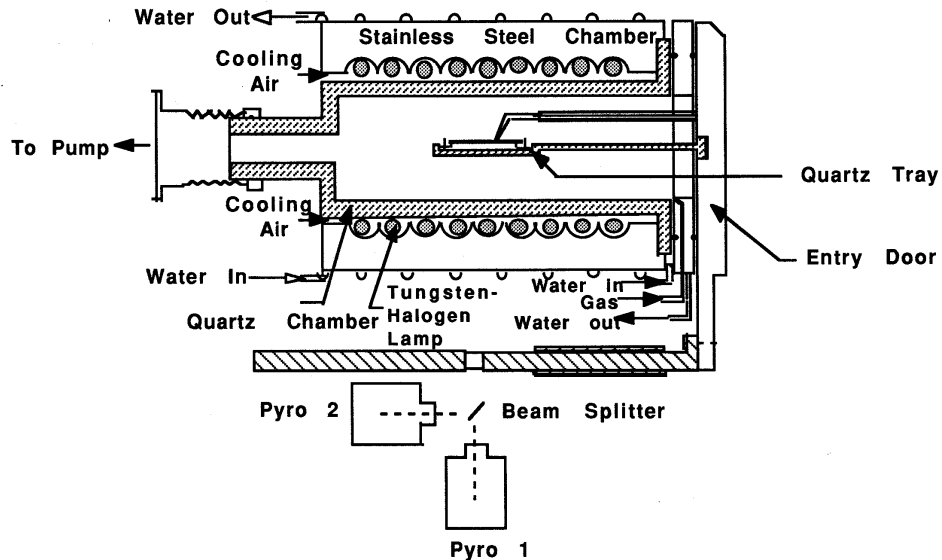


Figure 4-2. A schematic arrangement of reaction chamber of the RTCVD system

The operation of the RTP CVD system is computer-controlled from an IBM-compatible PC. Simultaneous temperature, gas flow and pressure versus time profiles are defined in a recipe file. During recipe execution, the desired temperature and time recipe is obtained by a closed-loop, real-time temperature control system that regulates the power of lamps every 0.2 s by comparing the signal from the pyrometer (or thermocouple) with the programmed temperature.

During the actual processing, the pyrometer is preferred to a thermocouple, since the latter can react with the processing gases and thereby act as a contamination source. It has also been suggested that the thermocouple is not as accurate as the pyrometer since it

‘sees’ the surrounding and not just the material that it is in contact with.^[11] In addition, the thermocouple can also interfere with the flow pattern of the processing gases which will affect film growth on the substrate. The pyrometers are calibrated against the thermocouples and provide a temperature calibration accuracy of ± 10 °C.

There are six gas cabinets individually equipped with pressure sensors, leak detectors, gas regulators and purging capability. The gas cylinders installed are ultra high purity (UHP, 99.999%) hydrogen (H₂), propane (5% C₃H₈ in H₂), silane (SiH₄), hydrochloride (HCl), dopant (99.999% N₂), and trimethylsilane (3MS, 99.995%). A seventh cylinder of oxygen (O₂) is kept outside the gas cabinets and used only during temperature calibration using a thermocouple. The cylinders are connected to the system via stainless steel tubes. Each gas line has an electronic Mass Flow Controller (MFC) to control the flow rate. Capacities range from 10 sccm to 10 slm.

The versatility of CVD combined with the temperature-time control of RTP has led to a very efficient and economic approach to thin film deposition: rapid thermal CVD. Unlike conventional CVD, in rapid thermal CVD, the gas flow is constant throughout the process and the temperature controls the reaction time. Growth takes place only during the limited period the system is at high temperature. Gas switching occurs during the low temperature segment of the process, thus removing the transient effect of gas residence times. Therefore, rapid thermal CVD has the potential ability to grow structures with very abrupt interfaces between thin films at various temperatures. Furthermore, by simply repeating the process with a series of appropriate gas precursors, a sequence of layers can

be deposited totally in-situ and with minimum high temperature exposure. Moreover, each layer can be rapidly deposited at its optimum temperature, something that is very difficult to do in a conventional CVD system where the temperature stabilization is quite lengthy. The combination of these characteristics makes rapid thermal CVD an interesting alternative to conventional CVD for the growth of hetero-structures and for in-situ conformal and non-conformal growth.

The advantages of the rapid thermal CVD setup over a conventional CVD one can be summarized as follows:

1. Ability to grow very thin films
2. Ability to grow multi-layers in-situ
3. Ability to grow films at higher temperatures while still maintaining an overall restricted thermal budget.
4. Ability to tailor the ramp-rate over a much wider range than in a conventional reactor
5. Elimination of contamination from a conventional susceptor.

4.2.2 Sample preparation

The quartz tray that holds the wafer inside the chamber is designed to hold only a 3" wafer. The low-stress, amorphous Si₃N₄/Si wafers come in size of 4" from Cronos. In order to optimize the size of samples and the cost of the wafers, they were cut into pieces that were about 1 x 1 cm² in dimension. The 1 x 1 cm² pieces can, of course, not be kept

by themselves on a quartz tray that supports a 3" wafer. In order to accomplish this, we used a 3" Si wafer as the main susceptor, and had one smaller piece of Si wafer serving as a block for the $1 \times 1 \text{ cm}^2$ $\text{Si}_3\text{N}_4/\text{Si}$ pieces. The block is essential since the tray is usually kept at a slight angle from the horizontal, which means that the $1 \times 1 \text{ cm}^2$ $\text{Si}_3\text{N}_4/\text{Si}$ pieces might move immediately after it is loaded into the chamber and the evacuation process of

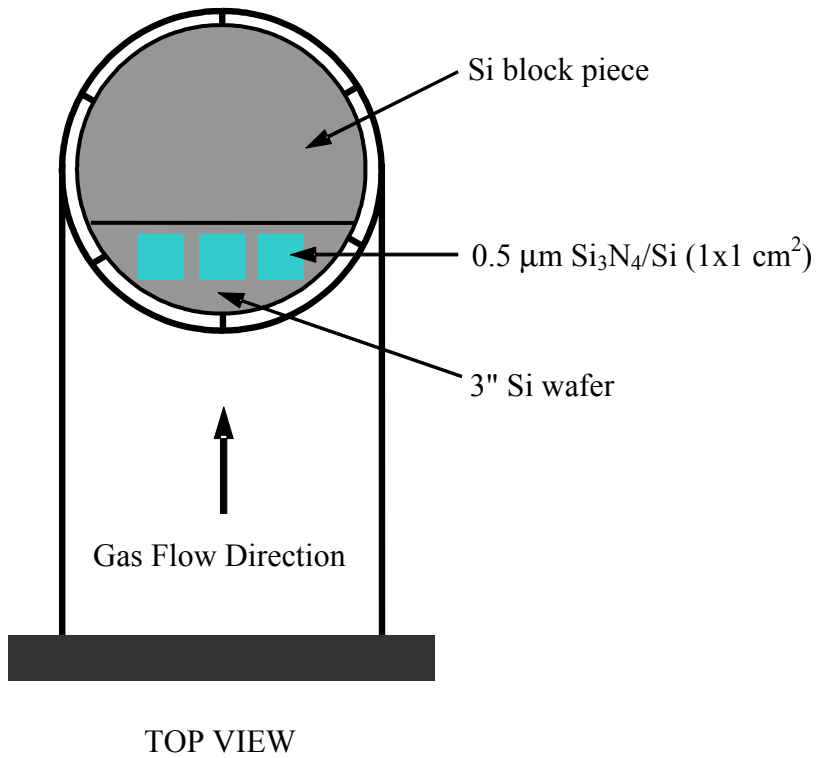


Figure 4-3. Arrangement of the sample and Si wafer pieces.

the chamber is executed or when the gases start flowing during the actual processing. It is important to prevent any movement since exact positioning of the sample is crucial for optimum growth. Fig. 4-3 shows a schematic of how the sample is blocked.

Using a cutting pen with diamond tip, the Si block can be simply cleaved from a regular 3" Si wafer. The $\text{Si}_3\text{N}_4/\text{Si}$ pieces can also be cleaved easily if the base Si substrate is in (100) orientation that will enable square or rectangular pieces to be cut. However, if the base substrate is in (111) orientation, the cleaving process will only yield either

rhombus or a triangle. If the shape and dimension of the pieces are not important, this cutting technique will be sufficient.

4.2.3 Ex-Situ cleaning

Pieces that have been cleaved are then cleaned at room temperature in the following procedure:

1. Dip samples and Si wafer in acetone for 1 minute to remove most organics and particulate impurities;
2. Dip in methanol for 1 minute to further remove organics as well as acetone residuals that do not dissolve in water;
3. Rinse in running deionized (DI) water for at least 1 minute;
4. Dip $\text{Si}_3\text{N}_4/\text{Si}$ samples and Si wafer in 5% HF solution to remove oxides for 30 seconds and 1 minute, respectively;
5. Rinse again in running deionized (DI) water for at least 1 minute;
6. Inspect samples with naked eyes. If necessary, repeat step 1 to 5 until they are cleaned;
7. Blow dry with N_2 air gun.

After all samples and Si wafers are cleaned, they are taken to the RM chamber and loaded in the following sequence:

1. 3" Si wafer
2. Sample block

3. Si₃N₄/Si samples

The chamber door is then closed and the isolation valve is opened to pump down the chamber to about 3 millitorr. This usually takes about an hour.

4.2.4 In-Situ cleaning

This in-situ cleaning is performed to remove any thin layer of native oxide that might have grown during the pump-down period. In the in-situ cleaning, the wafer temperature is ramped up to 1100 °C with 1 slm H₂ flowing. The wafer is maintained at 1100 °C for 30 seconds and then cooled down to room temperature.

4.2.5 Growth with trimethylsilane

All experiments of SiC growth were conducted using the precursor, trimethylsilane (CH₃)₃SiH – (referred to in the rest of this thesis as 3MS) – which contains both silicon and carbon. The linear chain structure of a 3MS chain is shown in Fig. 4-4. As a single organosilane precursor, 3MS is recognized to be non-pyrophoric, non-corrosive, and easier to handle than the conventional SiH₄/C₃H₈/H₂ gas system used for SiC growth. By using 3MS and low pressure CVD, Rodriguez-Vieho *et al.* reported that <111> oriented polycrystalline SiC film can be grown on SiO₂ [12] and Kim *et al.* reported that single crystalline SiC could be grown on Si₃N₄. [13]

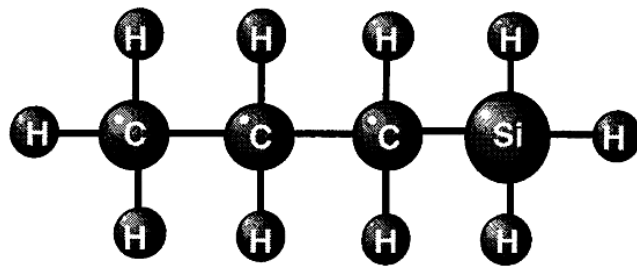


Figure 4-4. Linear chain structure of a 3MS $[(\text{CH}_3)_3\text{SiH}]$ molecule.

For all SiC-growth experiments reported in this chapter, the hydrogen flow rate is 1 slm, and the 3MS flow rates range from 20 to 40 sccm, while nitrogen flow rates vary from 0 to 10 sccm. The growth temperature is in the range of 1100 to 1250 °C, the growth time is 3 to 6 minutes, and temperature ramp rate is 25 °C/second. To get a SiC film with higher uniformity, we divide the total growth time into two equal ones and grow SiC film twice with a 180° manual rotation in between. Fig. 4-5 shows the recipe for SiC growth using 3MS. In order to evaluate the influence of growth temperature on structural and

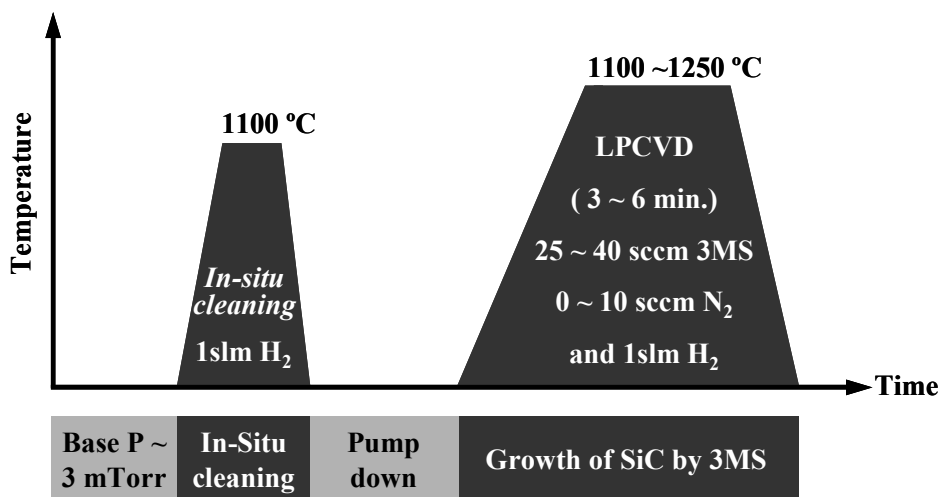


Figure 4-5. Recipe for SiC growth using 3MS

electrical properties, four different values were selected: 1100, 1150, 1200, and 1250 °C.

4.2.6 In-Situ nitrogen doping

The in-situ nitrogen doping during SiC-growth by CVD can eliminate the structural damage and stress in the film caused by alternative doping with ion implantation. There is no need for post-annealing at high temperature (usually >1500 °C) to repair the damage.

In this study, to investigate the doping effect of N₂ flow rate on the electrical properties of SiC films, two sets of growth conditions were chosen: (1) 0, 1, 2, and 10 sccm N₂ with constant 25 sccm 3MS at 1250 °C; (2) 2, 5, and 10 sccm N₂ with constant 40 sccm 3MS at 1200 °C. The flow rate of H₂ was kept at 1 slm all the time.

4.3 Characterization of as-grown SiC thin-film

The crystal structure of as-grown SiC films was characterized by XRD spectra. The surface morphology of the SiC films and the SiC/Si₃N₄ interface was examined by SEM. The surface roughness of the SiC films was studied by AFM. The SiC-film thickness of samples used for Hall measurements ranged from 1–2 μm. Electrical properties of grown SiC films were investigated using MMR Corporation's (California, USA) Hall-effect measurement system with a magnetic field up to 1.2 T. Electrical contacts were made by depositing Ni on the four corners of the sample using electron-

beam evaporation followed by annealing at 900 °C for 5 min. The quality of the electrical contacts was evaluated by checking the linearity of their current-voltage (I-V) relation. The magnetic field was set at 1 T (10,000 Gauss) for all Hall-effect measurements.

4.3.1 Characterization techniques

—*X-ray diffraction (XRD)*

A beam of x-rays directed at any material will be scattered in all directions. A diffracted beam is composed of a large number of scattered rays that mutually reinforce each other. This means that the intensity of the scattered beam is highest in the diffraction condition. For crystalline materials, the intensity of the radiation scattered in certain directions will be much stronger depending on the crystal planes that scatter them. For polycrystalline materials, peaks in the intensity profile are obtained in a number of different directions dependent on the different crystal planes off which diffraction is obtained. For mono-crystalline materials, the peak in the profile is obtained in directions specific to one family of planes.

According to the Bragg law, $\lambda = 2d \sin\theta$, where λ is the wavelength of the radiation hitting the sample, d is the interplanar spacing of the planes reflecting the radiation, and θ is half of the angle between the diffracted and transmitted beam. By using x-ray radiation of known wavelength, and measuring the angle θ , it is possible to determine the spacing d of various planes in a crystal, and thereby identify the material and the planes diffracting the x-ray beam. Fig. 4-6 [14] shows the essential features of an

x-ray diffractometer. X-rays from the tube T are incident on a crystal, C, which may be set at any desired angle with respect to the incoming radiation by rotating it about an axis through O, the center of the diffractometer circle. The intensity of radiation diffracting off from the C is measured in a detection counter, G that also rotates about an axis through O. The various components are arranged so that if C is moved through an angle θ , the detector, G moves through an angle 2θ . By moving C through a specified angular range, it is possible to determine the angular position at which the intensity plot shows peaks. Peak analysis can give qualitative information on the amount and quality of material.

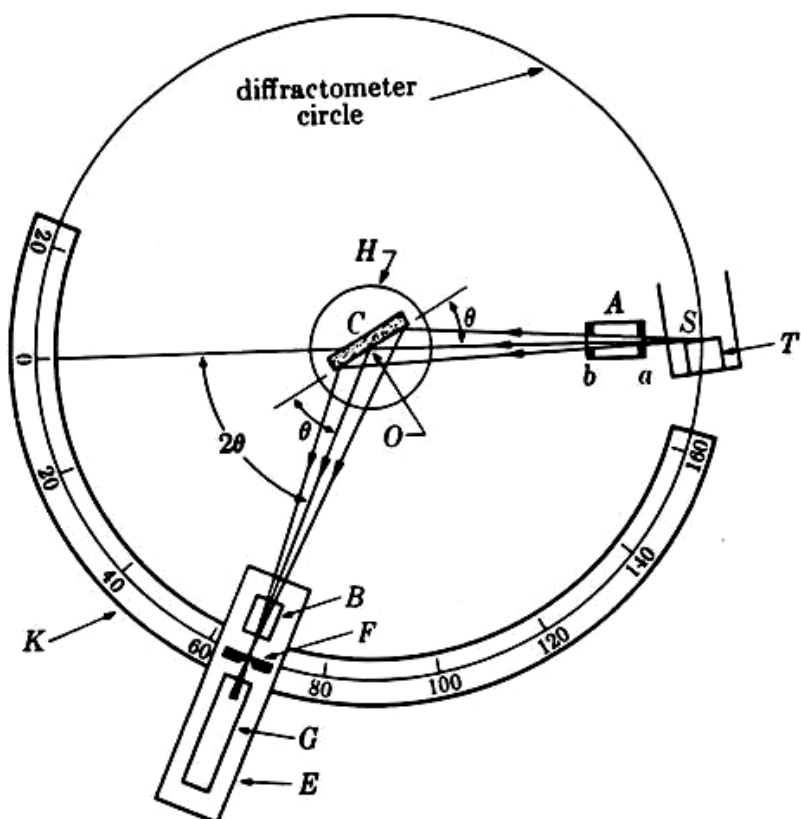


Figure 4-6. A schematic of X-ray diffractometer

The diffractometer used in this study was a Rigaku MiniFlex XRD system that allowed rotation of the sample about an axis perpendicular to its top surface. This was useful in aligning the mono-crystalline sample so that the diffracting planes would be aligned to give the maximum diffraction intensity.

The angular positions of interest in this study were as follow:

$$\begin{array}{lll} \text{Si (111)} = 28.4^\circ & \text{Si (200)} = 32.96^\circ & \text{Si (400)} = 69314^\circ \\ \text{3C-SiC (111)} = 35.6^\circ & \text{3C-SiC (200)} = 41.59^\circ & \text{3C-SiC (220)} = 60.0^\circ \\ \alpha\text{-Si}_3\text{N}_4 (200) = 26.44^\circ & \alpha\text{-Si}_3\text{N}_4 (200) = 35.35^\circ & \end{array}$$

—Scanning Electronic Microscopy (SEM)

In the SEM, a focused beam of electrons is rastered across a sample surface, the raster scan being synchronous with that of a cathode ray tube (CRT). The brightness of the CRT is modulated by the detected secondary electron current from the sample, such that the viewing CRT displays an image of the variation of secondary electron intensity with position on the sample. This variation is largely dependent on the angle of incidence of the focused beam on the sample, thus yielding a topographical image. Different detectors can be used to provide alternative information, e.g., a back-scattered electron detector will provide average atomic number information. As shown in Fig. 4-7, in normal SEM image observation, the second condenser lens (CL2) provides a crossover image (A point) for the objective lens (OL). Scanning coils SC1 and SC2 are energized and the incident beam scans the specimen surface through two stages with two sets of scan coils.

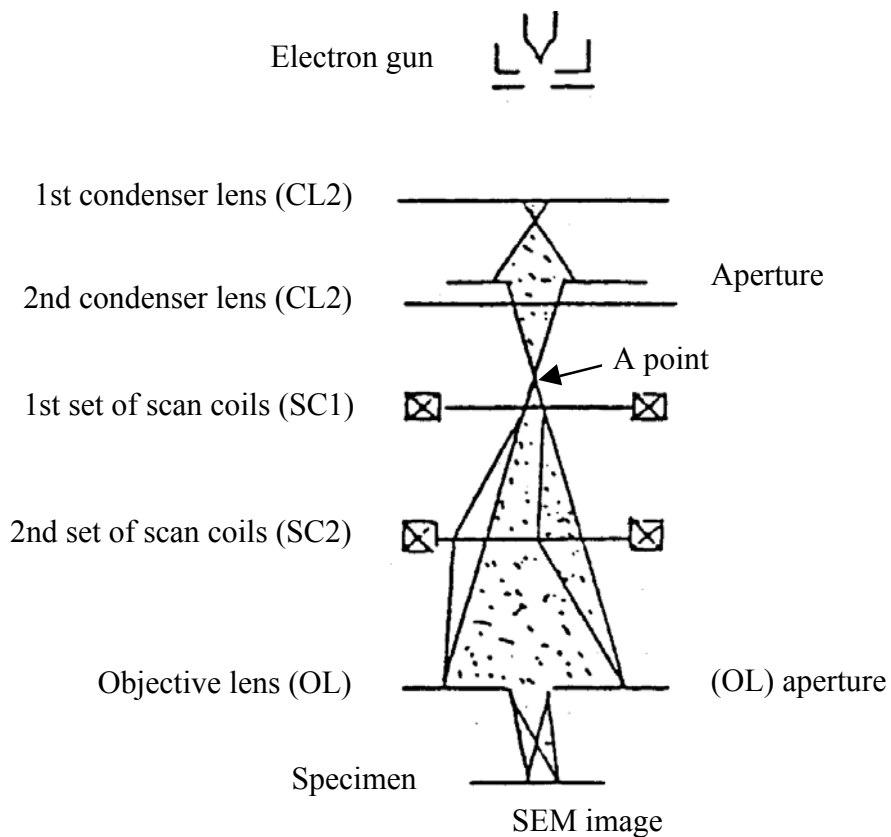


Figure 4-7. Electron beam diagram when observing SEM image.

A typical SEM sample stub is shown in the Fig. 4-8. The sample to be imaged is cleaved to a size smaller than the stub diameter and glued to it using conducting silver paste. Larger samples may be placed on a larger sample holder. Sometimes, it is convenient to glue more than one sample on the larger holder and image them one by one inside the SEM, instead of breaking vacuum to remove the smaller stub and glue a new sample on. The holder is then introduced into the chamber and pumped down. Following this, the sample is imaged in the conventional manner. The sample can be tilted to any angle from 0 to 90 °. This helps in getting a 3D perspective of the sample surface and the cross section of the interface between layers or layer and substrate.

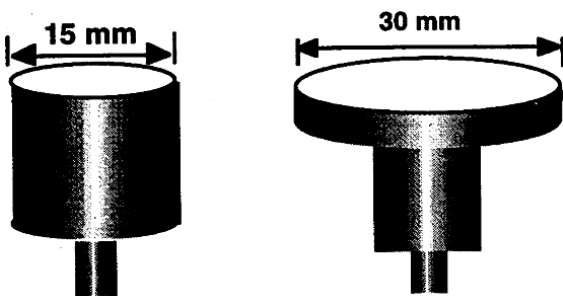


Figure 4-8. SEM sample stubs.

—*Atomic Force Microscopy (AFM)*

AFM is a variation on a method of imaging surfaces with atomic or near-atomic resolution called scanning probe microscopy (SPM). A small tip scans across the surface of a sample in order to construct a 3-D image of the surface. Fine control of the scan is accomplished using piezoelectrically induced motions. Any type of surface can be probed by the molecular forces, which are exerted by the sample surface against the tip. The tip can be constantly in contact with the surface; or it can gently tap the surface while oscillating at high frequency; or it can be scanned just minutely above the surface. The main advantages of using an AFM are:

- Measurements made under ambient conditions
- Little or no sample preparation or alteration
- Surface images are digitally acquired, stored, and manipulated
- The roughness of the sample surface can be quantified.

The instrument used in this project is a Nanoscope DimensionTM with integrated acoustic/vibration isolation system manufactured by Digital Instruments in California, as

seen in Fig. 4-9. It is a low-noise system specifically designed to produce measurements at the nanometer (lateral) and sub-angstrom (vertical) scales. The isolation system allows to image surfaces with roughness levels of < 10 nm RMS, where ground vibration and/or acoustic noise are prevalent. A sample of maximum diameter 15mm can be accommodated on this instrument. The sample is initially viewed using a CCD camera and imaged on a computer monitor. The area that needs to be imaged using the AFM can be first selected and the cantilever is brought down until it makes contact with the sample. The cantilever tip then scans over the desired area and the scanned image is displayed on the monitor. Scan area of up to 100 μm by 100 μm can be imaged.

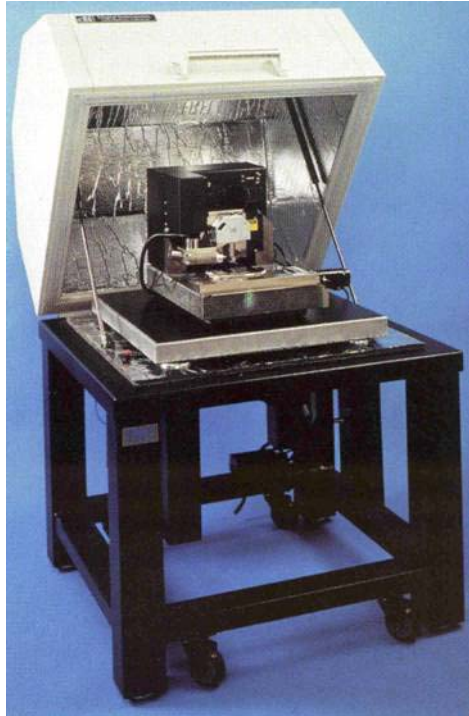


Figure 4-9. The Nanoscope DimensionTM AFM with integrated acoustic/vibration isolation system manufactured by Digital Instruments in CA

—Hall Effect Measurement

To accurately measure the resistivity, sheet resistance and carrier concentration directly, the most common method uses the Hall effect.^[15] Fig. 4-10 shows the basic setup^[16] where an electric field is applied along the axis x and a magnetic field is applied along the axis z . Consider a p -type sample. The Lorentz force ($qv_x \times B_z$) exerts an average downward force on the holes, and the downward-directed current causes a piling up of holes at the bottom side of the sample, which in turn gives rise to an electric field E_y . Since there is no net current along the y direction in the steady state, the electric field along the axis y (Hall field) exactly balances the Lorentz force. This Hall field can be measured externally and is given by

$$E_y = (V_y / W) = R_H J_x B_z ,$$

where R_H is the Hall coefficient and is given by^[17]

$$R_H = r \frac{1}{q} \frac{p - b^2 n}{(p + bn)^2}, \quad \text{where } b \equiv \frac{\mu_n}{\mu_p}, \quad \text{and } r \equiv \langle \tau^2 \rangle / \langle \tau \rangle^2.$$

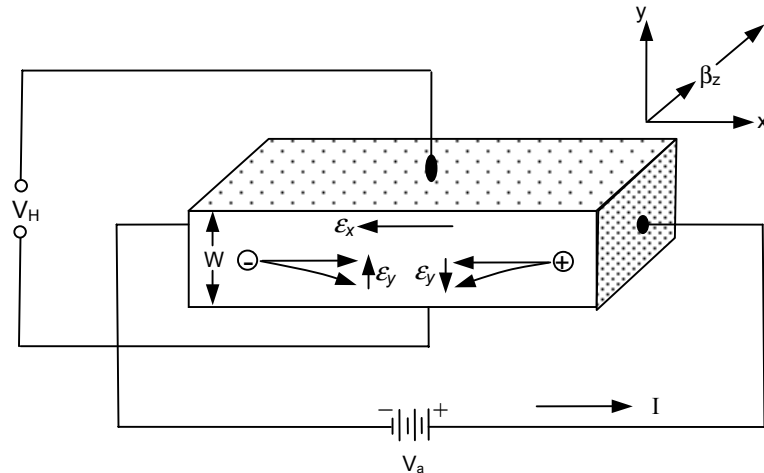


Figure 4-10. Basic setup of Hall effect measurement

The parameter τ is the mean free time between carrier collisions, which depends on the carrier energy. The parameters μ_n and μ_p are the electron and hole drift mobility, respectively.

In this study, we use a Hall and Van Der Pauw measurement system from MMR Technology. It includes a K-20 programmable temperature controller, H-50 Hall and Van Der Pauw controller, MPS-50 programmable power supply, M-50 benchtop electromagnet, MMR thermal stage with cryogenic refrigerator, Dewar and vacuum accessories. System control is provided by an IBM compatible computer. The K-20 temperature controller adjusts and maintains the temperature of the MMR thermal stage over a wide temperature range, with high accuracy and stability. The H-50 Hall and Van Der Pauw controller provides four probe method measurements of the electrical parameters of the samples. The M-50 benchtop electromagnet provides the magnetic field over the studied sample and the MPS-50 programmable power supply controls the magnitude of that magnetic field. These scientific instruments were designed as separate computer controlled devices. This MMR's Hall System allows the user to make automatic measurements of resistivity, mobility and carrier concentration of a wide range of samples using the Van Der Pauw method over a temperature range from 80 K to 400 K.

4.3.2 Structural properties of SiC films measured by XRD

The θ - 2θ XRD spectra for SiC films grown on $\text{Si}_3\text{N}_4/\text{Si}$ at different growth temperature are shown in Fig. 4-11. The spectra were normalized by the thickness of SiC

films. These spectra show that poly-crystalline SiC films oriented in the $<111>$ direction were obtained at growth temperatures from 1150°C to 1250°C. No other orientations of SiC films were detected. The normalized XRD intensity of the SiC (111) peak is plotted in Fig. 4-12 as a function of growth temperature. As expected, the SiC $<111>$ signal increased with temperature from 1100°C to 1200°C, but decreased when the temperature was increased to 1250°C.

To understand the cause for this decrease, we investigated the properties of the Si_3N_4 layer under annealing conditions chosen

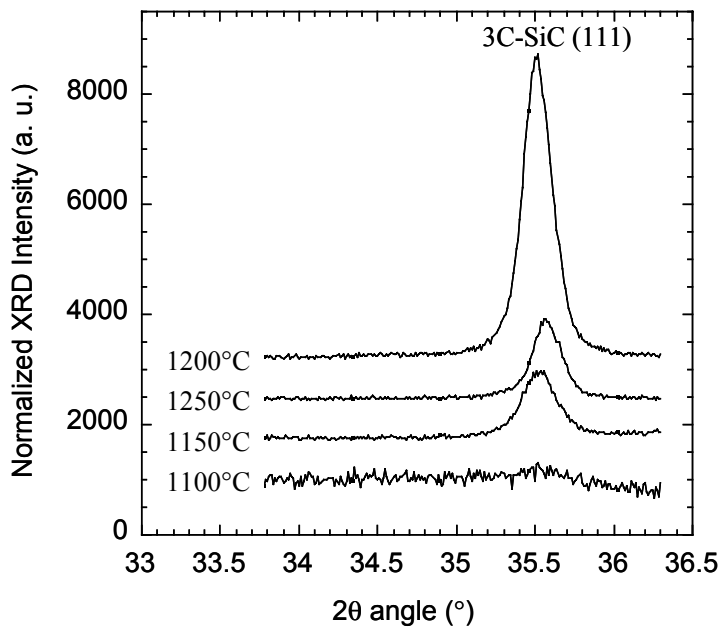


Figure 4-11. Normalized XRD spectra for SiC films grown on $\text{Si}_3\text{N}_4/\text{Si}$ at different temperatures. Flow rates: 30 sccm 3MS, 1 sccm N_2 .

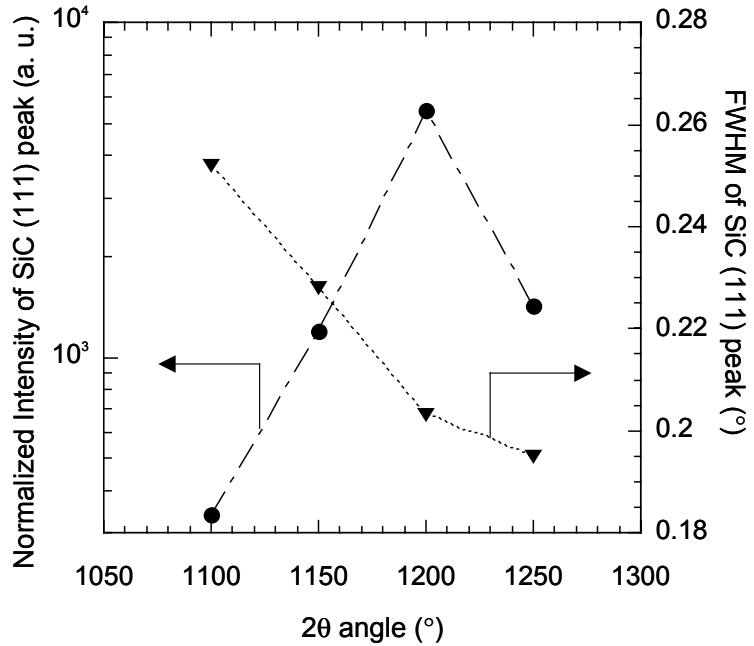


Figure 4-12. Normalized XRD intensity of the SiC (111) peak as a function of growth temperature. Flow rates constant at 30 sccm 3MS and 1 sccm N_2 .

to simulate the SiC growth process. Fig. 4-13 contains XRD spectra of the Si_3N_4 layers annealed at temperature from 1100°C to 1250°C . The spectra indicate that the Si_3N_4 layer remains amorphous after anneals up to 1200°C for several minutes. However, after annealing at 1250°C , two XRD peaks at 2θ angles of 26.437° and 35.350° are observed. The peaks correspond to $\alpha\text{-Si}_3\text{N}_4 <200>$ and $<210>$ directions. We suspect that the crystallization of Si_3N_4 layer could be the reason for the decrease of XRD signal of SiC $<111>$ orientation at a growth temperature of 1250°C . Interestingly, the full width at half maximum (FWHM) of the SiC (111) XRD peak decreases monotonically with increasing SiC growth temperature, ranging from 0.25° at 1100°C to 0.18° at 1250°C .

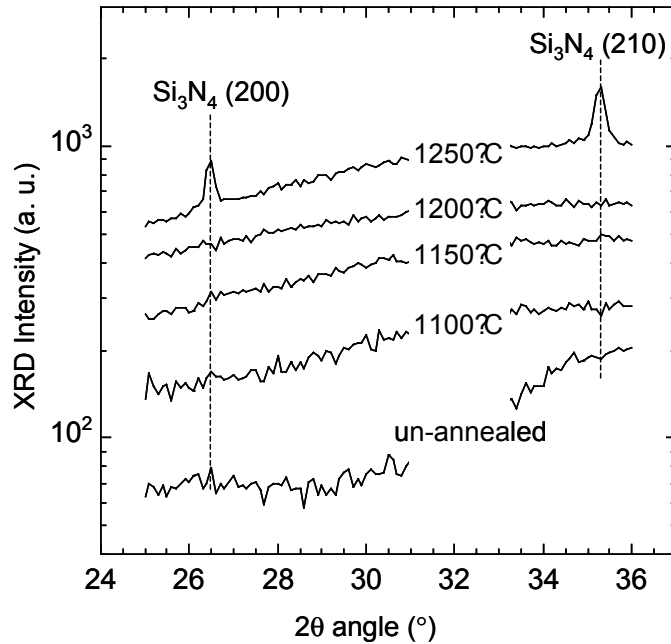


Figure 4-13. XRD spectra of Si_3N_4 layer un-annealed and annealed at the temperatures used for SiC growth.

The effect of 3MS flow rate on the crystallinity of the SiC films was also investigated. Fig. 4-14 indicates that increasing the 3MS flow rate in a certain range at a growth temperature of 1200°C results in a significant increase in the XRD intensity and a slight decrease in the FWHM of SiC (111) peak. In the following Hall effect

measurement, we investigated how the crystallinity affects the resistivity and sheet resistance of SiC films grown under various conditions.

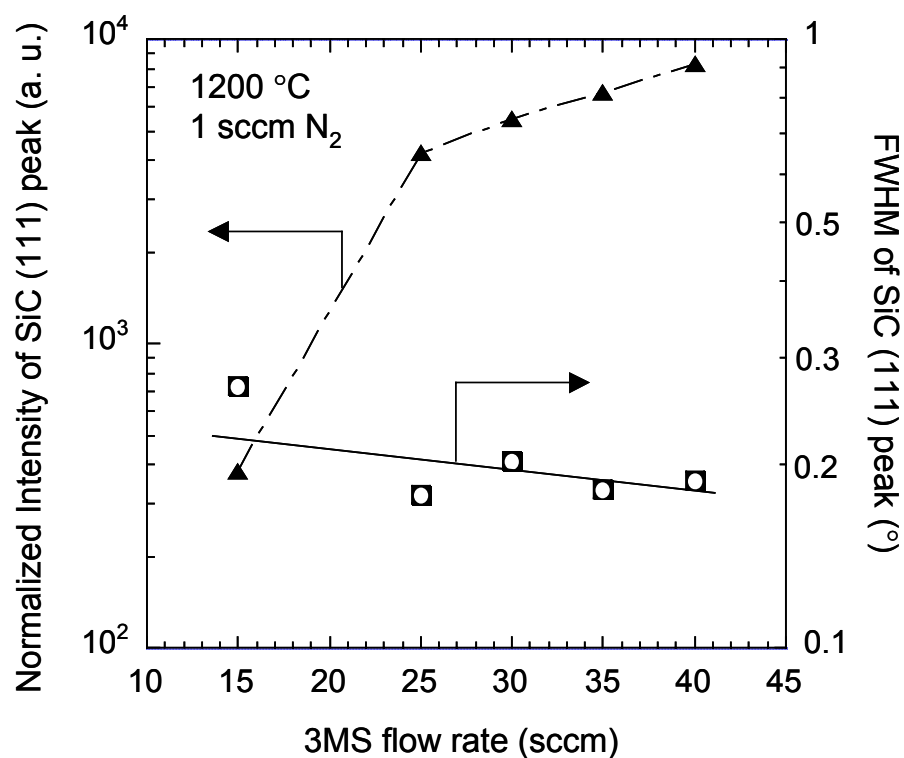


Figure 4-14. Normalized XRD intensity and FWHM of SiC (111) peak as a function of 3MS flow rate. Growth temperature is 1200°C and N₂ flow rate is 1 sccm.

4.3.3 Electrical properties of SiC films grown with constant 1 sccm N₂ flow rate

Fig. 4-15 shows the resistivity and sheet resistance of SiC films as a function of growth temperature with flow rates of 30 sccm 3MS and 1 sccm N₂. The lowest

resistivity and sheet resistance were obtained at 1200°C, which also resulted in the best crystallinity as seen in the XRD data of Fig. 4-11 and Fig. 4-12.

By increasing the 3MS flow rate we observed that the resistivity and sheet resistance decreased, as shown in Fig. 4-16, while the normalized XRD intensity of the SiC (111) peak increased (see Fig. 4-14). These results are consistent with the general observation that improvements in semiconductor yield improved electrical properties.

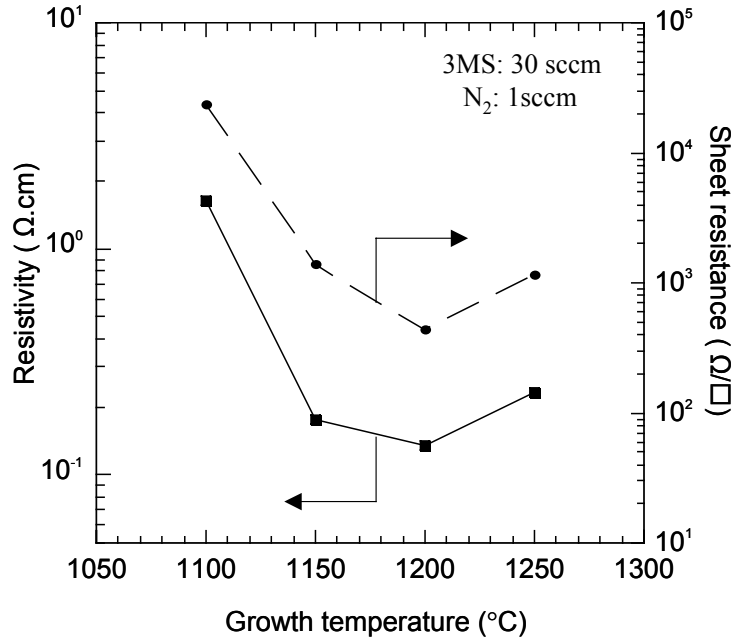


Figure 4-15. Resistivity and sheet resistance of SiC films at 300K as a function of growth temperature.
Flow rates: 30 sccm 3MS and 1 sccm N₂.

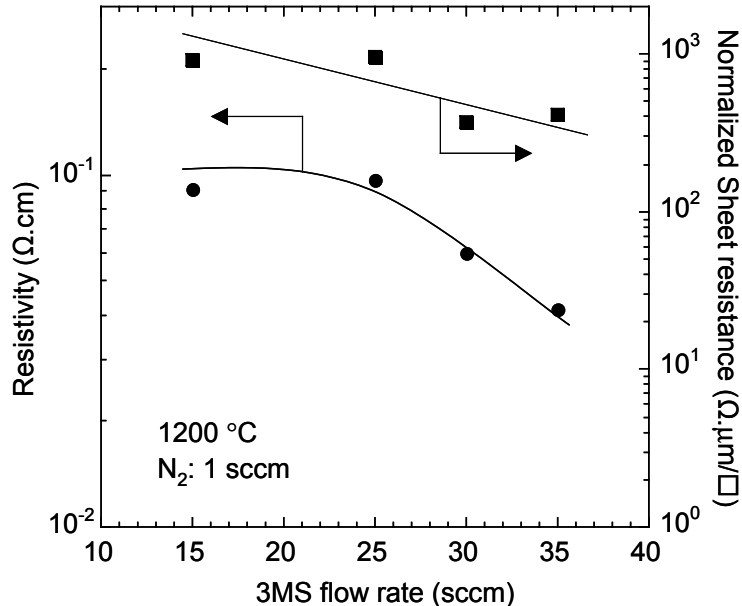


Figure 4-16. Resistivity and sheet resistance of SiC films at 300 K as a function of 3MS flow rate.
Growth temperature: 1200°C, N₂ flow rate: 1 sccm.

4.3.4 Electrical properties of SiC films versus different N₂ flow rates

The effect of the N₂ flow rate on the SiC electrical properties was studied for two sets of growth conditions. The first used a lower 3MS flow rate (25 sccm) at 1250°C, while the second used a higher 3MS flow rate (40 sccm) at 1200°C. The N₂ flow rate was varied from 0 sccm to 10 sccm. For both sets of operating parameters, the data of Fig. 4-17 show the same trend of decreasing resistivity and sheet resistance with increasing N₂ flow rate. This indicates that an increasing number of N atoms incorporated into the SiC film helps to lower the resistivity and sheet resistance.

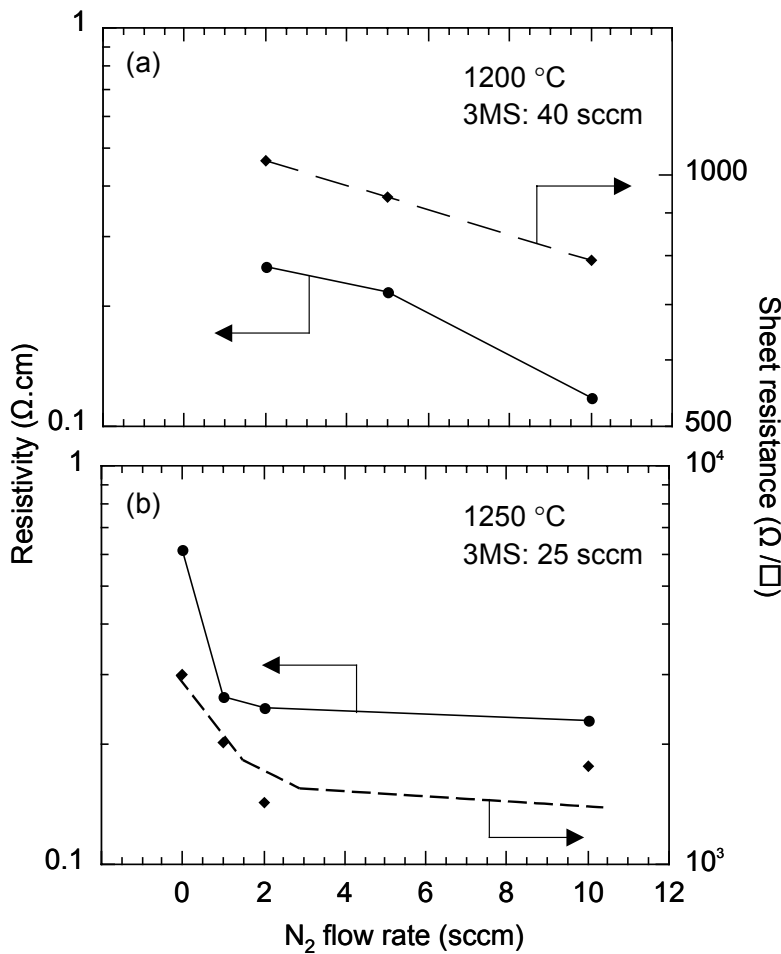


Figure 4-17. Resistivity and sheet resistance of SiC films at 300K as a function of N₂ flow rate: (a) growth temperature: 1200°C, 3MS flow rate: 40 sccm; (b) growth temperature: 1250°C, 3MS flow rate: 25 sccm.

4.3.5 Surface morphology of SiC films examined by SEM and AFM

The surface and interface quality was examined by SEM. As shown in Fig. 4-18, the surface morphology of SiC film becomes worse with increasing growth temperature, while the SiC-Si₃N₄ interface is very smooth and free of voids for all samples. Clearly, the Si₃N₄ layer prevents Si out-diffusion from the substrate and subsequent reaction with C or H from the gas phase, which causes the formation of voids at the SiC-Si interface during growth directly on a Si substrate or layer.

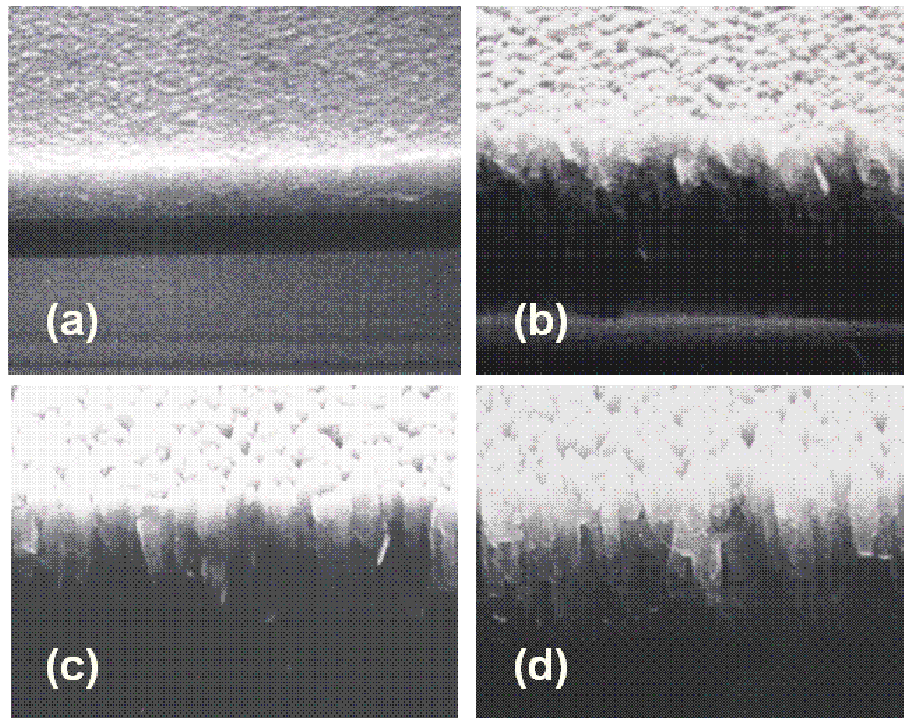


Figure 4-18. SEM micrographs of SiC thin films grown on Si₃N₄/Si structures with 30 sccm 3MS and 1 sccm N₂ at the following temperatures: (a) 1100°C; (b) 1150°C; (c) 1200°C; (d) 1250°C.

Fig. 4-19 compares SiC growth rate and surface roughness as a function of growth temperature that is also clearly revealed by 3-D AFM micrographs in Fig. 4-20. The root mean square (RMS) roughness measured by AFM and the growth rate both increase with increasing growth temperature, which conforms to the results of surface morphology observed by SEM. The SiC film thickness, measured using cross-sectional SEM, ranges from 0.7 to 3 μm . The growth rate obtained at the optimum temperature of 1200°C is about 0.5 $\mu\text{m}/\text{min}$, while the RMS surface roughness is approximately 40 nm.

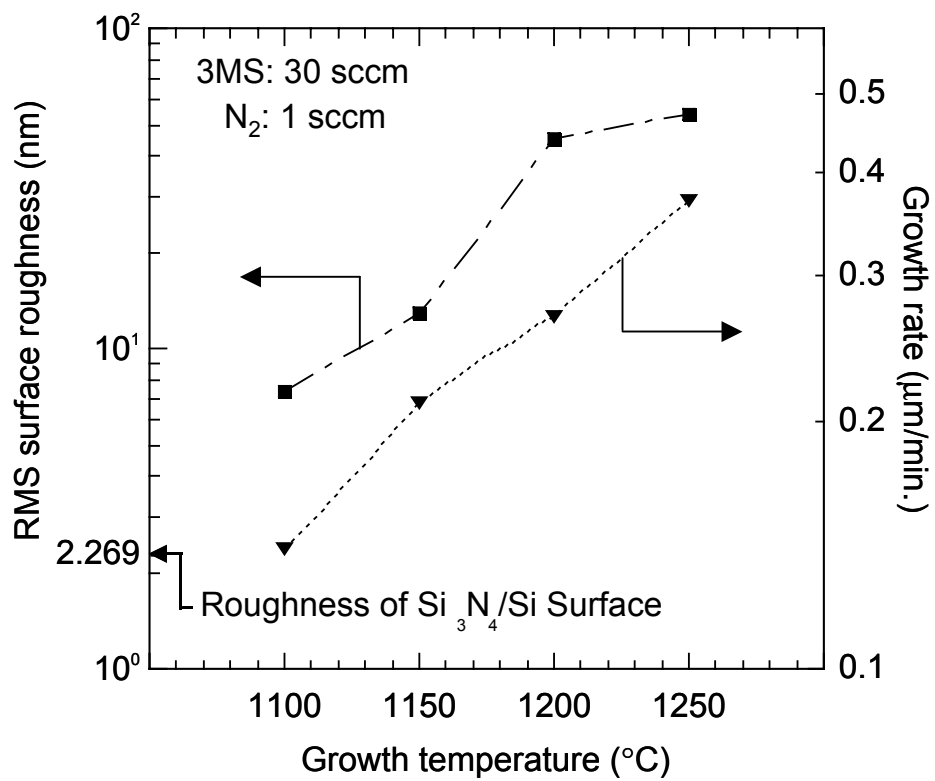


Figure 4-19. Growth rate and surface roughness of SiC films versus growth temperature.

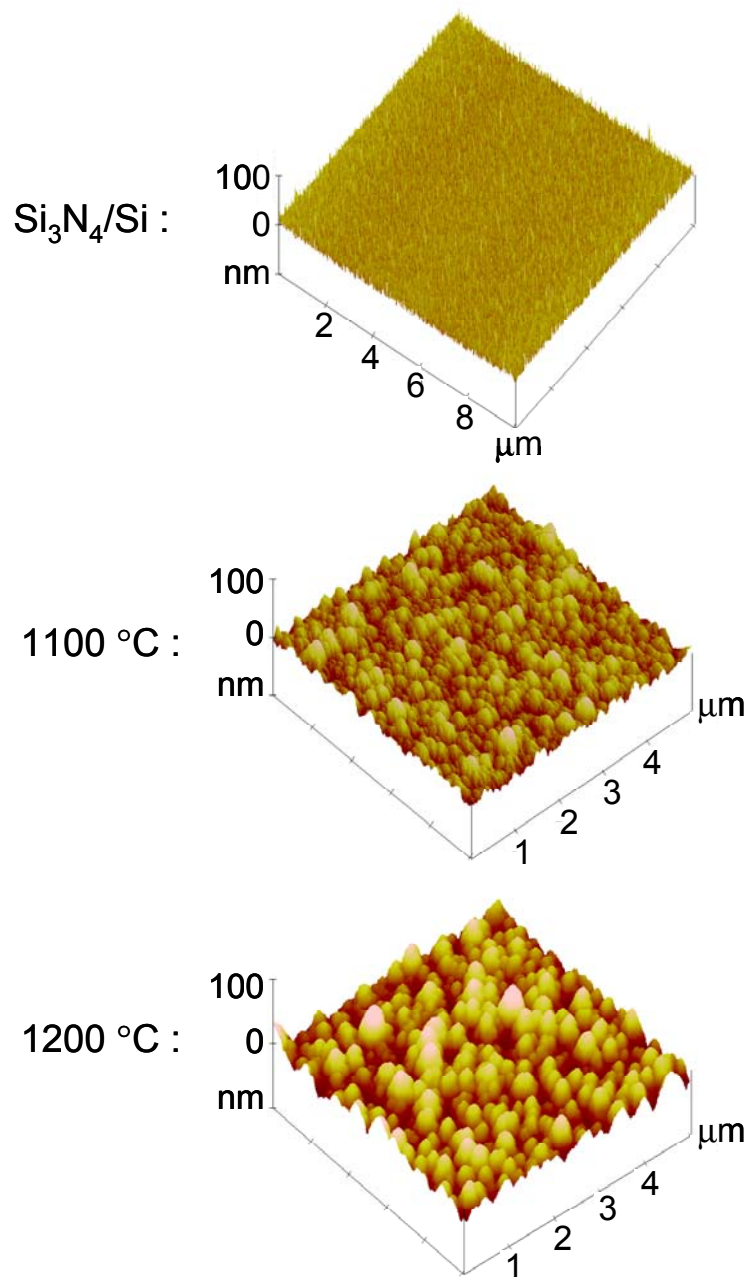


Figure 4-20. AFM micrographs of starting $\text{Si}_3\text{N}_4/\text{Si}$ surface and SiC film surface grown at 1100°C and 1200°C . Flow rates: 30 sccm 3MS, 1 sccm N_2 .

4.3.6 Initial efforts on MEMS fabrication

SiC film samples grown on $\text{Si}_3\text{N}_4/\text{Si}$ (100) substrate materials were patterned and processed in initial MEMS fabrication efforts. The previous results on SF_6 RIE etching of $\text{SiC}/\text{Si}_3\text{N}_4/\text{Si}$ and $\text{SiC}/\text{poly-Si}/\text{Si}_3\text{N}_4/\text{Si}$ MEMS structures done by J. Scofield [2] are shown in Fig. 4-21. It has been shown that LPCVD conformal growth of SiC on low-stress amorphous Si_3N_4 layer is successful. Simple MEMS structures such as cantilevers, lateral resonators and resonating membranes have been fabricated. The film stress was measured by using bent-beam strain gauges. The deflecting angle of our bent-beam is 6° . The residual stress generated by a bimorph involving a SiC thin film has been estimated at ~ 188 MPa. Lateral deflection of the supporting beam vernier structures correlates directly to the stress in the deposited film. Young's Modulus for our SiC films of $E = 426$ GPa used for stress calculations was obtained from MEMS resonance measurements for SiC films.

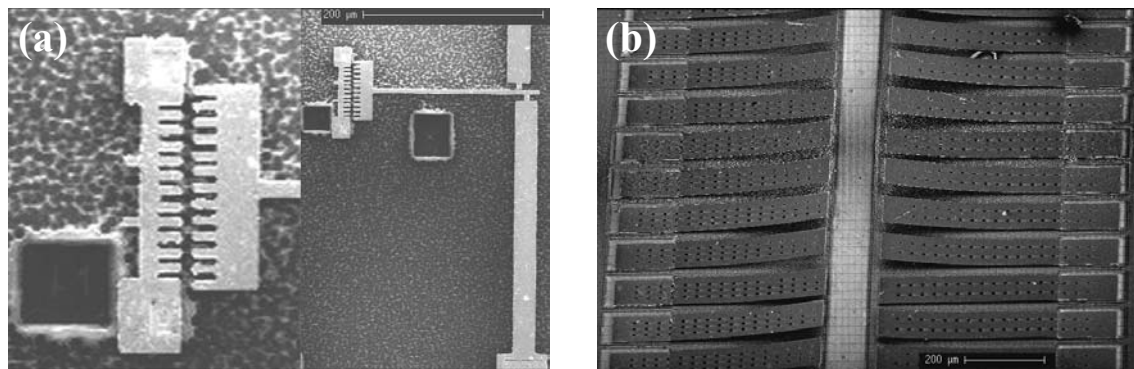


Figure 4-21. SEM micrographs of SiC MEMS structures: (a) film stress diagnostic indicator gauge; (b) residual stress cantilever beams.

In this study, we used inductively coupled plasma etching with NF₃/Ar mixtures, which give higher etch rate and lower damage than RIE etching. As discussed in Chapter 5, vertical sidewalls indicating high anisotropy NF₃/Ar etching have been obtained under specific etching conditions.

4.4 Conclusion

We have reported on the fabrication and properties of SiC structures for high temperature MEMS applications. The MEMS device requires the growth and doping of SiC thin films on amorphous Si₃N₄ layers on Si substrates. The SiC films were grown by CVD with the single organosilane trimethylsilane, while the in-situ doping was performed by addition of N₂ into the reaction chamber. A resistivity of 75Ω/□ was measured for the doped SiC film when operating the structure at 400K. MEMS structures such as cantilevers, lateral resonators and membranes were successfully fabricated.

4.5 References

- [¹¹] E. Miller, “*Low Stress Silicon Nitride Process Development*”, Washington Technology Center (Oct. 2001)
- [¹²] J. Chen, J. Scofield, and A.J. Steckl, *J. Electrochem. Soc.* **147**, pp. 3845-3849 (2000)
- [¹³] M. Mehregany, C.A. Zorman, N. Rajan, and C.H.Wu, *Mater. Sci. Forum* pp. 338–342, 541 (2000)
- [¹⁴] D. Brady, V. H. C. Watt, A. Karamchetti, G. Bersuker, S. Kim, L. Vishnubhitla, P. Zietzoff, M. Gilmer, J. Guan, K. Torres, B. Nguyen, g. Williamson, G. Brown, G. Gale, M. Jackson, and H. R. Huff, in *SILICON NITRIDE AND SILICON DIOXIDE THIN INSULATING FILMS*, Proc. 5th International Sym., **99-6**, eds.: K. B. Sundaram, M. J. Deen, W. D. Brown, R. E. Sah, E. Poindexter, and D. Misra, The Electrochemical Society Inc., NJ (1999)
- [¹⁵] L. Cheng, M. Pan, J. Scofield, and A. J. Steckl, *J. Electronic Materials*, Vol. 31, No. 5 pp. 361-365 (May, 2002)
- [¹⁶] S. M. Sze, in *Physics of Semiconductor Devices*, 2nd ed., John Wiley and Sons, Inc, New York, p. 852 (1981)
- [¹⁷]http://www.microlab.ucla.edu/pdf/week4_CVD.pdf
- [¹⁸] T. Searle, editor, in *Properties of amorphous silicon and its alloys*, INSPEC, London (1998)
- [¹⁹] C. H. Mastrangelo, Y. C. Tai, and R. S. Muller, “Thermophysical Properties o f Low-residual Stress, Silicon-rich, LPCVD Silicon Nitride Films”, *Sensors and Actuators A*, **23** pp. 856-860 (April, 1990)

-
- [¹⁰] AET Addax Inc. (now AET Thermal Inc., 695 E. Brokaw Rd., San Jose, CA 95112, Phone: (408) 573-8898, FAX: (408) 573-8988)
- [¹¹] P. Vandenabeele and K. Maex, *Microelectronics Engineering*, **10**, p. 207 (1991)
- [¹²] J. Rodriguez-Vieho, J. Stoemenos, N. Clavaguera, and M. T. Clavaguera-Mora, *J. Cryst. Growth*, **155**, p. 214 (1995)
- [¹³] K. C. Kim, C. Park, K. S. Nahm, E.-K. Suh, in *Proceedings of the 8th international Conference on Silicon Carbide, Related Materials*, Materials Science Forum, Vo. 338-342, p. 317 (2000)
- [¹⁴] B. D. Cullity, *Elements of X-Ray Diffraction*, in *Addison-Wesley Series in Metallurgy and Materials*, M. Cohen, Addison-Wesley Publishing Company, Inc., Philippines, (1978)
- [¹⁵] E. H. Hall, “On a New Action of the Magnet on Electric Currents,” *Am. J. Math.*, **2**, 287 (1879)
- [¹⁶] L. J. Van der Pauw, “A Method of Measuring Specific Resistivity an Hall Effect of Disc or Arbitrary Shape, “ *Philips Res. Rep.*, **13**, 1 (Feb. 1958)
- [¹⁷] R. A. Smith, *Semiconductors*, 2nd ed., Cambridge University Press, London, 1979

CHARPTER 5. PATTERNING OF SiC THIN-FILM ON Si₃N₄/Si FOR ROBUST MEMS APPLICATIONS

5.1 Sample preparation

The samples used were SiC thin-films grown on Cronos' 0.5 μm Si₃N₄ at 1100 and 1200 °C by the LPCVD described in 4.2.1. Thickness of the films is between 2 to 3 μm. The as-grown SiC films were polished by diamond lapping films before patterning. The sample size is about 1 x 1 cm for photolithography. Then each sample is cleaved into four small pieces (5 x 5 mm²) before loaded into the chamber.

The etching was carried out in a Plasma Therm 790 reactor. The ICP source was powered at 100-1000 W (2MHz), while the sample chuck was separately biased with 13.56 MHz power (40-150 W). The process pressure was held constant at 2 mTorr, with the NF₃ or Cl₂ and Ar mixture introduced into the ICP source through mass flow controllers at a total gas flow rate of 15 sccm. The addition of Ar can facilitate ignition of the plasma at low pressure and to enhance the ion-assisted component of the etching.

5.2 Polishing of SiC thin-film

To obtain a good adhesion of masking material on SiC film for a good pattern transfer during the etching process, a good surface morphology and lower RMS surface roughness are required. For this purpose, prior to the ICP etching, surface polishing was

performed on SiC thin film by using 0.5 μm and 0.1 μm diamond lapping films mixed with water sequentially. The improved surface morphology and reduced surface roughness after polishing are shown in Fig. 5-1.

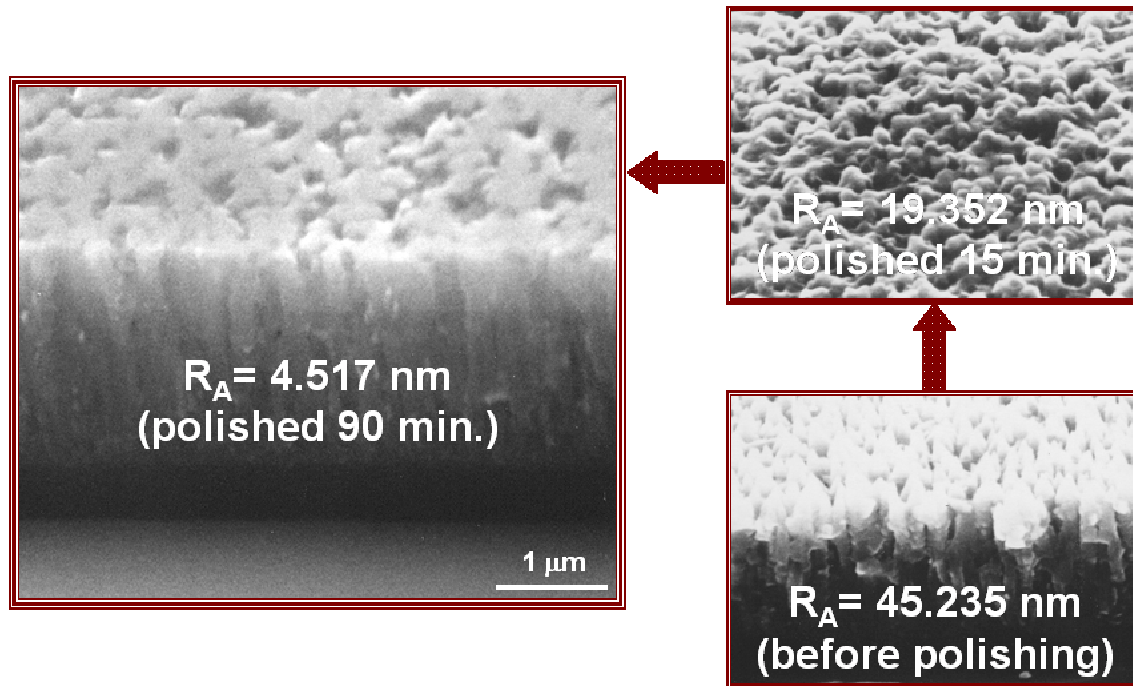


Figure 5-1 SEM micrographs of SiC thin-film grown on $\text{Si}_3\text{N}_4/\text{Si}$ at 1200 °C (a) before polishing, (b) after 15 minutes polish, and (c) after 90 minutes polishing by 0.1 μm diamond lapping films.

To remove the damage produced on the SiC surface during polishing, a dry oxidation at 1200°C followed by a removal of the oxide layer in 5% HF solution was then implemented. The effect of polishing on etching results is reflected in Fig. 5-4 and Fig. 5-5.

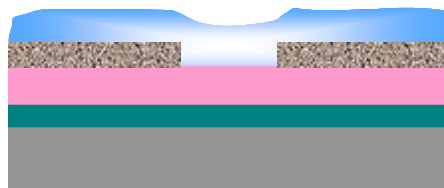
5.3 Photolithography and ITO liftoff

Photolithography is a technique used in the manufacturing of integrated circuits in which nearly coherent light is used to transfer the pattern of mask onto a photosensitive material called photoresist (PR), which has been spread over the wafer. Photoresist is used to mask the wafer from etching, ion implantation, diffusion, and as a sacrificial layer

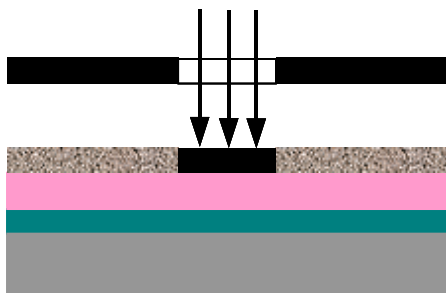
1. (+)ve PR 1818 application



4. Sputter ITO dielectric layer



2. UV expose resist



5. Lift-off photo-resist



3. Develop resist



3. SiC etch and ITO strip-off



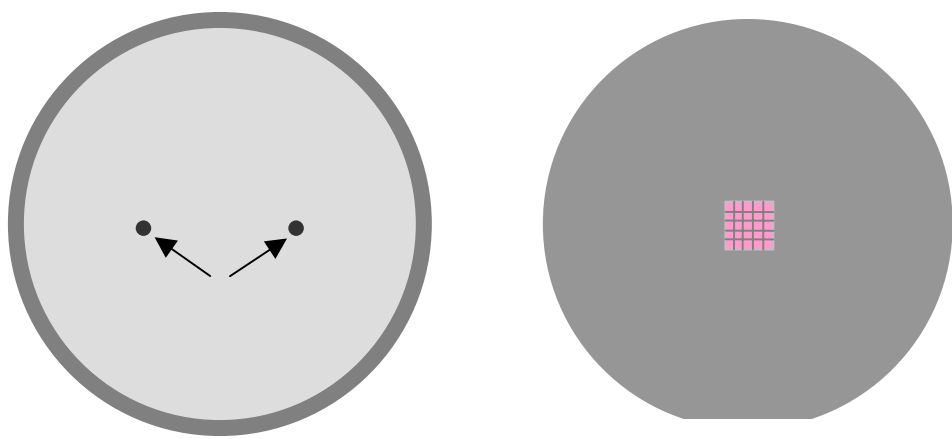
Figure 5-2 Basic steps used to pattern and expose photoresist, and liftoff process.

during steps like metal liftoff. The basic steps to perform photolithography and liftoff process for etching SiC are shown in Fig. 5-2. In the liftoff process, a thin indium-tin-oxide (ITO) layer as masking material was sputtered on photoresist patterned SiC film (see step 4). Then the ITO masking pattern was defined by a PR lift-off process.

5.4 ICP etching of SiC thin-film

5.4.1 Sample loading

As shown in Fig. 5-3, the small piece sample can not be directly put on 2" sample chuck. It was mounted on to a 2" Si supporting wafer, using Shipley 1818 photoresist. To promote the adhesion of sample, a dehydration bake was performed for 30 minutes at 120 °C.



(a) Top view of sample chuck (b) Sample adhesive to a 2" Si wafer

Figure 5-3 (a) Top view of 2" sample chuck; (b) small piece sample adhesive to a 2" Si wafer.

5.4.2 Plasma chemistries

Both Si and C form volatile etch products in either F₂-^{[1], [2], [3]} or Cl₂-based^{[4], [5]} plasma chemistries and some of the mixtures employed to date include CHF₃, CBrF₃, SF₆, CF₄ or NF₃ in the former category and Cl₂, BCl₃ and SiCl₄ in the latter. Etch rates for SiC in the range of 1500 Å/min have been reported for both ECR and ICP tools^[6] and fluorine plasma chemistries produced faster rates than either Cl₂- or Br₂-based mixtures.^[7] It is also generally found that NF₃ produced somewhat faster rates than SF₆ and much faster rates than carbon-containing fluorides.^[8]

In this study we report on the achievement of high etch rates and very clean etched surface for SiC thin-film in ICP NF₃/Ar discharges. The results about the effort on the ICP etching of SiC thin-film in Cl₂/Ar mixture have been also discussed. Electronic grade NF₃ or Cl₂ and Ar were fed into the chamber through mass flow controllers at total flow rates of 15 sccm.

5.4.3 Process parameters set-up

The initial base pressure was pumped down to 2x10⁻⁵ torr. The basic operating procedure for ICP etching is described as follows:

1. Vent the chamber: “Utilities / Vent;
2. When it shows a message as “atmospheric pressure” and “Vent Complete”, open the chamber. Then remove the ceramic clamp. Put 2" Si wafer with samples on

- the holder. Put the ceramic clamp back. Close the chamber lip;
3. Evacuate the chamber to 0 mTorr by clicking “Utilities / Pump Chamber”;
 4. Open the NF₃ or Cl₂ cylinder, adjust the delivery pressure at 14 psi;
 5. If necessary, write or edit your recipe for etching process by “Process / Edit”. All process parameters, including chamber pressure, ICP power, RF power (biasing), gas flow rate, substrate temperature, He cooling flow rate and pressure, and etch time, are edited and saved under a name of your recipe;
 6. Load etching recipe by clicking “Process / Load / Recipe Name”. Change to “Ready” mode. Then click “Run”;
 - If the helium cooling control has a problem during running, click “Hold”, it can be solved automatically.
 - After etching, the chamber will be evacuated and purged with N₂ alternatively for 3 times.
 7. After the process finished, return to “Standby” mode, and then close the NF₃ or Cl₂ cylinder;
 8. Vent the chamber. Take the sample out;
 9. Close the chamber. Evacuate it to 0 mTorr;
 10. Evacuate the lines by selecting “Service / Maintenance / Evacuate Gas Line / Gas Name”. Exit when the flow rate is less than 0.5 sccm.
 11. Load recipe from “Process / Load / clean up”. Change to “Ready” mode, and then click “Run”.
 12. After finishing clean-up, stay at “Standby” mode.

For all experiments on ICP etching of SiC thin-films grown on Si₃N₄/Si, the chamber pressure during etching process was chosen to be 2 mTorr, while the helium cooling pressure under the sample chuck was 5 mTorr. The substrate temperature was set up to 25 °C. The ICP power and RF power ranged from 100 ~ 750 W and 40 ~ 250 W,

respectively. Depending on the selections of mask material, etching chemistries and ICP plus RF power, the etch time varied from 1 ~ 10 minutes. The etched sample surface and pattern structure were inspected by SEM, depth profilometry, and optical microscope.

5.5 Results and discussion

5.5.1 Improvement of etching yield on polished SiC thin-films

Fig. 5-4 and Fig. 5-5 reveal the improvement of etching yield on polished SiC thin-films with two different ICP/RF chuck powers. An ITO thin layer (~ 300 nm) acted

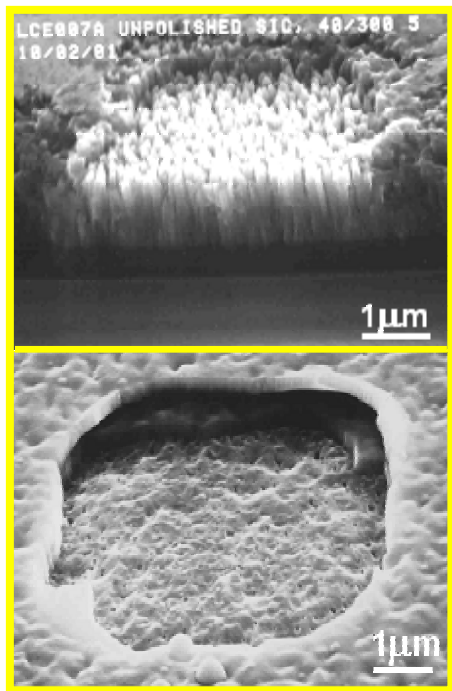


Figure 5-4. ICP etching of unpolished and polished SiC thin-films grown on $\text{Si}_3\text{N}_4/\text{Si}$ with 40 sccm 3MS at 1200 °C. ICP power / RF bias power: 300 / 40 W.

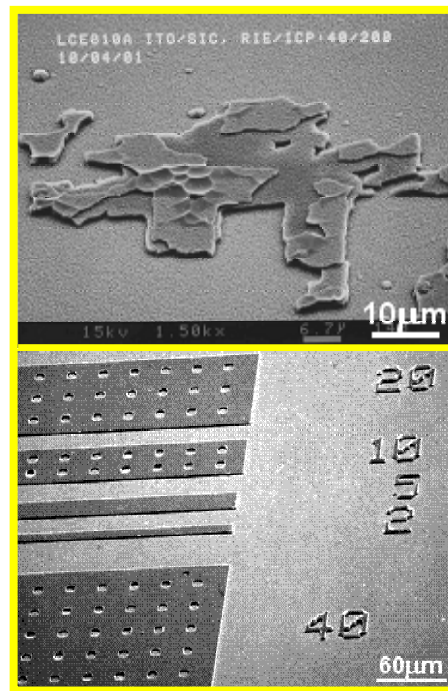


Figure 5-5. ICP etching of unpolished and polished SiC thin-films grown on $\text{Si}_3\text{N}_4/\text{Si}$ with 40 sccm 3MS at 1200 °C. ICP power / RF bias power: 200 / 40 W.

as an etching mask layer. The RMS surface roughness of polished and unpolished SiC thin-films is about 5 nm and 50 nm, respectively. Obviously, the adhesion of mask material to polished SiC thin-films is much better than that to unpolished SiC thin-films. These tell that a low surface roughness less than 10 nm with good surface morphology is highly required for a reliable bond between mask and device layers during ICP etching.

5.5.2 Effects of ICP source power, RF chuck power and NF₃ % on etch rate

Fig. 5-6 shows the effect of ICP source power on SiC etch rates in 10 sccm NF₃ and 5 sccm Ar discharges with 40W RF chuck power, 2 mTorr chamber pressure, and 25 °C substrate temperature. Here, ITO thin-film as mask layer was applied on all samples.

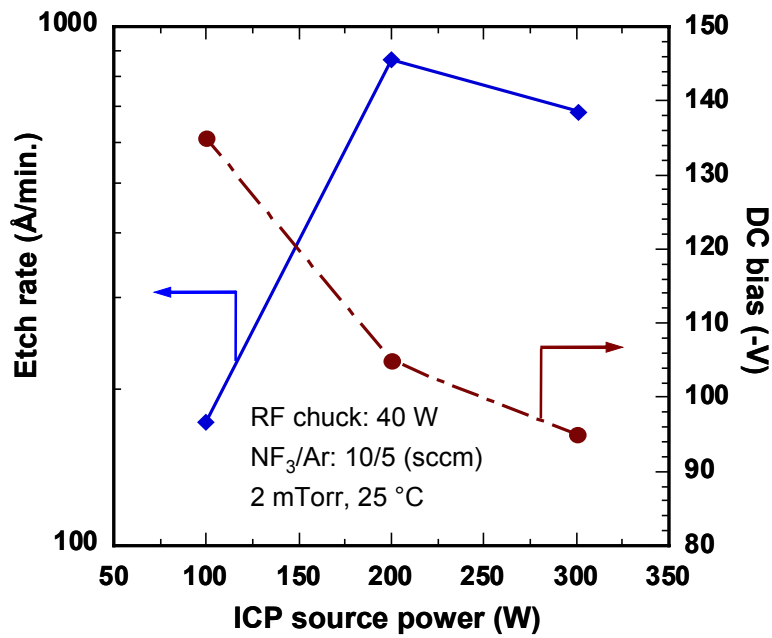


Figure 5-6. Effect of ICP source power on etch rates of SiC thin-films with total gas flow rate of 15 sccm, while SiC thin-films were grown on Si₃N₄/Si with 40 sccm 3MS at 1200 °C.

One would expect the etch rates to increase initially as source power was increased due to the higher ion flux and dissociation of the NF_3 , but as the conductivity of the discharge increases the DC chuck self-bias incident ion energy is also reduced. The tradeoff of these two effects, i.e.

increasing ion flux and reactive neutral concentration versus reduced ion energy, leads to the observed trends in the data in the figure.

Moreover, the effect of ICP power on surface morphology of the etched SiC films was examined by SEM shown in Fig. 5-7. The smoothest surface morphology was given by the lowest etch rate ($\sim 175\text{\AA}/\text{min}$) in 100W ICP discharge, while

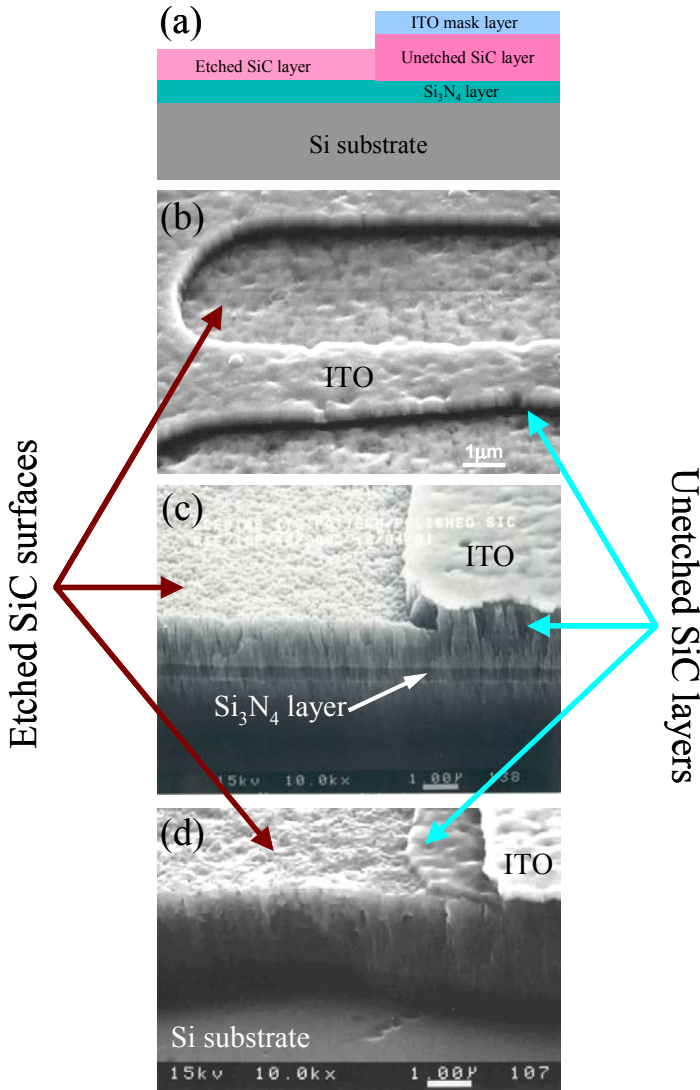


Figure 5-7 (a) Schematic of ICP etched $\text{SiC}/\text{Si}_3\text{N}_4/\text{Si}$ structure with ITO mask layer, and SEM micrographs of the etched SiC patterns in $10\text{NF}_3/5\text{Ar}$, 2 mTorr, 25 $^{\circ}\text{C}$ substrate temperature, 40W RF chuck power and (b) 100W, (c) 200W, (d) 300W ICP power discharges.

the roughest one was yielded from the highest etch rate ($\sim 865\text{ \AA/min}$) in 200W ICP discharge. These results indicate that higher ion energy produces heavier ion bombardment, which makes etched surface rougher.

Fig. 5-8 shows the influence of RF chuck power on SiC etch rates at fixed ICP source power (400W). The SiC films used were grown with 30 sccm 3MS at 1100 °C.

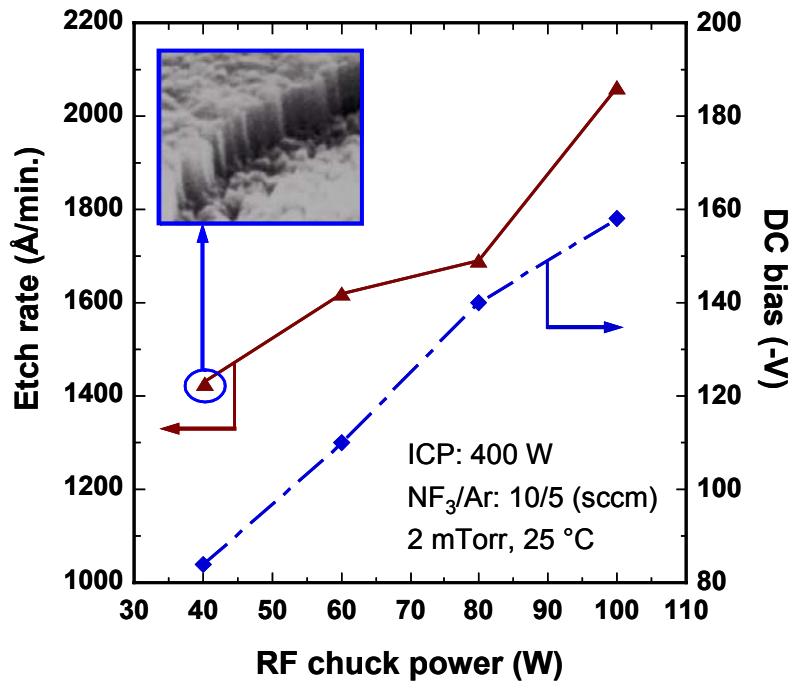


Figure 5-8 Etch rates of SiC as a function of RF chuck power in 10NF₃/5Ar, 2 mTorr, 25 °C substrate temperature, and 400 W ICP source power discharges.

For SiC there is a monotonic increase in etch rate with bias, which again emphasizes the strong role of ion energy in the etching mechanism. The average ion energy is the sum of the DC self-bias voltage and plasma potential (roughly ~ 20 V in this tool). As shown in

the inset picture in Fig. 5-8, vertical side-wall can be achieved at only 40 W RF chuck power. For 100 W RF chuck power, the etch rate reaches \sim 2100 Å/min maximum value.

The effect of NF_3 percentage in NF_3/Ar on SiC removal rates is shown in Fig. 5-9, for fixed ICP source power of 400 W, RF chuck power of 40 W, and chamber pressure at 2 mTorr. The SiC films etched were also grown with 30 sccm 3MS at 1100 °C.

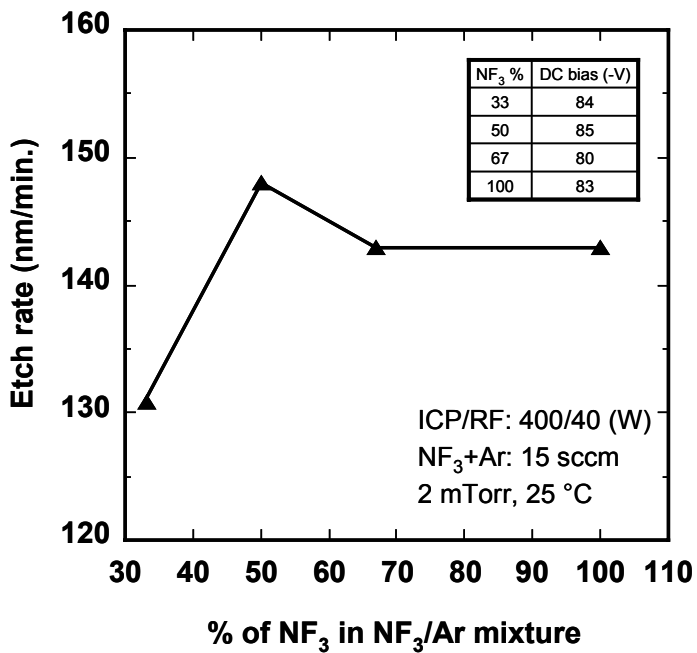


Figure 5-9 Effect of NF_3 % in NF_3/Ar on SiC removal rates.

Increasing the NF_3 percentage from 33 to 50% results in an increase in the etch rates of SiC films. This increase is mainly due to the more etchant species introduced into the chamber, which results in an increase of F atomic concentration, leading to a higher chemical reaction rate at the sample surface. Further increase of NF_3 % does not result in significant difference in etch rate, suggesting that the ion density and F atomic

concentration remain approximately constant for 400 W ICP source power and 40 W RF chuck power. The DC self-bias also stays relatively constant with plasma composition. This result indicates that F atomic concentration, not ion energy, controls etch rate under these conditions.

As compared to the etching of 6H-SiC bulk material in 10NF₃/5Ar discharges under similar conditions in the same Plasma-Therm 790 system,^[6] the ICP and RF chuck powers for etching our SiC films are about 50% lower than that for 6H-SiC substrate, but the etch rates in both cases are close to each other. This is due to the probable lower crystalline quality and bond strength of the SiC films relative to the SiC substrate.

5.5.3 Possibility to directly use photoresist as mask material

The ability to directly use photoresist as mask can simplify the patterning process, compared to the use of ITO or other metal materials such as Al or Ni, which require liftoff process. In 1996 G. McDaniel *et al.* reported the direct use of either AZ5209E photoresist or PMMA as mask material for the etching of 6H-SiC bulk materials in an Astex 4400 ECR system.^[4] Later J. J. Wang *et al.* reported again the use of AZ5209E photoresist as mask for the etching of 6H-SiC bulk materials in a Plama-Therm 790 ICP system.^{[6], [9]} However, the selectivity was very low under the conditions of 250W RF chuck power and 1000 ~ 1500 W ICP source power that are required for the etching of SiC substrate. In this study, since we can use very low RF/ICP power (40/100 W) to etch our SiC thin-films, it is possible to obtain a reasonable etch selectivity using photoresist

as mask material for the ICP etching our SiC thin-films, it is possible to obtain a reasonable etch selectivity using photoresist as mask material for the ICP etching.

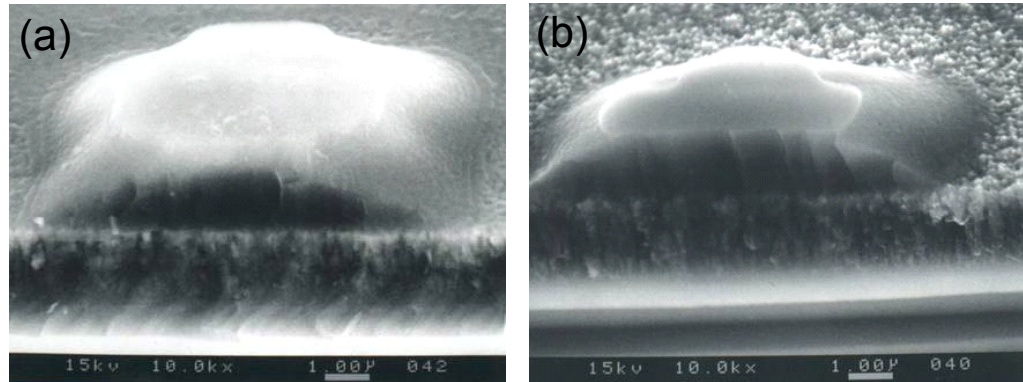


Figure 5-10 SEM micrographs (tilt 60°) of PR 1818 patterns on (a) polished SiC and (b) unpolished SiC films before ICP etching.

Shipley positive photoresist 1818 (PR 1818), one of the cheapest mask materials, has been evaluated as a possible mask for etch of the SiC films under the low RF/ICP power conditions. The total gas flow rate was 15 sccm ($10\text{NF}_3/5\text{Ar}$), while the operating pressure was kept constant at 2 mTorr and the substrate temperature was set to 25 °C. Fig. 5-10 shows a PR pattern on the polished and unpolished SiC films grown with 40 sccm 3MS at 1200 °C before etching. Due

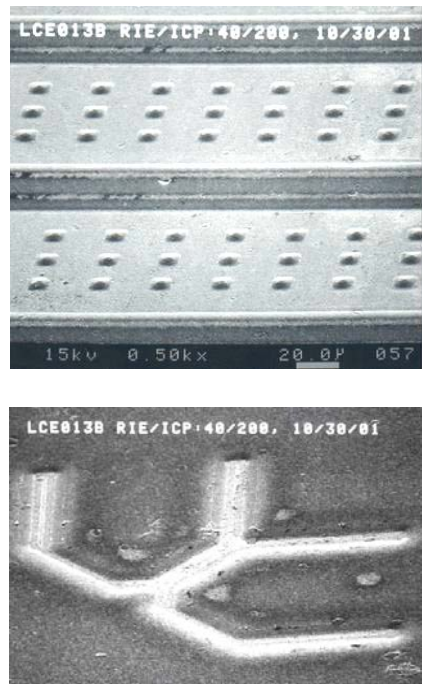


Figure 5-11. SEM micrographs of SiC etched patterns after stripping off PR.

the restriction in the lithography process, a large edge slope was made with about 30 ° angle to the interface of PR-SiC film. Thickness of the PR layer in central pattern area is about 1.8 μm .

Fig. 5-11 shows our first results on using PR 1818 as mask material for the etch of polished SiC in 40W RF chuck power, 107 –V DC self-bias and 200W ICP power discharge for 10 minutes. The etched SiC patterns were obtained after stripping off the photoresist. Although the patterns remain the large edge slope due to the low resolution of photolithography, it is promising to use PR1818 as the mask for SiC ICP etching under the low-power conditions. In the mean time, there was no etched pattern found from the unpolished SiC samples, indicating that the adhesion of PR layer to the unpolished (rough) sample surface was very poor.

5.5.4 Initial efforts on SiC etching in ICP Cl₂/Ar discharges

The possibility to directly use photoresist as mask material enables the investigation on SiC etching in ICP Cl₂/Ar discharges. The purpose to use Cl₂/Ar gas mixture is to find an alternative etchant for SiC etching with low damage. Usually, chloride or Cl[–] ions will not etch PR1818 chemically, but can have a chemical reaction with ITO and etch it away very fast. On the other hand, the lower electrical negativity of chlorine than that of fluorine will result in lower etch rate of the SiC film in Cl₂/Ar compared to NF₃/Ar under same etching conditions. To get the similar etch rate, we first etched PR-patterned SiC film (grown with 40 sccm 3MS at 1200 °C) in 20Cl₂/5Ar, 6

mTorr, 25 °C substrate temperature, 100W RF chuck power, -181V DC self-bias and 500W ICP source power discharge. The initial etched result is shown in Fig. 5-12. An etch rate of ~ 1480 Å/min was obtained under this condition. The overall etched surface is very smooth. The surface morphology is much better than all samples etched in 10NF₃/5Ar discharges. There are some small spikes on the etched surface, suggesting that an optimization on etching process is required for better results. However, the result shows a promise of using Cl₂/Ar with low RF/ICP power for dry etch of the SiC films for MEMS applications.

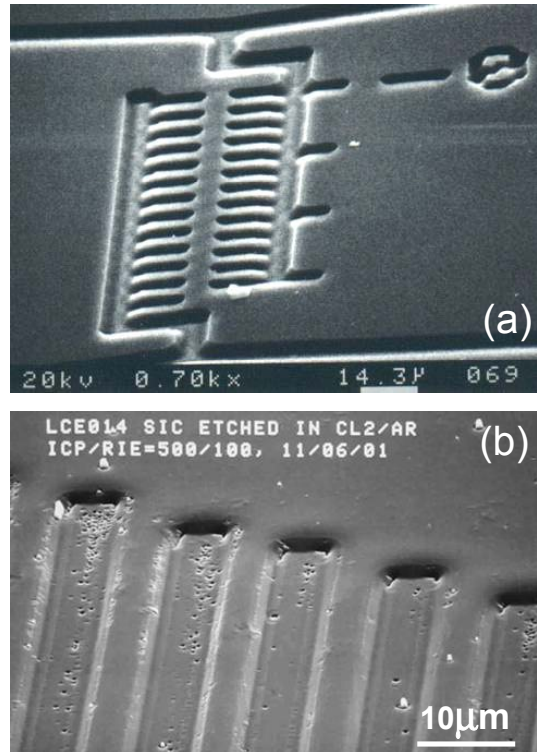


Figure 5-12. SEM micrographs of (a) PR patterns on SiC film before ICP etch and (b) etched SiC patterns in 20Cl₂/5Ar, 100/500 W RF/ICP powers discharges after stripping off PR1818.

5.6 Conclusion

Initial fabrication of MEMS structures by inductively coupled plasma (ICP) dry etching (Fig. 5-13) has shown that LPCVD conformal growth of SiC on low-stress

amorphous Si_3N_4 layer is successful. A physically polishing process has been developed to improve the SiC surface morphology for better etching yield. Under the low RF/ICP power conditions, NF_3/Ar gaseous mixture was utilized to produce smooth surfaces that are free of hydrogen passivation effects. The vertical side walls indicating high anisotropy of NF_3/Ar etching has been obtained under certain conditions. The dependence of etch rate on etching conditions (such as gases ratio, ICP power, RF chuck power and DC bias) has been studied. PR 1818 photoresist has been evaluated as a mask material for SiC etching in both NF_3/Ar and Cl_2/Ar discharges. Cl_2/Ar shows promise for ICP etching of the SiC film under certain condition. Further efforts on optimizing etching conditions are required for high etch rate with low damage.

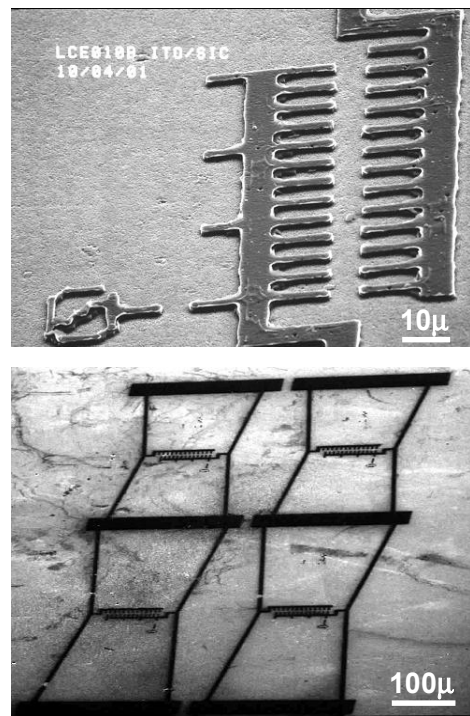


Figure 5-13 SEM micrographs of SiC surface micromachined MEMS structures: film stress diagnostic indicator gauges.

5.7 References

- [¹] J. B. Casady, E. D. Luckowski, M. Bozack, D. Sheridan, R. W. Johnson, and J. R. Williams, *J. Electron Soc.*, **143**, p. 1750 (1996)
- [²] P. H. Yih, and A. J. Steckl, *J. Electrochem Soc.*, **142**, p. 312 (1995)
- [³] J. R. Flemish, and K. Xie, *J. Electrochem. Soc.*, **143**, p. 2620 (1996)
- [⁴] G. F. McDaniel, J. W. Lee, E. S. Lambers, S. J. Pearton, P. H. Holloway, F. Ren, J. M. Grow, M. Bhaskaran, and R. G. Wilson, *J. Vac. Sci. Technol. A*, **14**, p. 885 (1997)
- [⁵] E. Niemann, A. Boos, and D. Leidich, *Inst. Phys. Conf. Ser.*, **137**, p. 695 (1994)
- [⁶] J. J. Wang, E. S. Lambers, S. J. Pearton, M. Ostling, C.-M. Zetterling, J. M. Grow, and F. Ren, *Solid-State Electron.*, Vol. 42, No. 5, pp. 743-747 (1998)
- [⁷] F. Ren, J. M. Grow, M. Bhaskaran, J. W. Lee, C. B. Vartuli, J. R. Lothian, and J. R. Flemish, *Mater. Res. Soc. Symp. Proc.*, **421**, p. 251 (1996)
- [⁸] J. B. Casady, in *Processing of Wide Bandgap Semiconductors*, ed. S. J. Pearton. Noyes Publications, Park Ridge, NJ. (1997)
- [⁹] J. J. Wang, E. S. Lambers, S. J. Pearton, M. Ostling, C.-M. Zetterling, J. M. Grow, F. Ren, and R. J. Shul, *Solid-State Electron.*, Vol. 42, No. 12, pp. 2283-2288 (1998)

CHAPTER 6. SiC THIN-FILM FABRY-PEROT

INTERFEROMETER FOR FIBER-OPTIC TEMPERATURE

SENSOR

6.1 Introduction

6.1.1 Motivation — Fiber-optic temperature sensors for flight control technologies

Efficient, high speed, all-optic systems, which utilize photons rather than electrons to carry information, is currently an important area of research.^{[1], [2]} Photons have several advantages over electrons, i.e. they have a higher information-carrying capacity, do not lose energy as quickly as electrons, and can pass near one another without generating cross talk. Optical circuits have a strong potential not only to significantly reduce weight, volume, and cost reduction but they also are highly immune to electromagnetic interference (EMI), which is particularly critical for the operation of the aircraft control systems. Even tiny amounts of radiation from the electronic devices inside the civil plane can leak through cabin windows to antennae on the outside of the airplane, interfering with its operating systems.

Two important advanced flight control technologies are currently being pursued: fiber optic control signaling Fly-By-Light (FBL) and electric actuation Power-By-Wire (PBW). Both these technologies are key to achieving the flight control technology effort objectives of reduced control system weight and reduced development cost and time for

the National Fixed Wing Vehicle (FWV) Technology Program. The FBL technology is the replacement of electronic data transmission, mechanical control linkages, and electronic sensors with optical components and subsystems. Installing lightweight, highly reliable, highly electromagnetically immune fiber optic control components on the aircraft will lower initial acquisition and direct operating costs, reduce weight, and increase aircraft performance and reliability.^{[3], [4]} However, the state-of-the-art FBL systems do not take full advantage of the photonics technologies. A true FBL/PBW system will require a simple lightweight interface where an optical signal provides the control and feedback signals to the vehicle management system computer (VMSC) box. The technology gap lies in the area of optically controlled motors and actuators as well as optically triggered distributed passive sensors, which could be connected via a single optical bus. The replacement of conventional sensors that provide absolute measurements of the external physical parameters for flight control systems by fiber-optic devices is one of the major directions in the development of second-generation fly-by-light technologies. An additional challenge is operation of such fiber-optic networks in harsh aircraft environments, where such conditions as high temperature, vibration, multi-stress, EMI, etc. set certain requirements for the materials used. For example for the motor failure monitoring, temperature sensors have to be placed on the bearings housing, where they are exposed to vibration and temperature 100% of the motor operation time. Or, in design and testing of gas turbine engines, real-time data about such physical variables as temperature, pressure, and acoustics are of critical importance. The high temperature environment experienced in the engines makes conventional electronic sensors merely difficult to apply. This study addresses the need for the fabrication of second-generation

fiber-optic temperature sensors for the use in the flight control systems in harsh environments.

6.1.2 Polycrystalline SiC for fiber-optic applications

In harsh environments, such as temperature sensing in jet turbine engines and compressors, high temperature, robust materials are required.^[5] SiC is well known as a wide bandgap semiconductor with superior thermal, mechanical, electrical, and chemical properties for the applications at high temperature in harsh environments. Current research mostly focuses on electrical devices using single-crystal SiC. However, the high cost of high quality single-crystal SiC is still an obstacle to commercialization. This has encouraged some investigation^{[6], [7], [8]} of lower cost polycrystalline SiC films for various device applications. Furthermore, device operation at high temperature also requires stable and reliable electrical contacts. Another approach for high temperature operation is to use fiber-optic technology in order to remove the need for electrical contacts. It is more economical to grow poly-SiC at much lower processing temperature on insulating substrates than to grow single-crystal SiC by using conventional chemical vapor deposition (CVD) technology. Finally, compared to Si-based devices, devices based on poly-SiC can operate at higher temperatures with better thermal, mechanical and chemical properties. Therefore, the ability to use electrically passive poly-SiC devices would be ideal for low-cost, robust, high temperature applications.

A fiber-optic, spectrum-modulating temperature sensor was for the first time

implemented on polycrystalline SiC in Nanoelectronics Laboratory at the Department of Electrical and Computer Engineering and Computer Science of University of Cincinnati in 2002.^[9] The details on the fabrication and characterization of poly-SiC Fabry-Perot interferometer for fiber-optic temperature sensor will be illustrated in the following sections.

6.2 Preliminary design of Fabry-Perot temperature sensor

6.2.1 Experimental approach

A schematic of the experimental approach is shown in Fig. 6-1. High-quality polycrystalline SiC films are grown by inexpensive low-pressure chemical vapor deposition (LPCVD) technique at relatively low temperatures on transparent substrates. Top and bottom surfaces of such a SiC film will serve as reflecting interfaces, or mirrors,

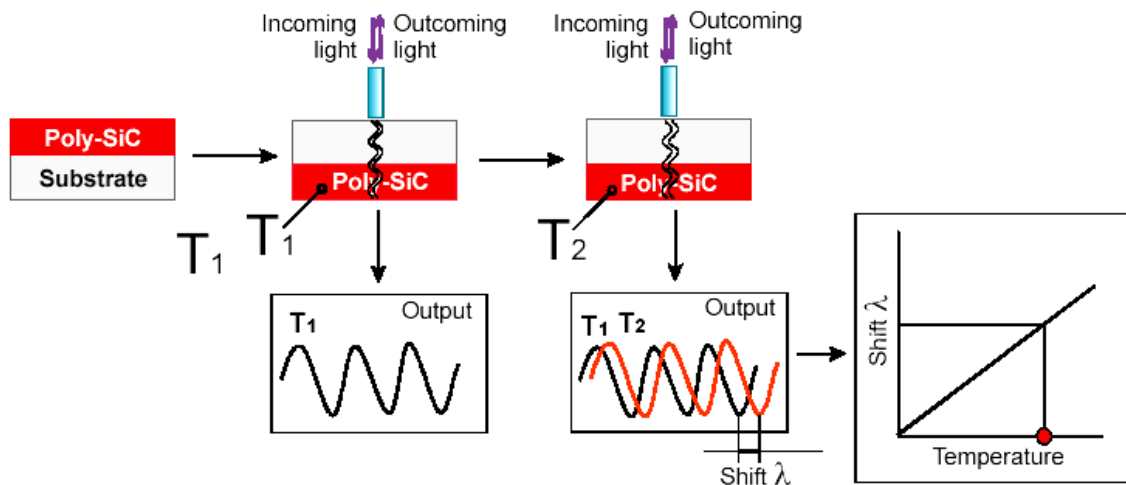


Figure 6-1 A schematic of the experimental approach.

of a Fabry-Perot interferometer, with SiC as a cavity medium. Any external physical parameter that can affect the optical properties of the SiC medium will cause changes in the light propagation inside the film. An optical signal entering such a thin-film SiC Fabry-Perot interferometer is extremely sensitive to the perturbations that affect the optical path length between the two mirrors. Therefore, measuring changes in the parameters of reflected light will provide measurement of the external physical parameter affecting the optical signal. A more detailed description of the principle of operation of a Fabry-Perot interferometer as well as an estimate of the sensor's temperature sensitivity are given in the following section.

6.2.2 Principle of operation of a Fabry-Perot fiber-optic temperature sensor and its temperature sensitivity

A thin-film Fabry-Perot interferometer shown in Fig. 6-2 is one type of spectrum-modulating transducer that can be used to sense a number of different physical parameters.^[10] The separation between the thin film boundaries, L, is of the order of magnitude of the wavelength so that interference effects occur.^[11] During operation, the sensor must incorporate some mechanism which causes the interferometer's optical path difference (OPD) to be a stable and sensitive function of only the parameter to be measured. For phase-modulated sensors, if the sensor is illuminated by a broadband light source, the positions of the maxima and minima of the sensor's output spectrum can be used to determine the magnitude of the sensed parameter. The information content of this type of spectrally encoded signal is unlikely to be degraded by routine variations in the

transmission properties of the fiber link. Besides providing a high degree of link-independence, Fabry-Perot type sensors can be compact and rugged, and they can provide both high sensitivity and stability.^[12]

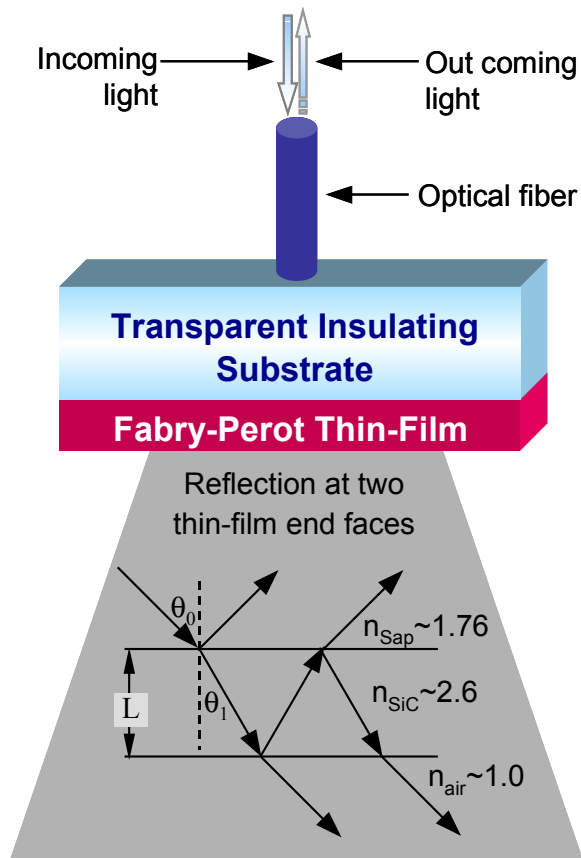


Figure 6-2. A schematic of the thin-film Fabry-Perot interferometer used for the temperature measurement.

An interferometer's spectral transfer function, as a function of wavelength λ , contains a number of periodically spaced minima and maxima positions which are determined by the interferometer's OPD expressed in the following term:

$$OPD = 2n(\lambda, T) \cdot L \cdot \cos\theta_i \quad (1)$$

where $n(\lambda, T)$, L , and θ_i represent the refractive index of the interferometric medium, film thickness, and incident angle of light, respectively. For normal incidence, the one-way phase shift, Φ , of the output spectrum is defined as: [10], [11], [12], [13], [14], [15]

$$\Phi = \frac{\pi \cdot OPD}{\lambda} \quad (2a)$$

or

$$\Phi = \frac{2\pi \cdot n(\lambda, T) \cdot L}{\lambda} \quad (2b)$$

where $\theta_i \approx 0$ and $\cos\theta_i \approx 1$. Since Φ is independent on λ , assuming the film thickness L unrelated to λ , taking a differential with respect to λ on equation (2b) gives:

$$\frac{\Delta\Phi}{\Delta\lambda} = 0 = 2\pi \cdot L \cdot \left(\frac{\Delta n}{\lambda} - \frac{\Delta\lambda}{\lambda^2} \right) \quad (3)$$

Dividing eq. (3) by ΔT yields:

$$\frac{\Delta n}{\Delta T} = \frac{1}{\lambda} \cdot \frac{\Delta\lambda}{\Delta T} \quad (4)$$

The temperature sensitivity is defined as: [13], [16]

$$\frac{\Delta\Phi}{\Delta T} = \frac{2\pi \cdot n \cdot L}{\lambda} \cdot \kappa_\Phi \quad (5)$$

and

$$\kappa_\Phi = \kappa_n + \kappa_L \quad (6a)$$

$$\kappa_n = \frac{1}{n} \cdot \frac{\Delta n}{\Delta T} \quad (6b)$$

$$\kappa_L = \frac{1}{L} \cdot \frac{\Delta L}{\Delta T} \quad (6c)$$

where κ_n and κ_L are the thermo-optic coefficient and thermal-expansion coefficient, respectively. Substitution of equations (6b) and (6c) into equation (5) gives:

$$\frac{\Delta\Phi}{\Delta T} = \frac{2\pi \cdot n \cdot L}{\lambda} \cdot \left(\frac{1}{n} \cdot \frac{\Delta n}{\Delta T} + \frac{1}{L} \cdot \frac{\Delta L}{\Delta T} \right) \quad (7)$$

Assuming $\kappa_n \gg \kappa_L$, we have:

$$\frac{\Delta\Phi}{\Delta T} \approx \frac{2\pi \cdot L}{\lambda} \cdot \frac{\Delta n}{\Delta T} \quad (8)$$

Combining equation (4) and (8) yields:

$$\frac{\Delta\Phi}{\Delta T} \approx \frac{2\pi \cdot L}{\lambda} \cdot \left(\frac{1}{\lambda} \cdot \frac{\Delta\lambda}{\Delta T} \right) \quad (9)$$

Assuming that the temperature is determined as a function of one of the resonant wavelengths (λ_m), equation (9) becomes:

$$\frac{\Delta\Phi}{\Delta T} \approx \frac{2\pi \cdot L}{\lambda_m(T_0)} \cdot \left[\frac{1}{\lambda_m(T_0)} \cdot \frac{\Delta\lambda_m}{\Delta T} \right] \quad (10)$$

where T_0 is arbitrarily defined. The relative temperature sensitivity, κ_s , can then be approximated by:

$$\kappa_s = \frac{1}{\lambda_m(T_0)} \cdot \frac{\Delta\lambda_m}{\Delta T} \approx \kappa_\Phi \quad (11)$$

This definition is fundamental and critical to the following discussion on the results of temperature sensing measurement.

Based on eq. (2b), the following derivations explain the effects of film thickness and spectral range on the interference pattern of Fabry-Perot interferometers. The phase difference, $\Delta\Phi(\lambda_1, \lambda_2)$, between two adjacent minima at wavelength λ_1 and λ_2 can be expressed:

$$\Delta\Phi(\lambda_1, \lambda_2) = \frac{2\pi(\lambda_1 - \lambda_2) \cdot n(\lambda, T) \cdot L}{\lambda_1 \cdot \lambda_2} \quad (12a)$$

or

$$\Delta\lambda = \frac{\lambda_1 \cdot \lambda_2}{2\pi \cdot n \cdot L} \cdot \Delta\Phi(\lambda_1, \lambda_2) \quad (12b)$$

where $\Delta\Phi(\lambda_1, \lambda_2)=2\pi$ for two adjacent minima. The wavelength difference, $\Delta\lambda_m$, at two adjacent minima was then obtained:

$$\Delta\lambda_m = \frac{\lambda_1 \cdot \lambda_2}{n \cdot L} \quad (13)$$

Eq. (13) indicates that thicker films give narrower spacing between two adjacent minima, and that the spacing increases with wavelength. These effects will be shown in the following results.

6.3 Substrate selection

For the operation of the poly-SiC thin-film interferometer at high temperature, proper consideration of the substrate is required. First, the selected substrate should be suitable for growth of poly-SiC thin-films by CVD, which means less thermal mismatch and smooth SiC-substrate interface. Second, its thermal, mechanical, and chemical properties should be reliable and stable at high temperature. Third, the substrate should be optically transparent to the light source used for the temperature sensing measurements. Fourth, because the temperature sensor is required to be immune to electromagnetic interference, the substrate should be electrically insulating in order to eliminate any electrical side effect on the sensor performance. Based on the above considerations, as shown in Table 1-2, single crystalline sapphire substrate appears to be

the best candidate because it is not only perfectly suited for poly-SiC growth and is transparent to a broad wavelength spectrum but also possesses excellent thermal, mechanical, and chemical properties, which is essential for the device operation in harsh environments. In addition, its availability as large diameter and high quality substrates is a good match for batch processing. In this section, we report on poly-SiC thin-films grown on sapphire substrates and on the fabrication of a Fabry-Perot interferometer for fiber-optic temperature sensor, which can operate at temperature up to 540 °C.

6.4 Growth of SiC thin-film on insulating sapphire substrate

The poly-SiC films were grown in an LPCVD system. The details of the system can be found elsewhere.^[17] The condition of the reaction chamber and information on carrier and precursor gases were previously described.^[7] In order to reduce contamination during the SiC growth, the starting sapphire substrate was initially cleaned with acetone, methanol, and de-ionized water, successively, before introducing in the chamber. Then, an in-situ clean was performed with 1 slm H₂ at 1100 °C for 30 seconds prior to each SiC growth run. For all SiC growth runs reported, the hydrogen flow rate was 1 slm, while the trimethylsilane [(CH₃)₃SiH or 3MS] flow rate ranged from 25 to 45 sccm. The SiC growth temperature was fixed at 1100 °C. The growth duration was varied from 2 to 16 minutes, and temperature ramping rate was set to 25 °C/sec. An optical pyrometer was used to monitor and control the processing temperature.

The crystal structure of the poly-SiC film was characterized by x-ray diffraction (XRD). The surface morphology of the poly-SiC film and the SiC-sapphire interface were examined by scanning electron microscopy (SEM). The surface roughness and morphology of the poly-SiC film were studied by atomic force microscopy (AFM). As shown in Fig. 6-3, the as-grown poly-SiC thin-film on sapphire is typically semi-transparent to visible light and brown in color.

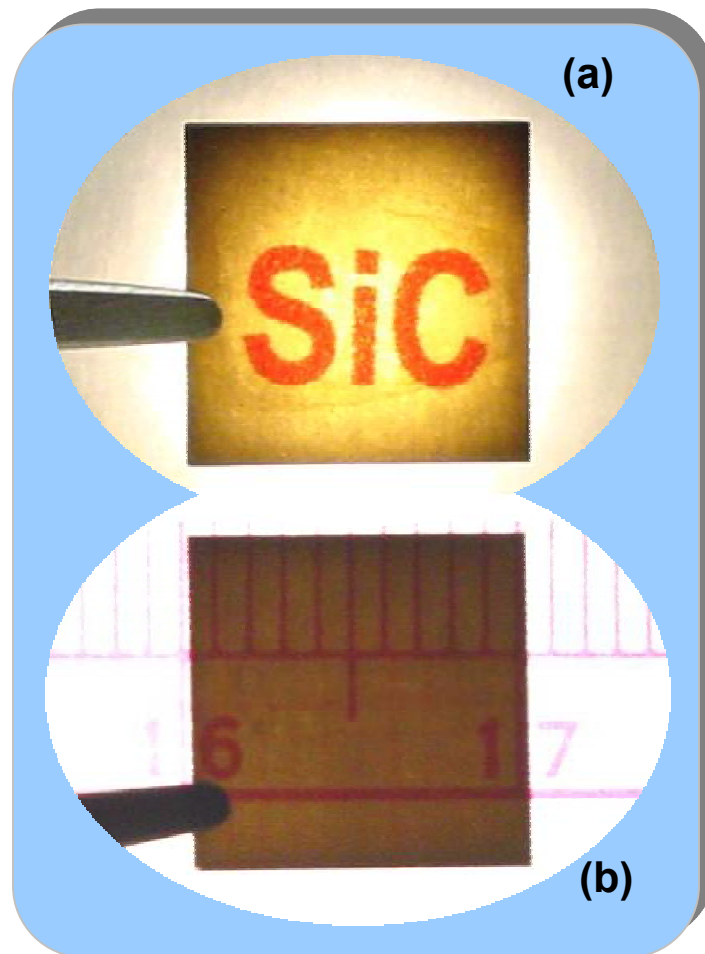


Figure 6-3. SiC thin- films grown on $1 \times 1 \text{ cm}^2$ sapphire substrate with (a) 40 sccm 3MS for 8 min. and (b) 35 sccm 3MS for 12 min. at 1100°C , which are semi-transparent to a flash light.

6.4.1 Effect of film thickness on the structural properties

To investigate the effect of film thickness on the structural properties of poly-SiC thin-films, the 3MS flow rate was fixed at 40 sccm. The film growth rate is in the range of 0.25 to 0.3 $\mu\text{m}/\text{min}$. Chemical composition and crystallinity of the SiC thin-films were obtained from their XRD spectra, as shown in Fig. 6-4. The poly-SiC thin-films grown for 8 and 5.5 minutes were 2.0 and 1.5 μm thick, respectively. They were both oriented in the 3C-SiC <111> direction with a 2θ peak at 35.5° and line widths between $0.27^\circ \sim 0.3^\circ$. The film grown for 2 minutes did not exhibit an obvious 3C-SiC <111>

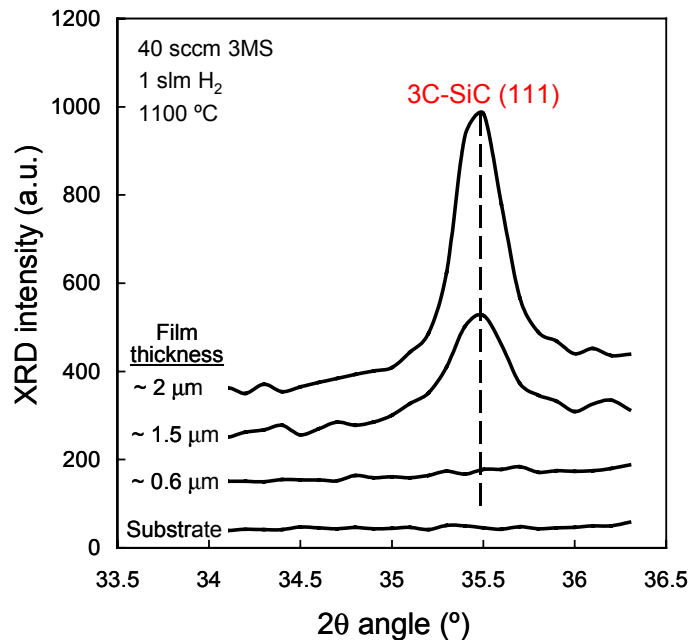


Figure 6-4 XRD spectra of starting sapphire substrate and SiC films grown at 1100 $^\circ\text{C}$.

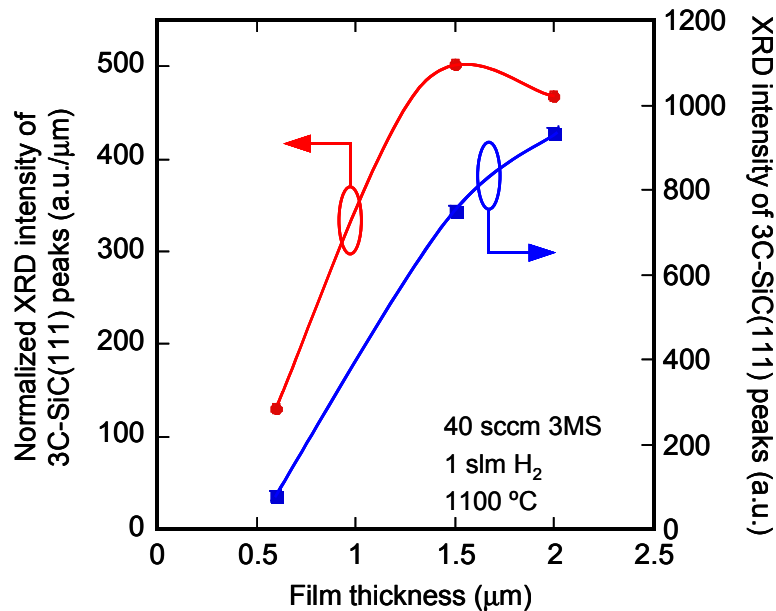


Figure 6-5 Dependence of XRD intensity and thickness-normalized XRD intensity of 3C-SiC (111) peaks on film thickness.

peak. No other crystal orientation was detected for the poly-SiC films within the XRD scan range. The XRD intensity of the SiC <111> peak is seen in Fig. 6-5 to increase monotonically with film thickness. Also shown in Fig. 6-5, the XRD intensity normalized to the film thickness first increases rapidly with film thickness and then shows saturation for the thicker films. This is mostly due to the mismatch in crystal structure and thermal expansion coefficient between the sapphire substrate and the SiC film. The disordered layer at the interface has a much stronger effect on a relatively thin film. As the film grows thicker, the strain is released and the film becomes “relaxed”, with the inter-planar distance reaching its normal bulk value.^[18] For the application of fiber-optic temperature sensor, the film thickness and structural properties, such as crystallinity and surface roughness, affect the device performance. AFM measurements showed additional details on the effect of film thickness on poly-SiC surface roughness and topology.

As a thin-film interferometer, the poly-SiC acts as a Fabry-Perot etalon, which consists of two mirrors of reflectance R_1 and R_2 separated by the poly-SiC thin-film.^[10] In order to reduce the dispersion of reflected light at the two mirrors, both end surfaces (the poly-SiC top surface and the SiC-sapphire interface) are required to be optically flat. The optical flatness of the film can be expressed quantitatively in terms of surface roughness, which is expected to be much smaller than the wavelength of the reflected light. Figs. 6-6 and 6-7 show the surface topology and root mean square (RMS) surface roughness of the starting sapphire substrate and the poly-SiC films studied by AFM. The RMS roughness varied from ~ 1 - 8.5 nm for poly-SiC films with different thickness and ~0.84 nm for the starting sapphire substrate. All measured values of the roughness are

about two orders of magnitude smaller than the wavelength in the spectral range ($490 \sim 1050$ nm) of the reflected light, in other words quite sufficient for our purpose. The poly-SiC surface morphology and SiC-sapphire interface quality were also examined by scanning electronic microscopy (SEM). The interface is smooth and free of voids, as seen in Fig. 6-8.

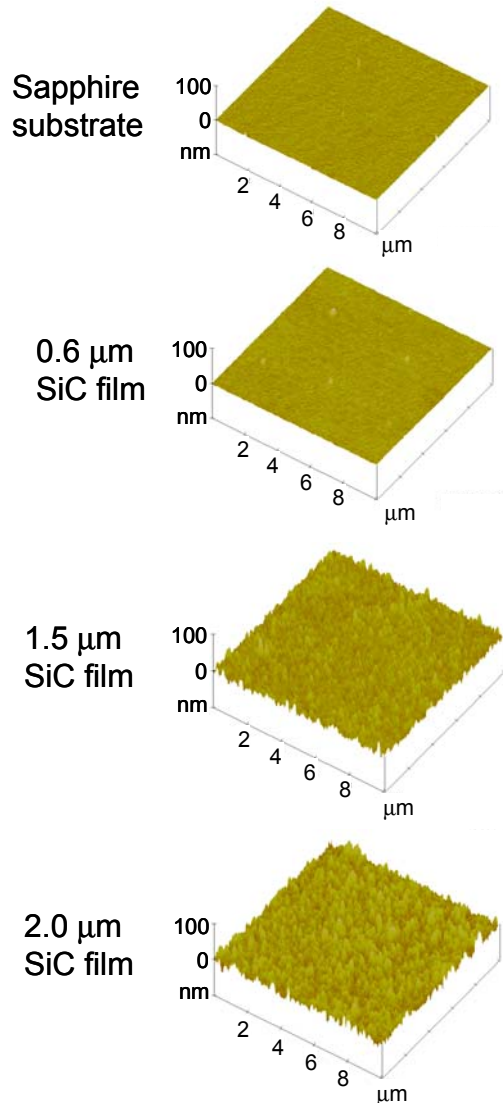


Figure 6-6 AFM micrographs of 3D surface topology of the starting sapphire substrate and of SiC films with different thickness.

According to eq. (5) in Section 6.2.2, the thicker film provides the higher temperature sensitivity. But thicker film also yields rougher surface as seen in Fig. 6-6, which can degrade the sensor performance because rougher surface scatters more reflected light at the end face, which acts as the mirror of Fabry-Perot interferometer. Therefore, we selected the 2 μm thick poly-SiC film for the temperature measurement, which will be discussed in Section 6.5.2.

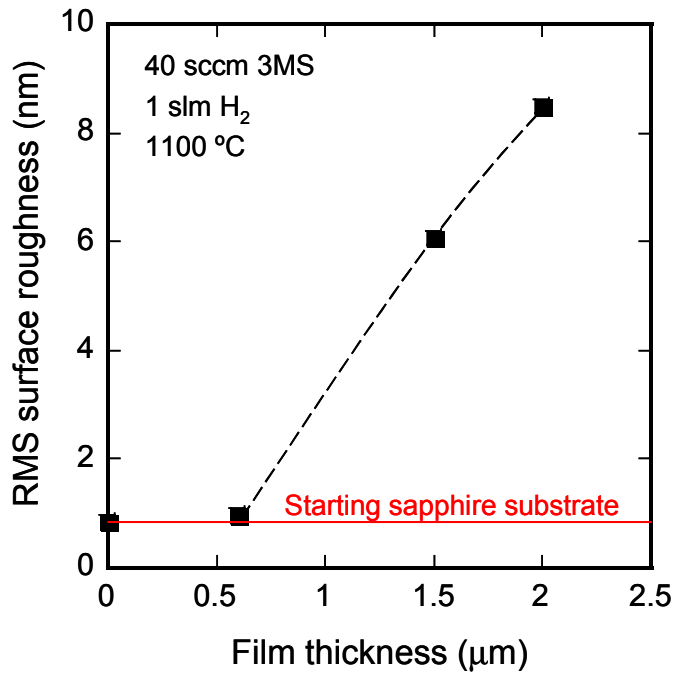


Figure 6-7. RMS surface roughness of starting sapphire substrate and SiC films vs. film thickness.

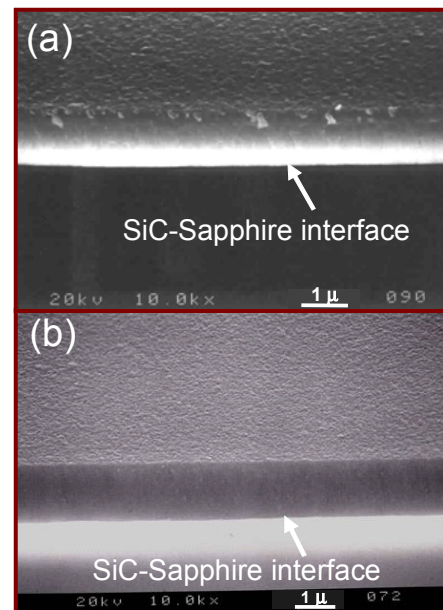


Figure 6-8 SEM micrographs of SiC films with different thickness (a) 1.5 μm ; (b) 2 μm .

6.4.2 Effect of 3MS flow rate on the structural properties

The 3MS flow rate is another key parameter to determine the structural properties of poly-SiC thin-films. Different 3MS flow rates could result in differences in film crystallinity, film density, grain size, stoichiometry, surface morphology and surface roughness, hence differences in film refractive index, optical path difference in the SiC Fabry-Perot interferometer, intensity of the light reflected at two end faces of the thin-film, as well as temperature sensing performance of the SiC sensor.

To study the effect of 3MS flow rate on the structural properties, the 3MS flow rate was varied from 25 to 45 sccm. The film growth rate ranges from 0.01 to 0.321 μm per minute for different 3MS flow rate. Based on the growth rate, the growth time was set up for getting $\sim 2 \mu\text{m}$ thick SiC film. From Fig. 6-9, the higher the flow rate of 3MS gives the higher the growth rate

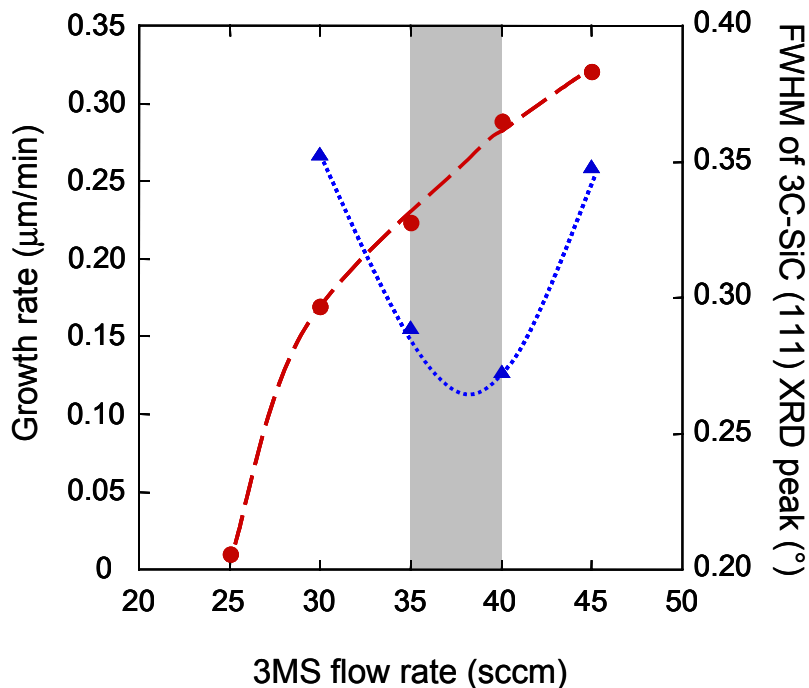


Figure 6-9 Effects of 3MS flow rate on growth rate and FWHM of 3C-SiC(111) XRD peak of SiC thin films grown on sapphire substrate at 1100 $^{\circ}\text{C}$

of SiC film. Since the growth rate for the film using 25 sccm 3MS is too low (about 0.01 $\mu\text{m}/\text{min}$. in Fig. 6-9), it is not practical to grow a 2 μm thick SiC film for ~ 200 minutes using our current LPCVD system under this growth condition.

However, the films grown with 30 to 45 sccm 3MS for 6 to 16 minutes can give enough information to show the effects of growth conditions on structural properties of the SiC films. The information of chemical composition and crystallinity of SiC thin films grown on sapphire substrate was obtained through their θ - 2θ XRD spectra, as shown in Fig. 6-10. These spectra show that poly-crystalline SiC films oriented in the 3C-SiC $<111>$ direction

with a 2θ peak at 35.5° and line widths between $0.273^\circ \sim 0.353^\circ$ were obtained at growth temperature of 1100°C . No other orientation of SiC films was detected. Unlike the one-direction relationship between growth rate and 3MS flow rate, it is interesting that the

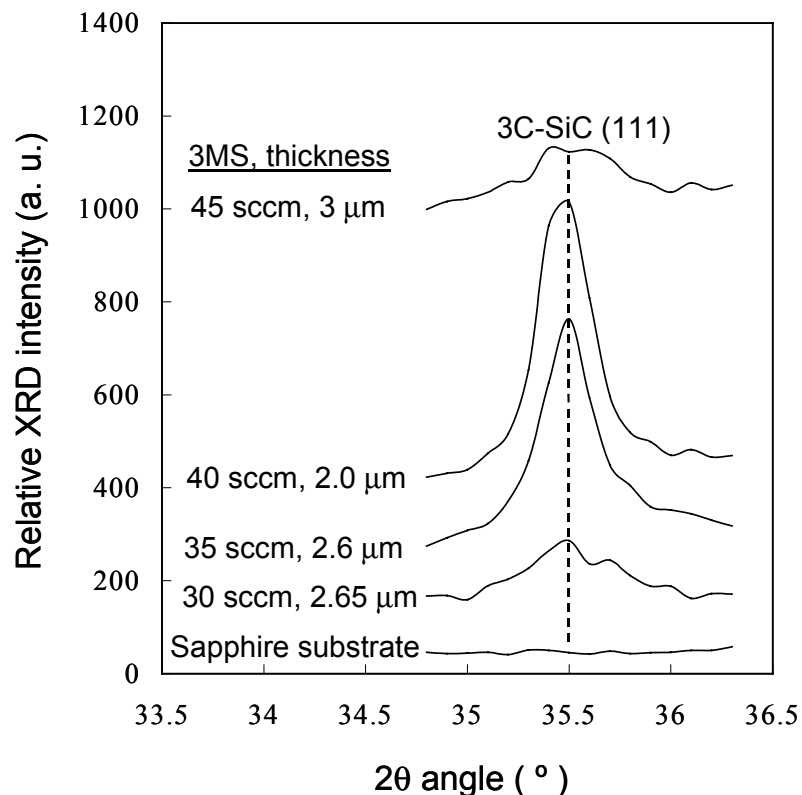


Figure 6-10 Effect of 3MS flow rate on the XRD peak intensity of 3C-SiC (111) orientation.

crystallinity of SiC films was not increased or decreased with increasing the 3MS flow rate monotonically. From the full widths at half maximum (FWHM) of SiC (111) peak vs. 3MS flow rate in Fig. 6-9, we imply that there is an optimized region for the selection of 3MS flow rate that can produce the SiC film with better crystallinity, which is in the range of 35 ~ 40 sccm. The following discussion on the SEM and AFM results could tell why this happened.

Fig. 6-11 shows the results of surface morphology, grain or column boundary, and SiC-sapphire interface measured by SEM. The interfaces of all samples grown on sapphire substrate at 1100 °C are smooth and free of void. The films grown with 40 and 35 sccm 3MS showed better surface morphology than the films grown with other 3MS flow rates.

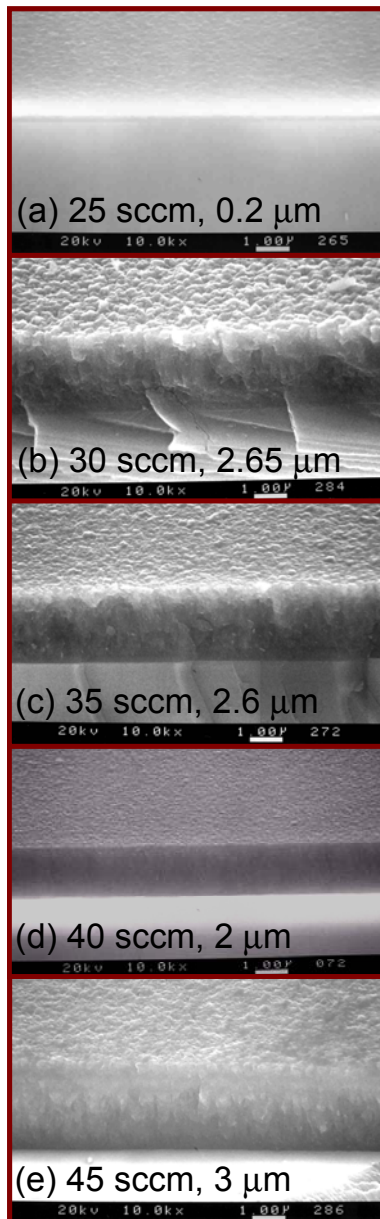


Figure 6-11. The SEM micrographs of SiC thin films grown on sapphire [0001] substrate with

- (a) 25 sccm,
- (b) 30 sccm,
- (c) 35 sccm,
- (d) 40 sccm,
- (e) 45 sccm

3MS at 1100 °C.

In Figs. 6-12 and 6-13, the root mean square (RMS) surface roughness of SiC thin films was normalized to the film thickness and varied from 4.33~5.75 nm per μm in thickness. The RMS surface roughness of starting sapphire substrate is 0.837 nm, measured by AFM. For all films with thickness of 2 to 3 μm , the RMS surface roughness will be about 2-order magnitude smaller than the spectral range (490 ~ 1050 nm) of the reflected light, sufficient for our purpose. In Fig. 6-13, the lower normalized RMS surface roughness was also given by the films grown using 40 and 35 sccm 3MS. These are consistent to the results on effect of 3MS flow rate on the line widths of SiC (111) peak in Fig. 6-9. The possible reason for such phenomenon could be explained by the different

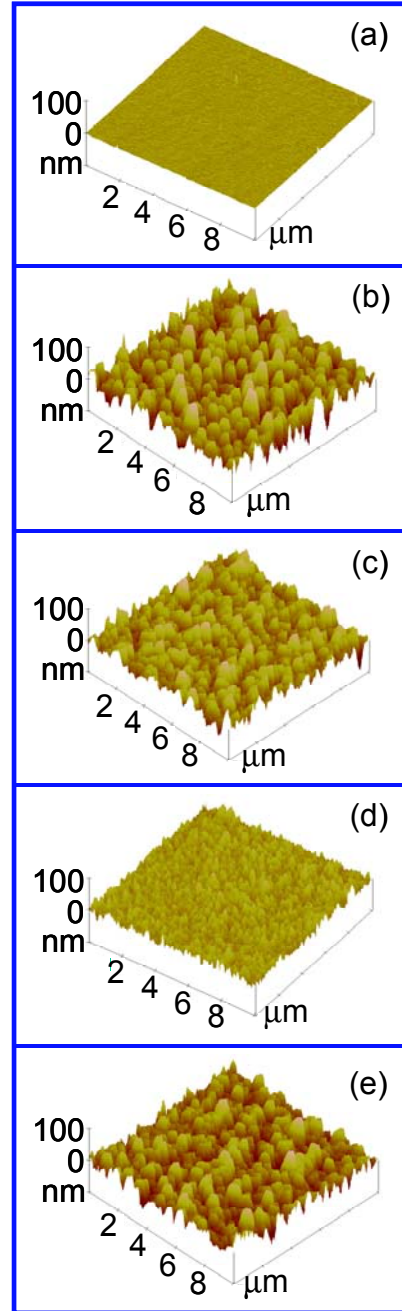


Figure 6-12 The AFM micrographs of (a) starting surface of sapphire substrate and surfaces of SiC films grown at 1100 °C with (b) 30 sccm, (c) 35 sccm, (d) 40 sccm and (e) 45 sccm 3MS for 16 min., 12 min., 8 min. and 9 min., respectively.

strain effect on the structural properties of each SiC film under different 3MS flow rate. It is well accepted that substrate temperature and deposition rate (atoms/cm²-sec) are among the chief variables affecting deposition processes.^[19] In this section, the flow rate of 3MS determined the structural properties of the SiC films. The lower 3MS flow rate results in lower growth rate and denser film. The denser film contains higher strain. When the film grows thicker, the strain in the film can be reduced due to a combination of relaxation originated from its higher surface roughness and lateral inhomogeneity in the composition of the films.^[18] On the other hand, the higher 3MS flow rate produces more void volume in the film, which makes the film surface rough and can degrade the device performance. To obtain a high temperature sensitivity of the SiC temperature sensor, the film should be thick enough while keeping low surface roughness.^[9] Therefore, the need of optically flat surfaces for SiC Fabry-Perot interferometer operation requires the growth conditions to be optimized, in order to provide a film with low surface roughness (about 10⁻²

of resonant wavelength λ_m), high crystallinity, good surface morphology, high film uniformity, and low void volume. From the next discussion on temperature sensing measurements of SiC Fabry-Perot interferometers, we will see how important

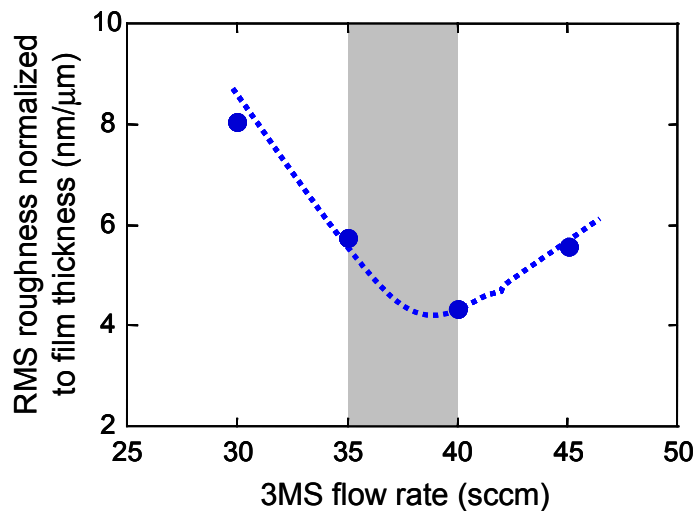


Figure 6-13 Effects of 3MS flow rate on RMS surface roughness of SiC thin films, which is normalized to the film thickness.

the optimized growth conditions are to the performance of SiC Fabry-Perot temperature sensors.

6.5 SiC temperature sensor characterization

6.5.1 Experimental set-up

As shown in Fig. 6-14, the temperature sensing measurement was performed by an Ocean Optics, Inc.'s (Florida, USA) SD2000 fiber optic spectrometer with a reflection probe designed for high temperature operation and a LS-1 white, broadband, tungsten halogen light source in the atmospheric ambient. A bundle of seven Fiberguide's (New Jersey, USA) multimode, 400- μm , gold-jacketed silica fibers, which includes six illumination fibers surrounding one read fiber in center, were designed for a bifurcated reflection probe that can operate at temperature up to 700 °C. This specially designed reflection probe has a 200 mm x 6.35 mm stainless steel ferrule to house the fiber bundle. It was coupled to the fiber optic spectrometer and the light source to create a small-footprint optical-sensing system. A BARNSTEAD/THERMOLYNE's (Iowa, USA) *Thermolyne Cimarec® 1* hot plate was used to provide heat during the temperature sensing measurement. The maximum operating temperature of this hot plate is about 550 °C with 375 watts output power. To avoid the collection of reflected light from the top surface of the hot plate, the sample was separated from the hot plate by a 1.5 cm thick metal disc ring. The reflection probe was held by a probe holder over the sample and sat on the backside of the sample in normal direction. To record the operating temperature,

the common end of an Omega® ‘s (Connecticut, USA) K type thermal couple with a temperature resolution of $0.1^{\circ}\text{C}/1^{\circ}\text{C}$ contacted end surface of the poly-SiC film. The other end of the thermal couple was then connected to an Omega®’s HH23 handheld microprocessor digital thermometer.

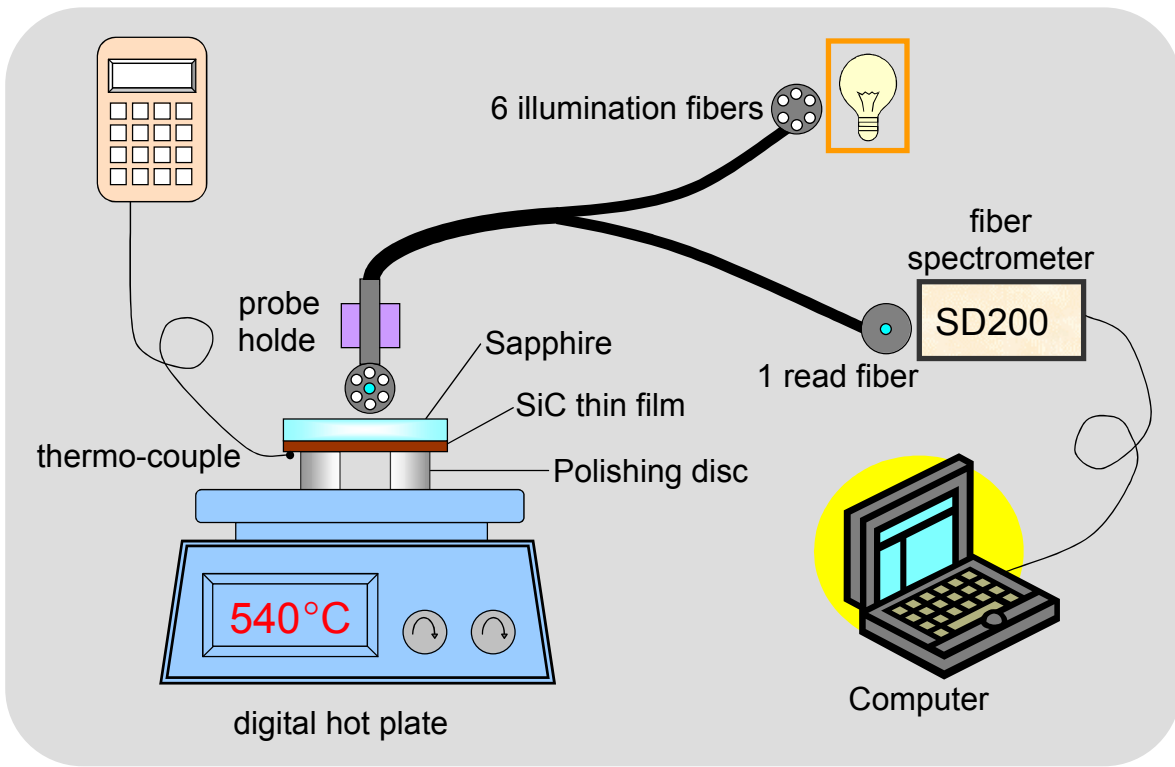


Figure 6-14 Sketch of the experimental set-up for temperature measurement.

The OPD of the reflective poly-SiC interferometer is temperature dependent due, primarily, to the variation of its refractive index with temperature, which can be translated into the change of wavelength of the resonance minimum. The sensing interferometer is illuminated by spectrally white broadband light source of a tungsten-halogen lamp. The sensed temperature can then be determined from the positions of resonance minima in the sensor’s output spectrum. Some simple algorithm and statistical

technique were used to analyze the spectrum in order to determine the temperature sensitivity of the sensor.

6.5.2 Effect of SiC thin-film thickness

For all measurements, the angle of incident light is approximated to be zero. Fig. 6-15 shows the output spectra of starting sapphire substrate and poly-SiC temperature sensors using poly-SiC thin-films grown on sapphire substrate with different thickness. The spectral range is from 490 nm to 1050 nm. The interference phenomenon was observed with all poly-SiC samples, but not with the starting sapphire substrate. The thicker poly-

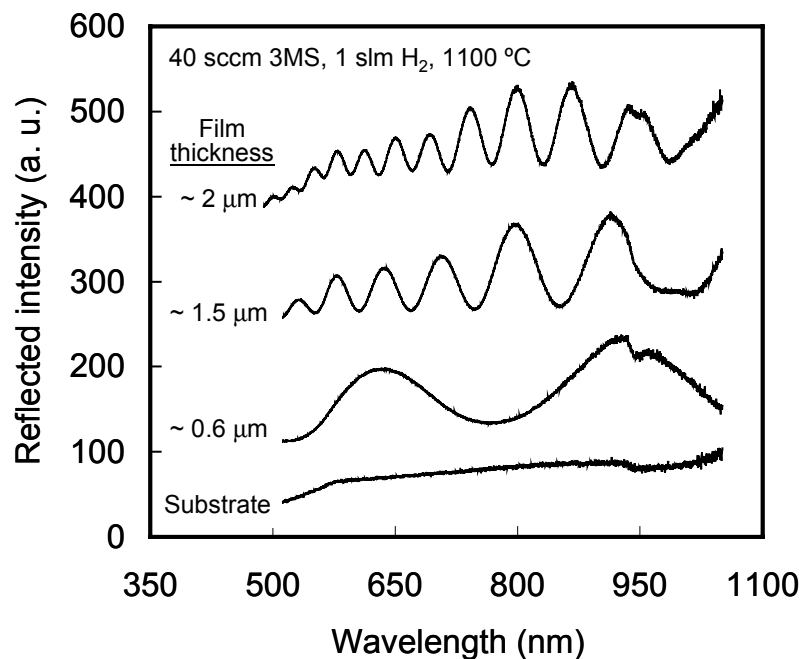


Figure 6-15 Spectra of temperature sensors using SiC thin films with different thickness over the wavelength range from 490 nm to 1050 nm.

SiC film gives sharper curvature at the positions of reflected resonance minima and shorter bandwidth between two adjacent resonance minima. Eq. (9) indicates that the thicker film should provide higher temperature sensitivity. However, in practice, there is a limitation on the film thickness due to the restriction on the RMS surface roughness for our purpose. Figs. 6-6 and 6-7 indicate that the top surface of a poly-SiC thin-film will no longer be optically flat when the film thickness exceeds a certain value. This can severely degrade the sensor performance because the rougher surface will give higher dispersion of the reflected light. Based on the above considerations, we chose the 2.0 μm thick poly-SiC film grown on sapphire substrate to make the temperature sensing measurement.

The resonant wavelengths, λ_m , of the output spectra were presumed to correspond to the local minima in the reflection $R_s(\lambda)$ function. To determine λ_m , the $R_s(\lambda)$ was measured using a sampling interval of 0.3 nm. A quadratic fit was applied to $R_s(\lambda)$ in the ± 6 nm region about the minimum value. By calculating the position of the polynomial's minimum, λ_m can then be determined. This simple algorithm was found to provide a resolution that was adequate for the purpose of calibrating the sensors and assessing their stability. As shown in Fig. 6-16, a shift of ~ 7 nm in resonance minimum was obtained for the poly-SiC temperature sensor over the temperature range of 22.2 $^{\circ}\text{C}$ to 546.5 $^{\circ}\text{C}$, where $\lambda_m \approx 692.8$ nm at T_0 of 22.2 $^{\circ}\text{C}$. In Fig. 6-17, the shift in resonance minimum, $\Delta\lambda_m$, increases with increasing the operating temperature, T_M . A linear fit to $\Delta\lambda_m/\Delta T_M$ provides the relative temperature sensitivity of $1.9 \times 10^{-5}/^{\circ}\text{C}$, using the definition of κ_s in eq. (11). From the slope of $\Delta\lambda_m/\Delta T_M \approx 0.013$ nm/ $^{\circ}\text{C}$, predicted by a linear regression in Fig. 6-17

and by applying the definition of κ_s again, we can get an approximation to convert the changes of $\Delta\lambda_m$ into the changes of measured temperature ΔT_M .

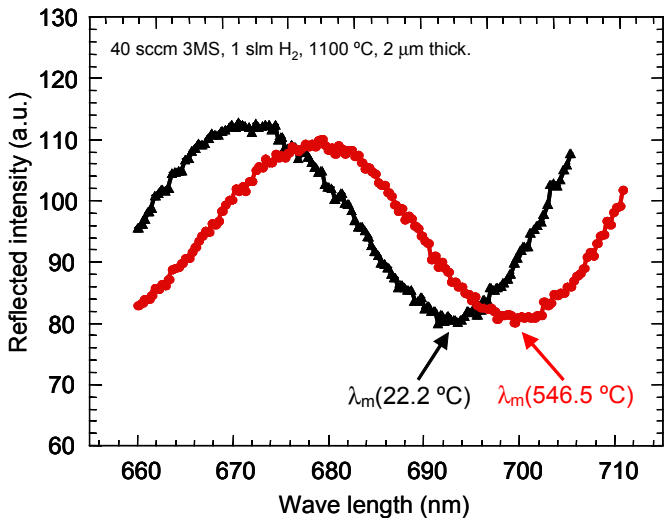


Figure 6-16. Spectra of SiC temperature sensor obtained at 22.2 °C and 546.5 °C. The shifts in resonance minima versus temperature were recorded. The $\lambda_m(T_0)$ near 692.8 nm at 22.2 °C is arbitrarily defined.

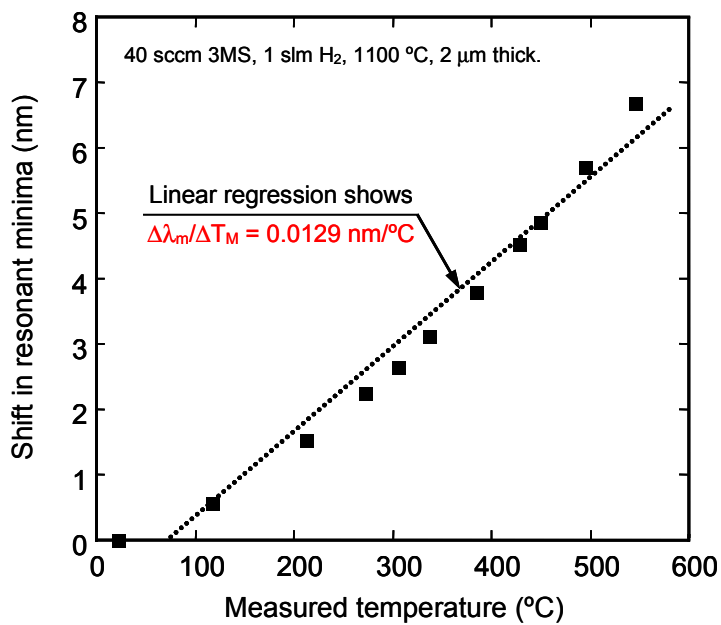


Figure 6-17. Measured shifts in resonance minima, $\Delta\lambda_m$, versus measured temperature, T_M , for the SiC temperature sensor fitted to a linear function.

The temperature accuracy of the poly-SiC temperature sensor was obtained by comparing spectrometer-sensed temperature to the actual temperature measured by a thermometer. For more accurate information on the temperature, the normalized resonance shift was defined as:

$$\overline{\Delta\lambda_m}(T) = \frac{\lambda_m(T) - \lambda_m(T_0)}{\lambda_m(T_0)} \cdot 100\% \quad (14)$$

where $T_0 = 22.2^\circ\text{C}$ by arbitrary definition. Fig. 6-18 shows that a quadratic function accurately fits the experimental data of $\overline{\Delta\lambda_m}(T)$ function. From Fig. 6-19, The deviation of normalized resonance shifts, $\delta[\overline{\Delta\lambda_m}(T)]$, from the quadratic fit exhibits a temperature accuracy of $\pm 3.5^\circ\text{C}$ over the range of 22°C to 540°C . We expect that this accuracy can be further improved by using a higher resolution spectrometer.

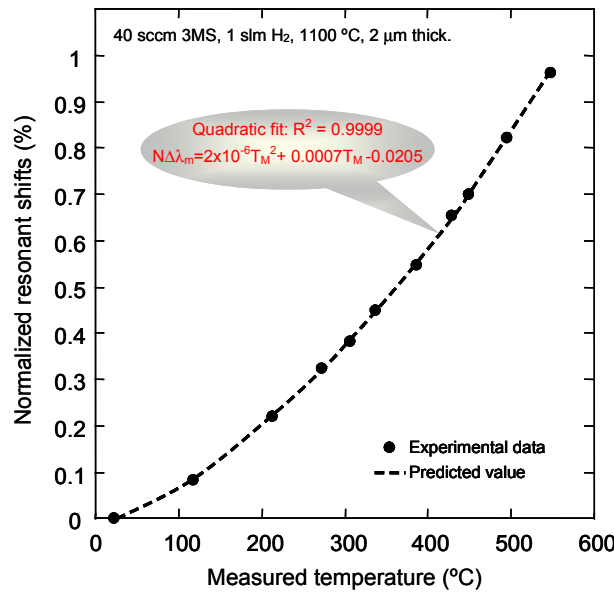


Figure 6-18 Normalized resonant shifts, $\overline{\Delta\lambda_m}(T) = \frac{\lambda_m(T) - \lambda_m(T_0)}{\lambda_m(T_0)} \cdot 100\%$,

versus measured temperature, T_M , for the SiC temperature sensor fitted to a quadratic function.

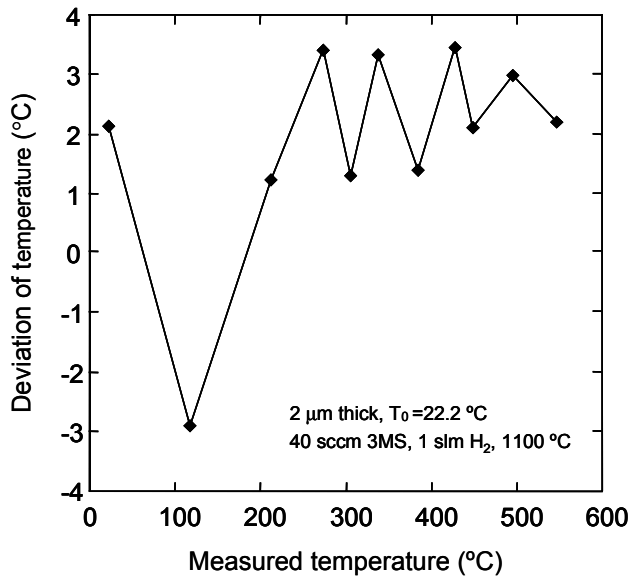


Figure 6-19 The deviation of normalized resonant shifts, $\delta[\overline{\Delta\lambda}_m(T)]$, from the quadratic fit in Fig. 6-18, expressed in terms of the deviation of sensed temperature, ΔT_M , from measured temperature T_M .

6.5.3 Effect of SiC thin-film structure using different 3MS flow rate

We have discussed the effect of 3MS flow rate on the structural properties of poly-SiC thin-films in previous section 6.4.2. The effect of SiC thin-film structure using different 3MS flow rate on temperature sensing performance of the SiC sensors has been investigated using the same experimental setup for the temperature measurement described before.

Fig. 6-20 shows the output spectra of starting sapphire [0001] substrate and the SiC films grown with different 3MS flow rate. The spectra range from 490 nm to 1050

nm. All measured SiC samples but the starting sapphire substrate showed the interference pattern in the output spectra. The effects of 3MS flow rate and film thickness on the reflected intensity, curvature at the resonant minima, and the bandwidth between two adjacent resonant minima have been also observed. Because of the increasing sharpness of curvature at resonant minimum, the temperature sensitivity and accuracy of Fabry-Perot interferometric sensor can be improved by the increase of reflected intensity and/or the decrease of bandwidth between two adjacent resonant minima. Fig. 6-20 also shows that the film grown with 40 sccm 3MS has the highest reflected intensity while the film grown with 35 sccm 3MS has

the smallest bandwidth between two adjacent resonant minima, although these two films are thinner than other two films grown with 30 and 45 sccm 3MS. This indicates that the temperature sensing performance of the SiC sensor is determined by the structural properties of the SiC films, as we predicted in the previous discussion.

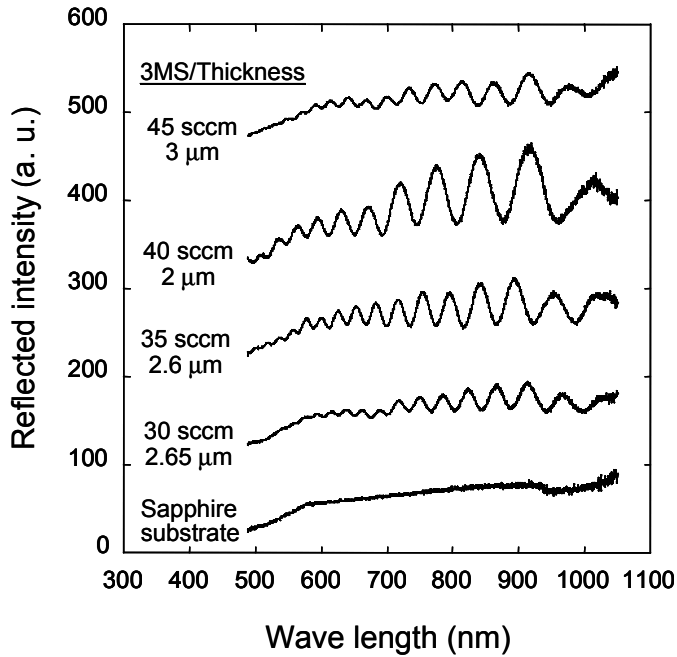


Figure 6-20 Sensor spectra: output spectra of SiC temperature sensors using SiC thin films grown on sapphire substrate with different 3MS flow rate. $490 \text{ nm} < \lambda < 1050 \text{ nm}$.

During the temperature sensing measurement, the one-way shifts in resonant minima $\Delta\lambda_m$ have been observed on all samples, which increase with the increased operating temperature T_M . The resonant wavelengths, λ_m , of the output spectra were presumed to correspond to the local minima in the reflection $R_s(\lambda)$ function. To determine λ_m , the $R_s(\lambda)$ was measured using a sampling interval of 0.3 nm. A quadratic fit was applied to $R_s(\lambda)$ in the ± 6 nm region about the minimum value, which was searched through the range of λ_m . By calculating the position of the polynomial's minimum, λ_m can then be determined. For the comparison of temperature sensing behavior of the SiC films grown under different conditions, we only investigated the shifts in resonant minima near the range of $660 \sim 700$ nm since it is difficult to find the same resonant minima from the output spectra on all samples. The linear fits to $\Delta\lambda_m$ versus measured temperature T_M over the range of 22 to 540 °C were then obtained to provide the corresponding thermal expansion coefficient, κ_ϕ , for each SiC sensor. The calculation of $\Delta\lambda_m$ over ΔT_M provides the relative temperature sensitivity of $1.77 \sim 1.89 \times 10^{-5}/^\circ\text{C}$ at $\lambda_m(T_0=22\text{ }^\circ\text{C})$ of 675.818 nm, 667.585 nm, 692.827 nm, and $0.55 \times 10^{-5}/^\circ\text{C}$ at $\lambda_m(T_0)$ of 714.232 nm for the SiC films grown with 30, 35, 40, 45 sccm 3MS, respectively. Obviously, the film grown with 45 sccm 3MS will not provide an expected temperature sensing performance.

For more accurate information on the performance of SiC temperature sensors, the normalized resonance shift was then defined in eq. (14) on page 136, where $T_0 = 22$ °C by arbitrary definition. Again for the samples grown with 35 and 40 sccm 3MS, Fig. 6-21 shows that the quadratic functions more accurately fit the experimental data of

$\overline{\Delta\lambda_m}(T_M)$ function than those grown with 30 and 45 sccm 3MS. For further information on temperature accuracy of the SiC temperature sensors, the deviation of sensed temperature ΔT_M is represented by the actually measured temperature T_M .

As shown in Fig. 6-22, the deviation of normalized resonance shifts, $\delta[\overline{\Delta\lambda_m}(T)]$, from their quadratic fits exhibits a temperature accuracy of ± 9.2 °C, ± 2.8 °C, and ± 3.5 °C over the range of 22 °C to 540 °C for the samples grown with 30, 35, and 40 sccm 3MS. These results enhance the previous statement in advance about the effects of growth conditions on the structural properties, hence the temperature sensing performance, of SiC Fabry-

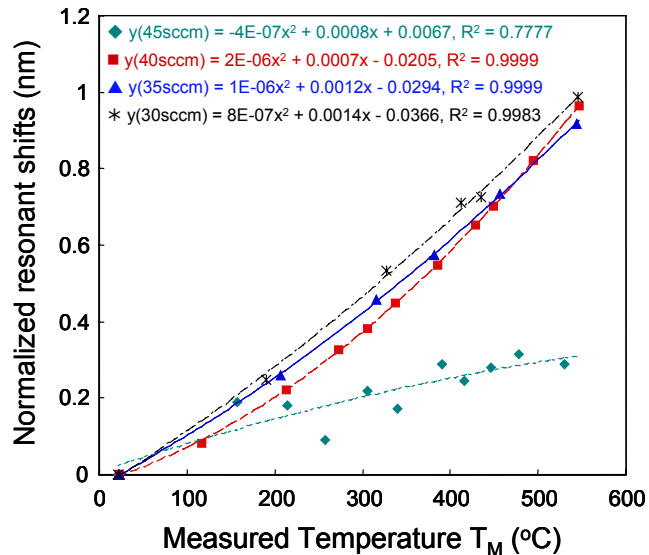


Figure 6-21 Normalized resonance shifts, $\overline{\Delta\lambda_m}(T)=100\%[\lambda_m(T)-\lambda_m(T_0)]/\lambda_m(T_0)$, versus measured temperature for the SiC temperature sensors fitted to the quadratic functions.

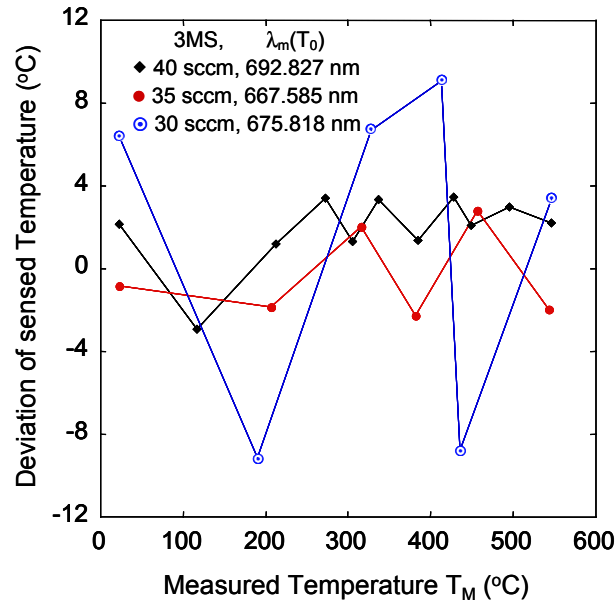


Figure 6-22 Effect of 3MS flow rate on the deviation of sensed temperature (i.e. temperature accuracy), ΔT_M , of the poly-SiC temperature sensors, expressed in term of measured temperature, T_M .

Perot interferometers. The best device performance is obtained from the sensor fabricated using optimized growth conditions and SiC film thickness.

6.5.4 Short-term stability test

During the temperature sensing measurement, the light coming out of the illumination fibers went through the sample from the backside of the sapphire substrate and was reflected at the end surface of SiC film and SiC-sapphire interface. The reflected light was then collected by the read fiber, while the output spectrum can be almost obtained synchronically. Within the spectral range of the grating, 500 nm to 1100 nm, in the spectrometer, the thin-film interference was observed when viewing the spectrum in reflection mode. Before recording the output spectrum, the lamp was allowed to warm up and stabilize for 30 minutes. The temperature was increased from 22 °C to 540 °C, continuously. At each temperature set point, it took about 30 minutes to increase and 2 hours to stabilize the temperature. Then the output spectrum was recorded, which contains the data information on temperature sensing performance of SiC Fabry-Perot interferometer. For the measurement of short-term stability, the soak temperature was brought to 532 °C and allowed to stabilize for 24 hours before the baseline $R_s(\lambda)$ measurement were performed.

The short-term stability test on the sensor using 35 sccm 3MS was performed at a constant temperature of 532 °C for about 14 days. The sensor was not pre-annealed and was characterized only at room temperature prior to this test. It was fully exposed to the

air during the measurements. The wavelengths at resonant minima were determined using the same method described before in this paper. The shifts in λ_m , relative to the baseline value, were converted to the changes in T_M using the measured value of κ_s . In Fig. 6-23, the sensor does not show any systematic temperature drifts. Instead, it shows a random variation within the range of $-2 \sim + 3.5$ °C about the baseline temperature. Over the full duration of this test, the temperature measurements of the sensor had a standard deviation of 0.97 °C. The results demonstrate the promise of SiC Fabry-Perot interferometric temperature sensor for high-temperature applications.

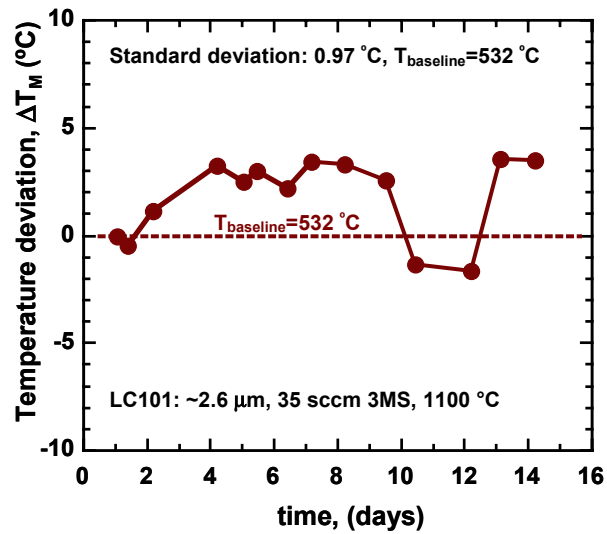


Figure 6-23 Short-term stability measurement on one SiC sensor exposed to 532 °C in air for two weeks shows the random variations of temperature about the baseline temperature and a standard deviation of 0.97 °C

6.6 Summary and Conclusion:

In summary, we have presented the fabrication and characterization of poly-SiC thin-films grown on insulating sapphire substrates for high temperature fiber-optic applications. The optically flat poly-SiC thin-films were successfully grown by LPCVD

on crystalline sapphire substrate at a much lower processing temperature (1100 °C) than that required for the epitaxial growth of single-crystal SiC. The optimized growth conditions for SiC thin films have been developed to provide the optically flat surface for SiC Fabry-Perot interferometers.

To investigate the temperature sensing behavior of the poly-SiC thin-film as a Fabry-Perot interferometer, a method of spectrum-modulating temperature measurement has been developed. The initial results on the temperature sensing behavior of this poly-SiC interferometer showed that the one-way phase shift in resonance minimum is a function of operating temperature over the range of 22.2 °C to 540 °C. The effects of thickness and structural properties of the poly-SiC thin-films on the performance of temperature sensors have been discussed. A temperature accuracy of ± 2.8 °C over the temperature range of 22 °C to 540 °C has been obtained from the sample with 2.6 μm thick SiC film grown with 35 sccm 3MS. The short-term stability test shows that the SiC Fabry-Perot interferometric temperature sensor is highly stable at temperature of 532 °C in a wide-opened ambient.

Our current research indicates that the SiC Fabry-Perot interferometer is very promising and economical for the applications of robust fiber-optic temperature sensor operating in harsh environment. However, a more precisely and reliably experimental setup is required for the measurement at higher temperature and in corrosive ambient. The potential of this poly-SiC temperature sensor operating at higher temperature range needs to be further studied.

6.7 References:

-
- [1] “Fiber Optical Sensor Technology and Applications 2001”, *Proc. SPIE – INT. Soc. Opt. Eng.*, p. 4578, 2002.
- [2] R. Lyons, “Fiber Optic Sensor Components and systems for Smart materials and Structures”, *NASA Report*, 1999.
- [3] M. R., “Fly-By-Light/Power-By-Wire Fault-Tolerant Fiber-Optic Backplane”, *NASA Report* NAS 1.26:211632, 2002.
- [4] G. H. Ames, “Multiplexed fiber Laser System”, *Patent Appl. PAT-Appl-8-983 046*, 2001.
- [5] M. A. Fonseca, J. M. English, M. von Arx, and M. G. Allen, “Wireless micromachined ceramic pressure sensor for high-temperature application,” *IEEE J. Microelectromechanical Systems*, vol. 11, pp. 337-343, Aug. 2002.
- [6] A. Solangi, and M. I. Chaudhry, “Fabrication and electrical properties of β -SiC/Si and poly-SiC/Si solar cells,” in *Springer Proceedings in Physics*, vol. 71, and *Amorphous and Crystalline Silicon Carbide IV*, eds.: C. Y. Yang, M. M. Rahman, and G. L. Harris, Springer-Verlag Berlin Heidelberg, pp. 362-367, 1992.
- [7] L. Cheng, M. Pan, J. Scofield, and A. J. Steckl, “Growth and doping of SiC thin films on low-stress, amorphous Si_3N_4 /Si substrates for robust microelectromechanical systems applications,” *J. Electronic Materials*, vol. 31, pp. 361-365, May 2002.
- [8] S. Roy, R. G. DeAnna, C. A. Zorman, and M. Mehregany, “Fabrication and characterization of polycrystalline SiC resonators,” *IEEE Trans. Electron. Dev.*, vol. 49, pp. 2323-2332, Dec. 2002.
- [9] L. Cheng, A. J. Steckl, and J. D. Scofield, “SiC Thin-Film Fabry-Perot Interferometer

for Fiber-Optic Temperature Sensor”, *submitted to IEEE Trans. on Electron Devices*,

2003

[¹⁰] H. F. Taylor, “Fiber optic sensors based upon the Fabry-Perot interferometer,” in *Fiber Optic Sensors*, eds.: F. T. S. Yu, and S. Yin, Marcel Dekker, Inc., pp. 41-71, 2002.

[¹¹] M. Ohring, ed., “The Materials Science of Thin Films,” Academic Press, Inc., pp.526-530, 1992.

[¹²] G. Beheim, K. Fritsch, and D. J. Anthan, “Fiber-optic temperature sensor using a spectrum-modulating semiconductor etalon,” NASA Technical Memorandum 100153, 1987.

[¹³] G. Beheim, “ Fiber-optic temperature sensor using a thin-film fabry-perot interferometer,” in *Ph. D. thesis*, Case Western Reserve University, Cleveland, Ohio, pp. 73-83, May 1996.

[¹⁴] Y. J. Rao, and D. A. Jackson, “Principles of fiber-optic interferometry,” in *Optical Fiber Sensor Technology*, eds.: K. T. V. Grattan, and B. T. Meggitt, pp. 167-191, 2000.

[¹⁵] A. Yariv, ed., “Optical Electronics in Modern Communications,” Fifth edition, *The Oxford Series in Electrical and Computer Engineering*, Sr. Consulting ed.: M. E. Van Valkenburg, Series eds.: Adel S. Sedra, and Michael R. Lightner, Oxford University Press, pp. 125-131, 1997.

[¹⁶] D. A. Krohn, ed., “ Fiber Optic Sensors — Fundamentals and Applications,” INSTRUMENT SOCIETY OF AMERICA, pp. 45-61, 1988.

[¹⁷] J. Chen, A. J. Steckl, and M. J. Loboda, “In-situ N₂-doping of SiC films grown on Si (111) by chemical vapor deposition from organosilanes,” *J. Electrochem. Soc.*, vol. 147, pp. 2324-2327, 2000.

[¹⁸] C. Lavoie, T. Pinnington, E. Nodwellm, T. Tiedje, R. S. Goldman, K. L. Kavanagh, and J. L. Hutter, “Relationship between surface morphology and strain relaxation during growth of InGaAs strained layers,” *Appl. Phys. Lett.*, vol. 67, No. 25, pp. 3744-3746, September, 2002.

[¹⁹] M. Ohring, ed., “The Materials Science of Thin Films”, Academic Press, Inc., p. 203, 1992.

CHAPTER 7. SUMMARY AND CONCLUSION

The work presented here studies the growth, mechanical polishing, ICP etching, and structural, electrical and optical properties of the SiC thin-films grown on the insulating, low-stress, amorphous $\text{Si}_3\text{N}_4/\text{Si}$ or single-crystal sapphire substrates with the single organosilane trimethylsilane by a rapid thermal LPCVD. The experimental results show that the SiCOI structures are very promising for robust MEMS and high temperature fiber-optic applications.

The fabrication and properties of SiC structures for high temperature MEMS applications have been reported. The MEMS device requires the growth and doping of SiC thin films on amorphous Si_3N_4 layers on Si substrates. The in-situ doping was performed by addition of N_2 into the reaction chamber. The sheet resistance and resistivity can be readily controlled by the growth temperature and N_2 gas flow rate. A resistivity of $75\Omega/\square$ was measured for the N_2 doped SiC film when operating the structure at 400K. MEMS structures such as cantilevers, lateral resonators and membranes were successfully fabricated.

Initial fabrication of MEMS structures by inductively coupled plasma (ICP) dry etching has shown that LPCVD conformal growth of SiC on low-stress amorphous Si_3N_4 layer is successful. To improve surface morphology of the as-grown SiC films, a mechanical polishing method has been developed for a good mask adhesion and high etching yield. Under the low RF/ICP power conditions (40~100/100~400 W), NF_3/Ar

gaseous mixtures were utilized to produce smooth etched SiC surface. Vertical side-walls indicating high anisotropy of NF₃/Ar etching have been obtained under certain conditions. The dependence of etch rate on etching conditions (such as gases ratio, ICP power, RF chuck power and DC bias) has been studied. Positive photoresist Shipley1818 has been evaluated as a mask material for SiC etching in both NF₃/Ar and Cl₂/Ar discharges. Cl₂/Ar shows promise for ICP etching of the SiC film under certain condition. Further efforts on optimizing etching conditions are required for high etch rate with low damage.

Optically flat poly-SiC thin-films were successfully grown on crystalline sapphire substrate at a much lower processing temperature (1100 °C) by LPCVD than that required for the epitaxial growth of single-crystal SiC. The optimized growth conditions for the SiC thin-films have been developed to provide the optically flat surface for SiC Fabry-Perot interferometers. To investigate the temperature sensing behavior of the poly-SiC thin-film as a Fabry-Perot interferometer, a method of spectrum-modulating temperature measurement has been developed. The initial results on the temperature sensing behavior of this poly-SiC interferometer showed that the one-way phase shift in resonance minimum is a function of operating temperature over the range of 22.2 °C to 540 °C. The effects of thickness and structural properties of the poly-SiC thin-films on the performance of temperature sensors have been discussed. A temperature accuracy of ±2.8 °C over the temperature range of 22 °C to 540 °C has been obtained from the sample with 2.6 μm thick SiC film grown with 35 sccm 3MS. The short-term stability

test shows that the SiC Fabry-Perot interferometric temperature sensor is highly stable at temperature of 532 °C in a wide open ambient for two weeks.

Our current research indicates that the SiC Fabry-Perot interferometer is very promising and economical for the applications of robust fiber-optic temperature sensor operating in harsh environment. However, a more precisely and reliably experimental setup is required for the measurement at higher temperature and in corrosive ambient. The potential of this poly-SiC temperature sensor operating at higher temperature range needs to be further studied.